UNIVERSITY OF CALIFORNIA, SAN DIEGO

In pursuit of small molecule based prevention of Alzheimer's disease: defining the mechanistic pathway via bilayer electrophysiology

A dissertation submitted in partial satisfaction of the
requirements for the degree
Doctor of Philosophy

in

Bioengineering

by

Alan L. Gillman

Committee in charge:

Professor Ratneshwar Lal, Chair
Professor Gert Cauwenberghs
Professor Bruce Kagan
Professor Edward Koo
Professor Eliezer Masliah

2015

The dissertation of Alan L. Gillman is approved, and it is acceptable in quality and form for publication on microfilm and electronically:

_____

_____

_____

_____

_____
Chair

University of California, San Diego

2015

DEDICATION

To my parents, for their unconditional love and support.

EPIGRAPH

Alice: This is impossible.
The Mad Hatter: Only if you believe it is.
– Lewis Carroll, *Alice in Wonderland*

TABLE OF CONTENTS

LIST OF FIGURES

LIST OF TABLES

ACKNOWLEDGEMENTS

The work presented in this dissertation was not performed in a vacuum and would not have been possible without the help of many people. I would first like to thank my advisor and committee chair Ratnesh Lal for the supervision and support that he showed throughout my graduate studies. His leadership was crucial in guiding me down the research path that ultimately led to work presented within. I would like to thank Dr. Ricardo Capone and Dr. Rustam Azimov for their time and patience while training me in the bilayer recording technique. I am sincerely grateful to committee members Dr. Bruce Kagan, for his many discussions with me regarding data interpretation, and Dr. Eliezer Masliah, for his assistance with small molecule drug interventions. I would like to thank the members of my committee, Dr. Gert Cauwenberghs and Dr. Edward Koo, for their feedback and guidance.

I have been lucky enough to be part of great collaborative work throughout my doctoral studies and have worked with truly great individuals. I want to thank my collaborators at the NIH, Dr. Hyunbum Jang and Dr. Ruth Nussinov, for the modeling presented in Chapter 2. Thank you to Joe Phaneuf for working on your own time to code the custom Python analysis program presented in Chapter 3. The work in Chapters 4 & 5 would not have been possible without two separate small molecule compounds generously provided to our laboratory. I would like to thank Dr. Christian Griesinger of the Max Planck Institute for Biophysical Chemistry (Göttingen, Germany) for the Anle138b compound presented in Chapter 4 and Neuropore Therapies Inc. (San Diego, California) for the NPT-440-1 compound presented in Chapter 5.

Grad school was a long process and one that would have felt much longer and been much less fun without truly wonderful people surrounding me on a daily basis. I cannot thank the members of the Lal Lab enough for their contributions, not only from a scientific standpoint but also in making life more enjoyable. I would especially like to thank Brian Meckes, Jeanie Kwok, Joon Lee, and Laura Connelly for your regular trips down to my basement "dungeon" and for your friendship.

Most importantly, I would like to thank my family. Words alone cannot adequately express my gratitude for all of the support that you have given over the years. Jason and Michael, thank you for paving the way and giving me standards to strive for.

Mom and Dad, thank you for your unwavering confidence in my abilities over the years and for listening to me vent even when you had no idea what it was that I was talking about. I could not have asked for a better family and Michael has said it best: we truly won the genetic lottery.

Chapter 2, in full is a reprint of the material as it appears in the Journal of Physical Chemistry B, 2014, Gillman, A.L., Jang, H., Lee, J., Ramachandran, S., Kagan, B.L., Nussinov, R., and Arce, FT. The dissertation author is shared primary author of this paper with Dr. Hyunbum Jang.

Chapter 4, in part, is currently being prepared for submission for publication of the material. Hernandez Martinez, A., Gillman, A.L., Lee, J., Ryazanov, S., Agbemenyah, H.Y., Li, Q., Leonov, A., Benz, R., Giese, A., Arce, FT., Korte, M., Lal, R., Griesinger, C., Eichele, G., and Fischer, A. The dissertation author is a shared primary investigator of the material with Ana Hernandez Martinez and Joon Lee.

Chapter 5, in part, is currently being prepared for submission for publication of the material. Gillman, A.L., Lee, J., Ramachandran, S., Capone, R., Masliah, E., and Lal, R. The dissertation author is the primary investigator and author of this material.

VITA

2009	B. S. in Agricultural & Biological Engineering, *Summa cum laude*, University of Florida
2012	M. S. in Bioengineering, University of California, San Diego
2013	C. Phil. in Bioengineering, University of California, San Diego
2015	Ph. D. in Bioengineering, University of California, San Diego

PUBLICATIONS

Gillman, A.L., Lee, J., Ramachandran, S., Capone, R., Masliah, E., and Lal, R. Reduction in β-sheet character prevents neurotoxic ionic flux through $A\beta_{1-42}$ pores. 2015 *In Preparation*

Hernandez Martinez, A.*, **Gillman, A.L.*,** Lee, J.*, Ryazanov, S., Agbemenyah, H.Y., Li, Q., Leonov, A., Benz, R., Giese, A., Arce, FT., Korte, M., Lal, R., Griesinger, C., Eichele, G., and Fischer, A. The oligomer modulating anle138b compound blocks $A\beta$ channels and rescues the phenotype in the APP PS1 Δ9 mouse Alzheimer's model. 2015 *In Preparation*

Jang, H., Arce, F.T., Lee, J., **Gillman, A.L.,** Ramachandran, S., Kagan, B.L., Lal, R., and Nussinov, R. Computational Methods for Structural and Functional Studies of Alzheimer's Amyloid Ion Channels. *Methods in Molecular Biology* DOI $10.1007/978-1-4939-2978-8\_16$

Lee, J., **Gillman, A.L.,** Jang, H., Ramachandran, S., Kagan, B.L., Nussinov, R., and Arce, F.T. Role of the Fast Kinetics of Pyroglutamate-Modified Amyloid-β Oligomers in Membrane Binding and Membrane Permeability. *Biochemistry* 2014 *53* (28), 4704-4714

Gillman, A.L.*, Jang, H.*, Lee, J., Ramachandran, S., Kagan, B.L., Nussinov, R., and Arce, FT. Activity and Architecture of Pyroglutamate-Modified Amyloid-β ($A\beta_{pE3-42}$) Pores. *J Phys Chem B* 2014 *118* (26), 7335-7344

Connelly, L.S.*, Meckes, B.*, Larkin, J., **Gillman, A.L.,** Wanunu, M., and Lal, R. Graphene Nanopore Support System for Simultaneous High-Resolution AFM Imaging and Conductance Measurements. *ACS Applied Materials & Interfaces* 2014 *6* (7), 5290-5296

Landon, P.B., Ramachandran, S., **Gillman, A.L.,** Gidron, T., Yoon, D., and Lal, R. DNA Zipper-Based Tweezers. *Langmuir* 2012 *28* (1), 534-540

* Denotes equal authorship

ABSTRACT OF THE DISSERTATION

In pursuit of small molecule based prevention of Alzheimer's disease: defining the mechanistic pathway via bilayer electrophysiology

by

Alan L. Gillman

Doctor of Philosophy in Bioengineering

University of California, San Diego, 2015

Professor Ratneshwar Lal, Chair

The prevailing hypothesis for pathology of Alzheimer's disease (AD) proposes that amyloid-beta ($A\beta$) peptides are the toxic element. Small oligomers of $A\beta$ are believed to induce uncontrolled, neurotoxic ion flux across cellular membranes. The resulting inability of neurons to regulate their intracellular concentration of ions, particularly calcium ions, has been associated with cell death and may contribute to the cognitive impairment typically seen in AD patients. The mechanism of the ion flux is not fully understood, but the most direct mechanism of membrane disruption would be the formation of channel-like pores. Structural models and experimental evidence suggest that $A\beta$ pores form from an assembly of loosely-associated mobile β-sheet subunits. However, further understanding of the underlying mechanism of AD will be crucial to

our ability to design highly efficacious therapeutics. The dissertation focuses on the application of bilayer electrophysiological recordings to the study and determination of the mechanistic pathway of $A\beta$ pathophysiology in AD. Biophysical characterization of the highly cytotoxic pyroglutamate-modified $A\beta$ ($A\beta_{pE}$) is first presented. We show that $A\beta_{pE}$ activity is shifted to higher conductance events, which could explain their increased toxicity. Next, we introduce, and provide proof of concept for, a newly developed analysis tool which more accurately depicts cytotoxicity than traditional channel analysis methods. Finally, we use two small molecule drug candidates to test efficacy and gain insight into the mechanism of pore formation. From the results we suggest structural targets for future therapeutic design. This work advances the understanding of the underlying mechanism of AD pathophysiology by pore formation and will aid the design of small molecule pharmaceuticals for the treatment/prevention of this devastating disease.

Chapter 1

Introduction

1.1 Alzheimer's Disease

1.1.1 History and Prevalence

In 1906 Alois Alzheimer gave a talk at the Meeting of Psychiatrists of South West Germany. There he presented the case of one of his patients, *Auguste D*, who had died earlier in the year at the age of 55 following a dementing illness. Alzheimer described the unusual pathological features in her brain including plaques and tangles and published his first paper on the topic the following year [1]. While Alzheimer was the first to describe the tangles in detail [2], he was not the first to observe the clinical symptoms of the disease, nor was he the first to describe the plaques [3] that would become the pathological hallmark of the disease that bears his name [4]. However, Alzheimer recognized that this case did not fit well within the confines of any other defined disorder of the day and that it was a unique disease [4, 5]. It was not until the late 1960s that it was recognized that the majority of "senile dementia" cases showed Alzheimer pathology [6, 7, 8], and with that a new era of disease recognition began.

Alzheimer's disease (AD) is a progressive neurodegenerative disease that is the most common cause of dementia [9, 10]. Clinically, AD is characterized by the loss of memory, thinking, and brain functions. It has become increasingly clear over the years that AD is one of the largest health related problems facing society, with its impact continuing to grow both from a human and economic perspective. Age is the single

greatest risk factor in developing AD with less than 4% of cases in individuals under the age of 65 (Figure 1.1) [11] and a risk that doubles every 5 years over the age of 65 [12]. Improvements in modern healthcare have led to a steady increase in human life expectancy. Unfortunately, as more people live to reach older age the numbers of individuals projected to develop neurodegenerative diseases, such as AD, are set to increase dramatically [13, 14, 15]. According to the latest figures, 5.3 million Americans currently suffer from AD with that number expected to leap as newly proposed diagnostic criteria goes into place in conjunction with the aging of the populace [11]. AD is considered the 6^{th} leading cause of death in the United States and, despite years of research on the topic, is the only one of the top ten that currently has no effective way to slow, cure, or prevent progression. There are currently six FDA approved drugs on the market, with only one being approved in the past decade [11]. These drugs show minimal efficacy and temporarily improve some of the symptoms while not addressing the underlying pathophysiology. Sadly, in many ways *Auguste D's* prognosis would be the same today as it was during the early 20^{th} century.

1.1.2 The Amyloid Hypothesis

The mechanism of disease pathogenesis has been the source of speculation and research for the past several decades, but remains unclear to this day. The majority of the research has focused on the pathological hallmarks of AD, namely the presence of intracellular neurofibrillary tangles (NFTs) and extracellular plaques [1, 4, 15, 16, 17, 18, 19, 20]. These aggregates are primarily comprised of a class of abnormally folded proteins known as amyloids in their fibril form [21, 22]. Over the last quarter century, no fewer than 16 different clinical syndromes have been characterized by the presence of amyloid deposits [22, 23], each with a different primary amyloid protein. Rudolf Virchow mistakenly believed amyloids to be carbohydrate in nature, first using the term in 1854 to describe amorphous "starch-like" deposits that stained purple with iodine [22, 24, 25, 26, 27]. Subsequent studies revealed that these deposits were composed of proteins. Today amyloids are classified as misfolded proteins that aggregate into (fibrilar) deposits, exhibit cross β-sheet structure, are resistant to proteolytic cleavage, and bind Congo Red [28, 29, 30]. The fibrilar amyloids are a common pathological hall-

mark among amyloid diseases, known as amyloidosis [22, 28, 31, 32]. In addition to AD, many well-known diseases fall into the category of amyloidosis including Huntington's disease, Parkinson's disease, amyotrophic lateral sclerosis (ALS or Lou Gehrig's disease), and Type II diabetes [33, 28].

AD is unique in that it is characterized by two different fibrilar amyloid deposits: NFTs and senile plaques. While NFTs and their constituent protein, tau, have been the subject of intense research–including a recent study out of the Mayo Clinic that implicates tau as the primary driver of AD [34]–the majority of work has focused on the senile plaques. These plaques are composed primarily, but not exclusively, of aggregates of amyloid-beta ($A\beta$) in the fibril form. $A\beta$ is derived from the amyloid precursor protein (APP). APP is processed by the enzymes β- and γ- secretase [29, 35, 36, 37] (Figure 1.2) to produce the $A\beta$ peptide. Differential cleavage of APP by these secretases produces $A\beta$ of varying lengths, with $A\beta_{1-40}$ and $A\beta_{1-42}$ (consisting of 40 and 42 residues, respectively) being the predominant species generated [15, 35, 36, 38, 39, 40, 16]. Often these peptides are further procesed and modified to additional forms of $A\beta$, which may play a role in AD pathophysiology. One such form (Characterized in Chapter 2) is pyroglutamate (pE)-modified $A\beta$, which has been shown to represent the dominant fraction of $A\beta$ oligomers in brains of AD patients [41, 42].

Although $A\beta$ is found in large fibrils in the brain, the mechanism by which the peptide causes neurotoxicity is not fully understood. The prevailing view, known as the amyloid cascade hypothesis, states that $A\beta$ is the toxic element in AD pathophysiology [13, 14, 15, 16, 22, 24, 25, 43, 44, 45, 46, 47, 48, 49, 50, 51, 52, 53, 23, 54, 20, 55, 17, 56, 57, 58, 59, 60, 61, 62, 63, 64, 65, 18]. Over the years the cascade hypothesis has been modified to fit the results of various studies. A primary tenant of the hypothesis links $A\beta$ to pathophysiologic cell response via destabilization of cellular ionic homeostasis, primarily a gain of intracellular Ca^{2+}. Dysregulation of ionic homeostasis alters neuronal information processing (a loss of synaptic efficacy), leads to neuronal dysfunction, and eventual degeneration (cell death) via triggering of apoptotic pathways [66, 67, 68] (Figure 1.3). The prevailing view for many years pointed to the fibrilar aggregates of $A\beta$ as the toxic element [69, 70]. This view is no longer tenable. Instead, research in recent years has focused on small oligomers that appear to be the most toxic to cells

[48, 53, 71, 72, 73, 74, 75, 76, 77, 78]. These small oligomers lead to a destabilizing influx of Ca^{2+} primarily by the alteration of cellular membrane properties–including membrane thinning, non-specific leakiness, or pores to ionic transport across the cellular membranes (both plasma as well as intracellular membranes) [79]. The most direct mechanism of membrane disruption, which will be the focus of the dissertation, is via pore formation.

1.1.3 Channel Hypothesis

Just over two decades ago, Arispe et al first reported the remarkable finding that $A\beta$ was capable of forming ion-permeable channels in lipid bilayer membranes [57, 59]. Using a technique called planar lipid bilayer (PLB) recording (discussed below in depth) they showed that $A\beta$ induced unregulated ionic flux across model membranes through non-specifically cation selective channels. The channels were large, showed heterodisperse conductivity, Ca^{2+} permeable, and could be blocked by Zn^{2+}. Over a series of papers they hypothesized that membrane depolarization and/or Ca^{2+} influx could be responsible for cellular toxicity and proposed the amyloid channel hypothesis [57, 59, 80, 58, 61]. The heterogeneity of single channel conductances suggested that the channels are formed by multiple molecular species in the membrane. Furthermore, the activity is not fully dependent on the concentration of $A\beta$ species, implying that a subset of the possible structures is required to obtain channel activity. Due to unfavorable thermodynamics and a high energetic cost of a fully formed channel entering the membrane, it has been suggested that $A\beta$ oligomers can irreversibly insert into the membrane and spontaneously assemble within the bilayer to form a cytotoxic pore [81].

Since the development of the channel hypothesis, multiple complementary techniques have been used to test the theory. In 2001, Lin et al [48] presented high resolution AFM images that showed channel-like structures formed by $A\beta_{1-42}$ reconstituted in a model membrane system. They further validated that the channels demonstrated heterogeneous single channel conductance and blockage by Zn^{2+}, while demonstrating calcium uptake and neuritic degeneration in cell culture. Multiple AFM studies since that time have shown that $A\beta$ channels have outer diameter of $8-12$ nm and inner diameter $\sim$2 nm [48, 23, 82, 83, 84]. AFM images have accounted for the multilevel conductance

observed in PLB electrical recording by demonstrating that $A\beta$ pores are assemblies of several subunits. This structural motif is supported by molecular dynamics (MD) simulations of that suggest that oligomer subunits are mobile within the bilayer and are free to assemble into new pores, add to existing pores, or disassociate from other oligomers [85]. This leads to variable pore size and morphology and the heterogeneouss electrical activity of $A\beta$.

An increasing body of evidence has pointed to $A\beta$ pore formation. For technical reasons, much of the work on $A\beta$ pores has been conducted in model membrane systems leading many to question its applicability to in vivo toxicity. Demuro et al answered this challenge and, using a technique they have coined "optical patch-clamping", clearly demonstrated Ca^{2+} fluorescence transients after the addition of $A\beta_{1-42}$ to oocytes [86]. These transients were spatially localized which was highly suggestive of pore presence rather than nonspecific leakage. Most significantly the flux was heterogeneous in intensity, validating the multi-level nature of conductance events seen in electrical recordings. Capone et al further advanced the channel hypothesis by demonstrating that $A\beta$ with an all D- amino acid sequence retains strikingly similar features known for the all L- peptide. This result suggested that chirality had no bearing on $A\beta$ activity and is thus unlikely the result of stereospecific receptor binding [87, 82]. Recently Sciacca et al showed membrane disruption by $A\beta$ involves a two-step mechanism: i) the formation of ion permeable pores, ii) $A\beta$ fibrillization causes membrane fragmentation via a detergent-like mechanism [88]. This model suggests that distinct pore formation is followed by nonspecific leakiness of the membrane and is supported by data contained in this dissertation.

While evidence is mounting for the role of $A\beta$ pores playing a significant role in cytotoxicity, the mechanism of pore formation is unclear. Numerous MD simulations of $A\beta$ pores have pointed to a β-barrel structure for the intramembrane region of the pore [83, 84, 85, 89, 90, 91]. While some studies have pointed to the β-sheet secondary structure as a necessary element in $A\beta$ toxicity [90, 92, 93] the results of other studies have been mixed [92, 94, 95] and point to the need for further investigation.

1.2 Planar Lipid Bilayer Recording

1.2.1 History and Membrane Formation

The black lipid membrane (BLM) became the first artificial lipid membrane formed *in vitro* [96] in 1962 and has served as a model system of cellular membranes ever since. First demonstrated by Mueller and Rudin [96], BLMs have been used extensively to study the properties of the membrane itself as well as membrane embedded proteins, most notably ion channels. The term "black" refers to the fact that they appear dark under reflected light due to the destructive interference of light reflecting off of the two faces. This was the first indication that the bilayer formed was of molecular thickness (only a few nanometers), a phenomenon that was first noticed by Newton during his work with soap films. The technique relies on the formation of an artificial membrane over a small aperture (on the order of tens to a few hundred microns in diameter) in a non-conducting barrier between two electrically isolated chambers containing an aqueous ionic solution (buffer) (Figure 1.4A). There are two main types of BLMs that are characterized by their method of membrane formation: i) painted and ii) solvent-free or folded.

In the painted technique of Mueller and Rudin [96], lipid is dissolved in a hydrophobic solvent (typically heptane, decane, or squalene) and then painted over the aperture using a brush, syringe, or glass bulb. A spontaneous lipid monolayer forms at the interface between the organic and aqueous solutions on either side of the aperture. Once tethered to the hydrophobic walls of the partition, the solvent droplet thins at the center bringing the two monolayers together. When sufficiently close the monolayers fuse into a bilayer and rapidly exclude the solvent to the edges leaving a planar bilayer at the center of the aperture. The excluded solvent forms a significant annulus around the planar region of the membrane and is essential for membrane stability [97].

The solvent free method was introduced a decade later by Montal and Mueller to address the presence of non-excluded solvents between the lipid layers [98]. Volatile organic solvents, such as chloroform, are used to dissolve the lipids before depositing on the surface of each chamber. A lipid monolayer is formed at the air/water interface as the solvent evaporates away. The fluid level is then lowered and raised across the aperture,

folding the two monolayers together to form a bilayer. While folded membranes are devoid of intramembrane solvent and been shown to be slightly thinner than painted membranes [98], peptide activity is comparable between the two types [99, 100, 101, 102]. Due to the similarities in peptide activity between the two membrane types, the easier to prepare painted bilayers were used throughout the studies described within.

Since lipid membranes are non-conducting, insertion of ion channels into the membrane, either through spontaneous insertion or vesicle fusion, provides the only pathway for ionic currents to pass the membrane. By placing an electrode in both chambers and utilizing the voltage clamp mode of an amplifier, the activity of individual channels can be measured. In fact, BLM (used interchangeably with planar lipid bilayer, or PLB) recordings were used for the first single molecule studies in the early 1970s when Hladky and Haydon confirmed the unit channel structure of Gramicidin A (gA) [103] (Figure 1.4B). BLM and the patch-clamp technique, developed by Neher and Sakmann [104], have been used extensively in the study of ion channels due to their ability to recapitulate the electrical properties of cellular membranes.

1.2.2 The Electrical Model of the Cell Membrane

As an electronic model, the bilayer is represented as a resistor and a capacitor in parallel [105]. Simple measurements allow for the determination of whether a membrane was formed and to asses membrane size and quality. Lipids are poor conductors and thus are highly resistive. In electrophysiology studies the conductance (g) of the system is typically measured, and is given by rearrangement of Ohm's law:

$$g = R^{-1} = \frac{I}{V} \tag{1.1}$$

where R is membrane resistance, I is measured current, and V is the potential difference across the bilayer. Low bilayer conductances of < 10 pS ($R > 10$ GΩ) indicate the formation of a BLM over the aperture.

Furthermore, the bilayer has a capacitance due to the storage of charge near its surface. The bilayer can be thought of as two charged surfaces separated by a thin dielectric and can thus be approximated as a parallel plate capacitor by:

$$C = \frac{\varepsilon_0 \varepsilon_1 A}{d} \tag{1.2}$$

where C is the capacitance, A is the surface area of the bilayer, d is the bilayer thickness, ε_0 is the permittivity of free space, and ε_1 is the dielectric constant of the lipid. The capacitance is indicative of membrane area and thickness which are crucial for determination of membrane quality. Capacitance can be measured in real-time, allowing the investigator to monitor the evolution of the BLM over the course of the experiment. Manipulation of basic circuit equations allows us to relate the capacitance to easily measured parameters. Taking the time-dependent derivative of the relationship between charge (Q), voltage, and capacitance (Equation 1.3) gives an expression for capacitance that is linear with respect to the applied bias potential and the measured current (Equation 1.4) as follows:

$$Q = CV \tag{1.3}$$

$$I = \frac{dQ}{dt} = C\frac{dV}{dt}. \tag{1.4}$$

In practice, membrane capacitance is typically determined by the relationship between an applied symmetric triangular wave function (of known parameters) as the membrane potential and measuring the amplitude of the resulting rectangular current.

1.2.3 Advantages

The greatest advantage of BLM/PLB recording lies in its sensitivity. BLM recordings allow for the conductance of single channels to be resolved over large membrane areas. Membranes with estimated diameters of $120 - 180\ \mu m$ are typical under the working conditions used within our studies. This provides a very large surface area for channel formation to occur and greatly increases the probability of successful peptide incorporation. BLM provides single channel resolution while recording the bulk current through the membrane, making it a truly multiscale technique that allows for the simultaneous study of individual channel and ensemble properties.

Both BLM and path-clamping deliver single channel ionic conductance resolution in biologically relevant membranes. While patch-clamping is a remarkable tech-

nique that allows for the study of channels in live cells, it is ill suited for the study of amyloids. The cellular membrane in live cells is very complex, involving many variables, such as other membrane embedded ion channels, which are very difficult to isolate and control. Consequently, studying the ionic flux across a cellular membrane due to specific membrane proteins is extremely challenging. This is especially true for channels types that are not "well behaved" with clearly defined pore size and signature conductance (i.e. Na^+, K^+ channels). Amyloid channels, as further discussed below, exhibit variable pore sizes and multi-level conductance. As a result, we examine ionic flux across model bilayers using BLM.

By using a model membrane we ensure a pure system that isolates specific membrane permeabilizing peptides. BLM allows precise control over the constituents of the experimental setup, including the buffer, membrane composition, and peptide. Most BLM chambers are open in nature and provide easy access to both sides of the membrane allowing for online addition of components to the system. Many chambers also employ a perfusion or flow through design to quickly change out the buffer solution which enables to investigator to rapidly screen multiple compounds against channel activity [106].

In addition to experimental control, BLM provides great insight into the mechanism of peptide insertion and channel formation. Unlike patch-clamp, which necessitates the presence of channels in the membrane prior to isolation and gigaseal formation, BLM starts with a pure membrane. This pure membrane allows us to better understand the membrane binding and insertion mechanism of peptides. Some conducting pore forming peptides are able to spontaneously insert, either from one or both sides, into the bilayer while others require assistance through proteoliposome fusion. All studies in this dissertation were carried out by spontaneous pore formation with no assistance from proteoliposome fusion.

1.2.4 PLB Recording of Aβ Pores

While $A\beta$ is the focus of this dissertation, it must be noted that it is not the only amyloid capable of forming channel-like pores. Many, if not all, amyloid peptides have demonstrated ion permeable pores in vitro. Quist et al [23] presented a series of

AFM images of ion channels for a series of disease-related amyloid species, including $A\beta_{1-40}$, α-synuclein, ABri, ADan, SAA, and amylin (Figure 1.5). Despite the fact that amyloid proteins exhibit no amino acid sequence homology, they do share the physical chemical properties that lead to membrane poration [22]. As mentioned previously, $A\beta$ pores demonstrate heterogeneous single channel conductance, a characteristic that has been found in recordings of all characterized amyloids. This is unusual for typical ion channels that have been well studied in biological systems, which show characteristic single channel conductance (Figure 1.4B), and has led to pushback over the use of the term "ion channel." As a result amyloids are most accurately said to form channel-like pores of non-unitary conductance.

There are three different types of ionic activity that have been described for amyloid pores [22, 107], which are highlighted in Figure1.6. The first type of activity is known as the "bursting" fast cation channel which, as its name implies, is a short burst of activity that gives a nonlinear current-voltage relationship. The second type of channel activity is the "spikey" fast cation channel. Spike behavior is similar to the burst; however, the spike is more short-lived when compared to bursting activity. Lastly, the third type of channel activity is the "step" or "step-like" activity. With the step-like behavior a clear, defined jump in current is seen as a channel opens and closes. Step behavior is considered to most approximate the behavior seen in traditional ion channels (Figure 1.4B).

The variable nature of amyloid activity introduces challenges for their analysis. Many commercially available software packages exist for the analysis of electrophysiology data, but all rely on characteristic conductance levels for the creation of activity histograms. While qualitative conclusions can be drawn by observing the traces, without the unitary conductance, quantitative assessment is time consuming and labor intensive. The matter is complicated further by the different activity types which could erroneously bias histogram analysis toward prevalent but short lived pores that may not hold significance in cytotoxicity. For these reasons, current techniques make it difficult to make comparisons between the toxicity of different amyloid species.

1.3 Overview of the Dissertation

Decades of research have been dedicated to the understanding of AD and the search for a meaningful treatment. Despite this effort, little tangible progress has been seen in the treatment and prognosis of those who suffer from this devastating disease. While we have done a wonderful job of defining the parts that make up the puzzle, we still have not solved the fundamental question of how these pieces fit together to form the full picture of the disease. Determination of the underlying mechanism of AD will be crucial to our ability to design highly efficacious therapeutics. BLM recording, as a tool, has played an invaluable role in our understanding $A\beta$ induced cytotoxicity and will continue to do so going forward.

The dissertation focuses on the application of PLB/BLM recording to the study and determination of the mechanistic pathway of $A\beta$ pathophysiology in AD. The work within is focused on three main areas: i) biophysical characterization of a previously unstudied peptide; ii) development of new tools for the analysis and comparison of $A\beta$ pore toxicity; iii) use of small molecule drug candidates to test efficacy and gain insight into the mechanism of pore formation. Chapter 2 presents the first published biophysical characterization of $A\beta_{pE3-42}$—a highly toxic $A\beta$ variant found preferentially and in abundance in senile plaques—activity. Chapter 3 introduces our newly developed analysis software for amyloid recordings which more accurately depicts toxicity than traditional histogram analysis. As proof of concept for the software, data from Chapter 2 is reanalyzed. Chapters 4 & 5 present two different small molecule drug candidates, one embedded in the membrane (Chapter 4) and one in aqueous solution (Chapter 5). Insights into mechanism of channel formation and blockage are discussed along with potential areas of focus for future drug development.

Chapter 1 is original content. The dissertation author is the primary author of this content.

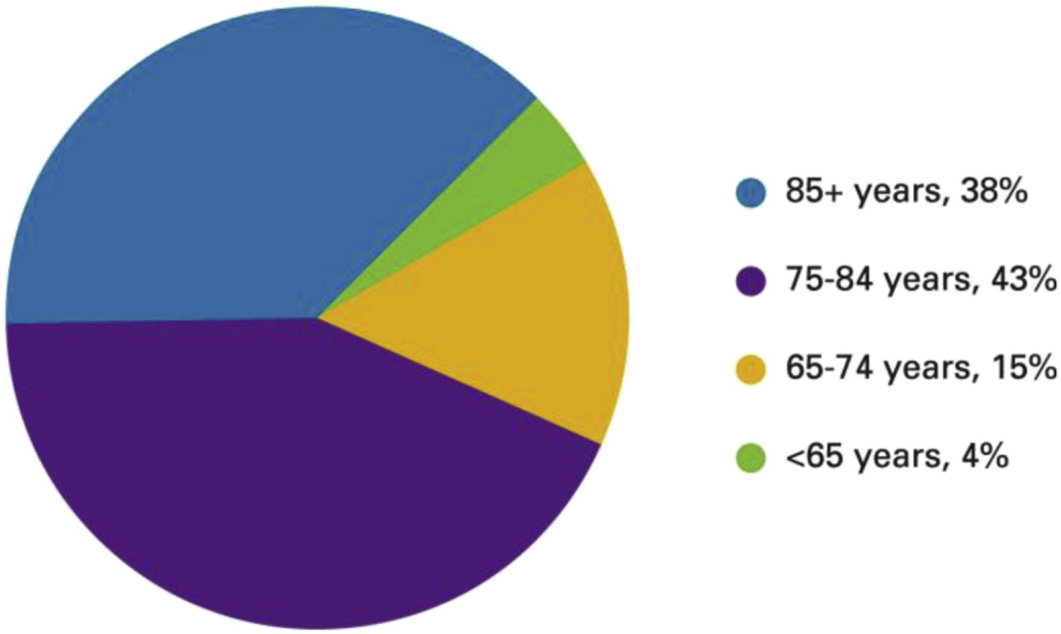

Figure 1.1: **Ages of people with AD in the United States, 2015.** Age is the single greatest risk factor for the development of AD. As the average life expectancy of the population increases, from improvements in medical care, the number of people afflicted with AD is expected to rise dramatically. From the 2015 Alzheimer's Facts and Figures report [11] with data by Hebert et al, 2013 [108]

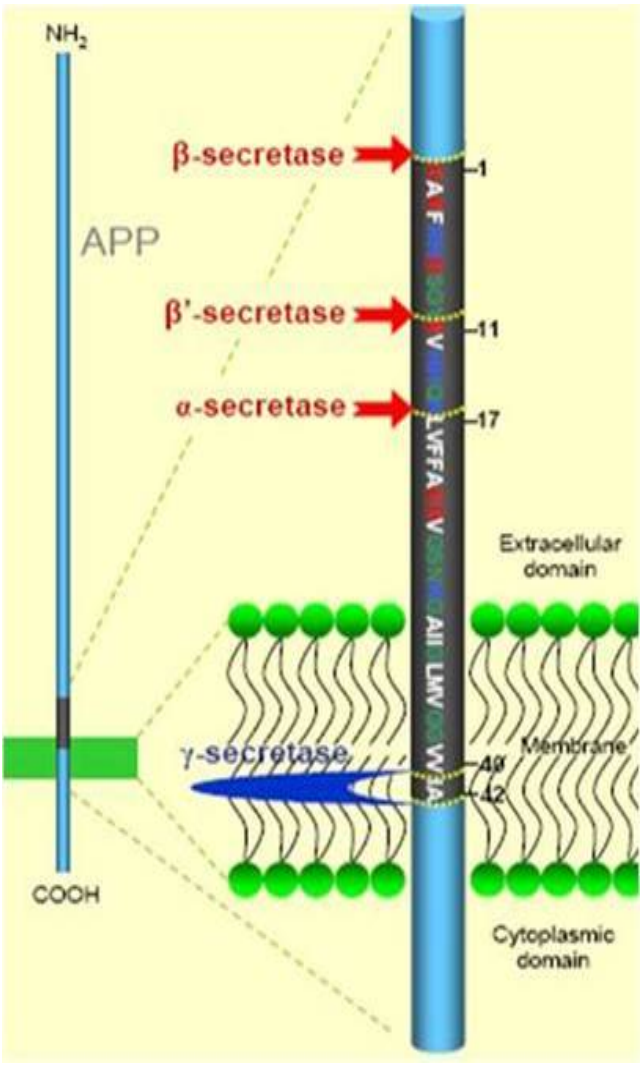

Figure 1.2: **Differential secretase processing of APP to form Aβ.** Differential cleavage of the amyloid precursor protein (APP) by α-, β-, and γ-secretase forms $A\beta$. Various $A\beta$ fragments are processed by different secretase combinations. Amyloidogenic fragments of $A\beta_{1-40}$/$A\beta_{1-42}$ are produced by β- and γ-secretase cleavage. From Thinakaran et al, 2008 [36] and Jang et al, 2010 [46], modified.

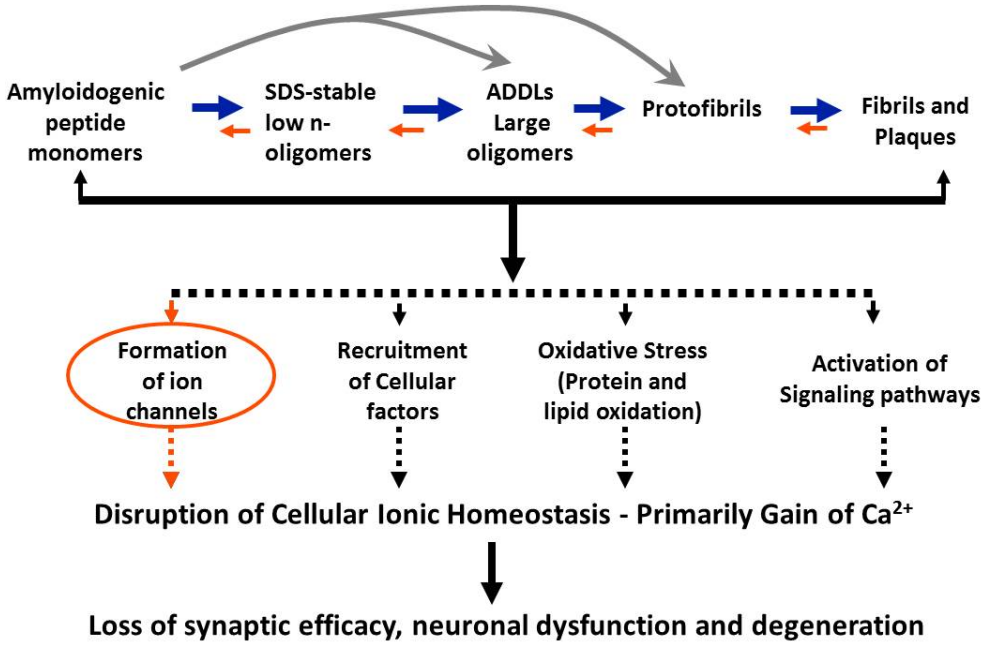

Figure 1.3: **Flow diagram of cascade hypothesis.** The amyloid cascade hypothesis links $A\beta$ to pathophysiologic cell response via destabilization of cellular ionic homeostasis, primarily a gain of intracellular Ca^{2+}. Dysregulation of ionic homeostasis alters neuronal information processing (a loss of synaptic efficacy), leads to neuronal dysfunction, and eventual degeneration (cell death). $A\beta$ exists in a variety of aggregated states from monomers to fibrils, with the small oligomers exhibiting the highest toxicity in cell culture models. Influx of Ca^{2+} may arise from a variety of factors including, but not limited to: the formation of ion channels, recruitment of cellular factors, oxidative stress, and activation of signaling pathways. The most direct mechanism of membrane destabilization, and the focus of this dissertation, is the formation of ion channels (highlighted in orange).

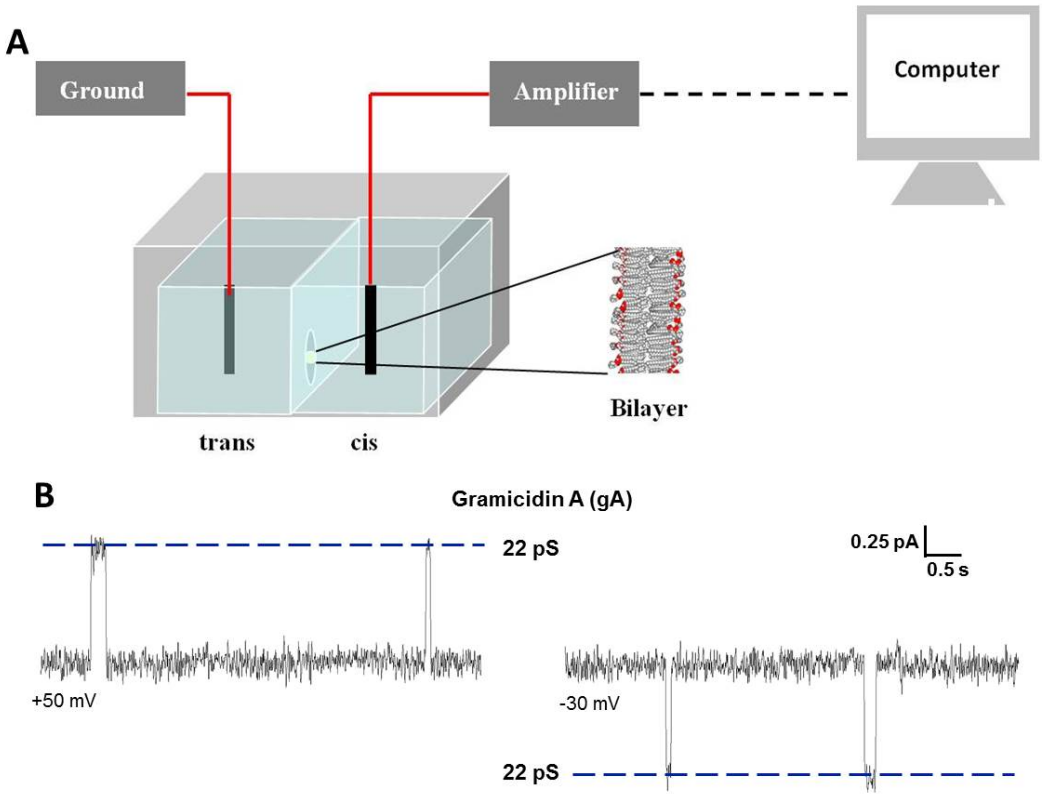

Figure 1.4: **BLM schematic and typical ion channel activity. A)** Schematic representation of our BLM/PLB setup for bilayer recordings. Two chambers are separated by a Delrin partition with a small aperture. Spontaneous membrane formation occurs when lipid solution is painted over the hole. We measure the current using electrodes submerged in the solution of each chamber: one is connected to the amplifier and the other is connected to ground as a reference electrode. The recordings are controlled and displayed using a LabVIEW program. From Kotler, 2011 (Master's Thesis) [109]. **B)** Gramicidin A (gA) forms channels of unitary conductance. This is typical behavior of many channels, but not of amyloid channel-like pores. We use gA for training on the technique as well as for validation of membrane formation at the end of membrane-only experiments.

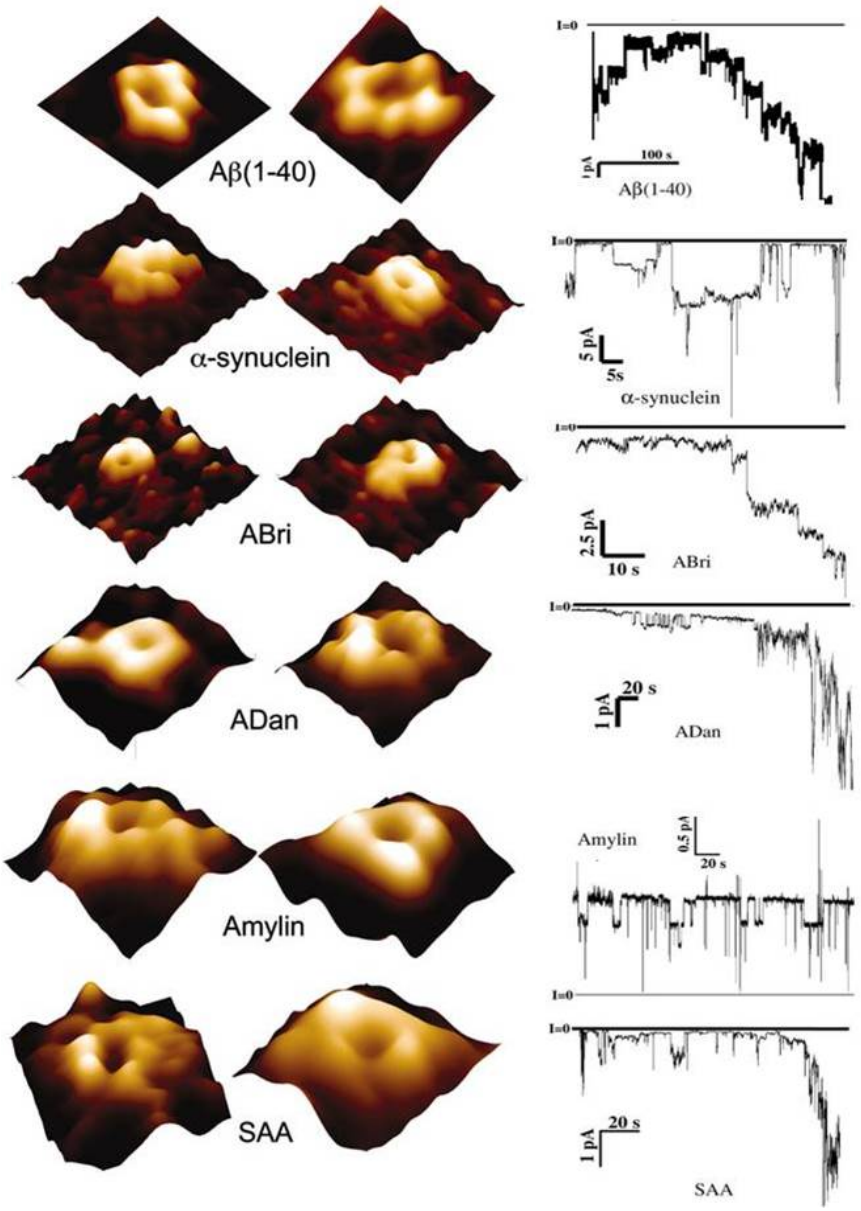

Figure 1.5: **Ion channel model of degenerative amyloid diseases.** AFM images show ion channel-like structures for (from top to bottom) amyloid beta 1-40, alpha-synuclein, ABri, ADan, amylin, and serum amyloid A.The electrical conductance activity of ion channels are shown to the right of each AFM image. Similar structures are reported from our lab for various other amyloids. Modified from Quist et al, 2005 [23].

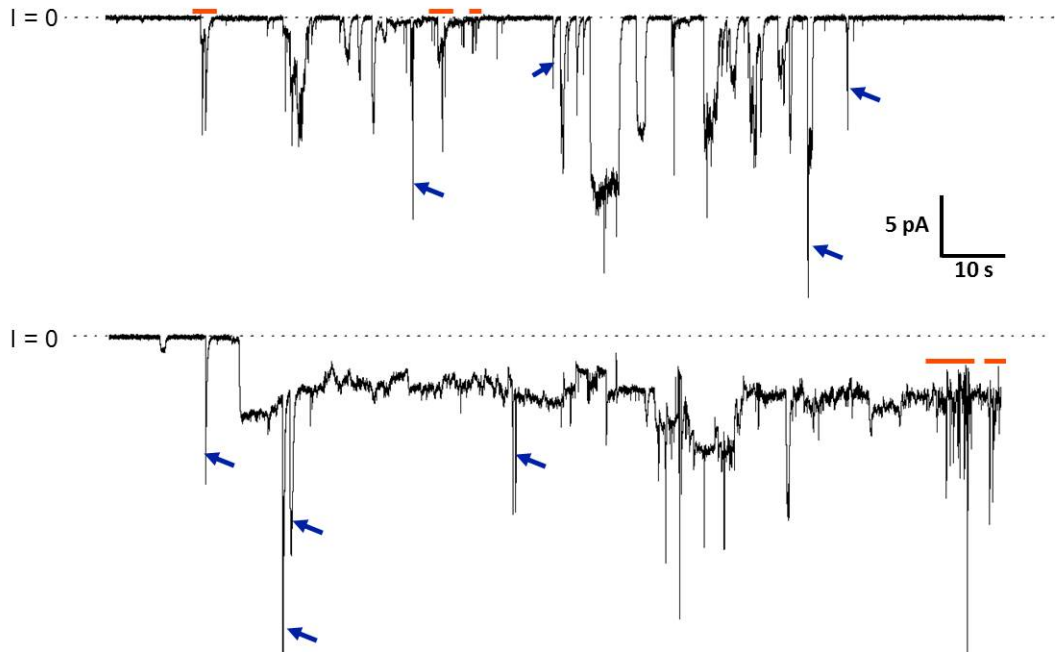

Figure 1.6: **Typical types of Aβ_{1-42} electrical activity.** Two separate recordings of $A\beta_{1-42}$ are shown demonstrating the typical activity types observed with $A\beta$ (and other amyloid) pores: bursts, spikes, and steps. Bursts (orange bars) are characterized by rapid events that give a nonlinear current-voltage relationship. Spike (blue arrows) behavior is similar to the burst but is more short-lived. Step behavior is seen as a clear, defined jump in current. The activity demonstrates the heterogeneous conductance that is common for amyloids. Tracings are recorded at -50 mV bias potential with 150 mM KCl, 10 mM Hepes (pH 7.4), 1 mM $MgCl_2$ as the aqueous buffer.

Chapter 2

Activity and Architecture of Pyroglutamate Modified Amyloid-β ($A\beta_{pE3-42}$) Pores

2.1 Abstract

Among the family of $A\beta$ peptides, pyroglutamate-modified $A\beta$ ($A\beta_{pE3}$) peptides are particularly associated with cytotoxicity in Alzheimer's disease (AD). They represent the dominant fraction of $A\beta$ oligomers in the brains of AD patients, but their accumulation in the brains of elderly individuals with normal cognition is significantly lower. Accumulation of $A\beta_{pE3}$ plaques precedes the formation of plaques of full-length $A\beta$ ($A\beta_{1-40/42}$). Most of these properties appear to be associated with the higher hydrophobicity of $A\beta_{pE3}$ as well as an increased resistance to enzymatic degradation. However, the important question of whether $A\beta_{pE3}$ peptides induce pore activity in lipid membranes and their potential toxicity compared with other $A\beta$ pores is still open. Here we examine the activity of $A\beta_{pE3}$ pores in anionic membranes using planar bilayer electrical recording and provide their structures using molecular dynamics simulations. We find that $A\beta_{pE3}$ pores spontaneously induce ionic current across the membrane and have some similar properties to the other previously studied pores of the $A\beta$ family. However, there are also some significant differences. The onset of $A\beta_{pE3-42}$ pore activity

is generally delayed compared with $A\beta_{1-42}$ pores. However, once formed, $A\beta_{pE3-42}$ pores produce increased ion permeability of the membrane, as indicated by a greater occurrence of higher conductance electrical events. Structurally, the lactam ring of $A\beta_{pE3}$ peptides induces a change in the conformation of the N-terminal strands of the $A\beta_{pE3-42}$ pores. While the N-termini of wild-type $A\beta_{1-42}$ peptides normally reside in the bulk water region, the N-termini of $A\beta_{pE3-42}$ peptides tend to reside in the hydrophobic lipid core. These studies provide a first step to an understanding of the enhanced toxicity attributed to $A\beta_{pE3}$ peptides.

2.2 Introduction

The amyloid hypothesis states that accumulation of amyloid-β ($A\beta$) peptides in the brain is the primary driver of pathogenesis in Alzheimer's disease (AD), including synapse loss and neuronal cell death [110, 111, 112, 35, 18]. The full-length $A\beta_{1-42}$ peptide and its $A\beta_{17-42}$ fragment (p3) are formed via cleavage of the amyloid precursor protein (APP) by the action of three secretase enzymes [111, 36, 45]. The $A\beta_{pE3-42}$ fragment is post-translationally generated by cleavage of the first two N-terminal amino acids of $A\beta_{1-42}$, leaving an exposed glutamate (E) residue in position 3. The lactam ring in the pyroglutamate (pE) residue is subsequently generated by intramolecular dehydration catalyzed by the glutaminyl cyclase (QC) enzyme [41, 42].

pE-modified $A\beta$s represent the dominant fraction of $A\beta$ oligomers in brains of AD patients [41, 42]. Autopsied brains of elderly patients with normal cognition also show accumulation of $A\beta_{1-40/42}$, but the amount of accumulated $A\beta_{pE3-42}$ is significantly lower [113, 114, 115]. Consequently, the ratio of $A\beta_{pE3-42}$/$A\beta_{1-42}$ oligomers is higher in AD brains than in brains of normal elderly individuals [41, 42, 113, 114, 115]. The larger accumulation of $A\beta_{pE3-42}$ in AD brains has been attributed to its increased stability and higher aggregation propensity [41, 42]. These properties are attributed to the lactam ring in the pE-modified third residue as well as the loss of electrical charge in three residues during the conversion of $A\beta_{1-42}$ to $A\beta_{pE3-42}$, thus resulting in higher $A\beta_{pE3-42}$ hydrophobicity and increased resistance to degradation by peptidases [41, 42]. Significantly, it is also believed that the formation of $A\beta_{pE3-42}$ plaques precedes $A\beta_{1-42}$

plaque formation [42]. This is supported by the observation that $A\beta_{pE3-42}$ plaques appear earlier than $A\beta_{1-40/42}$ plaques in Down syndrome (DS) brains [41, 42]. The additional copy of chromosome 21, characteristic of DS, is responsible for generating more APP, and thus individuals with DS are more likely to develop AD earlier in life [110].

Increasing evidence suggests that following initial interactions on the cell membrane, $A\beta$ oligomers insert into the membrane and form pore structures [57, 59, 116, 94, 86, 22, 25, 117, 118, 81]. Cell toxicity results from an abrupt change in cell ionic concentration, producing loss of cell homeostasis. Pore activity has been observed for full-length $A\beta$s [57, 59, 48, 23, 82, 87], $A\beta$ fragments [45, 65, 119, 85, 46, 89], and point substitutions [45, 83, 82]. In addition to pore formation, $A\beta$-induced toxicity mechanisms include lipid extraction by peptides on the membrane surface [120, 79]. These mechanisms are not mutually exclusive, as a recent study suggested that pore formation precedes nonspecific fragmentation of the lipid membrane during amyloid fiber formation [121].

To the best of our knowledge, there is currently no experimental data for amyloid pore formation in vivo. $A\beta_{pE3-42}$ was observed to induce neurodegeneration and lethal neurological deficits in transgenic mice [122]. These $A\beta_{pE3-42}$ mice displayed a significantly reduced survival rate compared with $A\beta_{1-42}$ transgenic mice [122]. In vitro, optical patch-clamping was used to characterize the single-channel Ca^{2+} fluorescence transients induced by $A\beta_{1-42}$ pores in membranes of *Xenopus laevis* oocytes [86]. However, most experimental evidence of amyloid pore formation stems from model membrane studies.

Here we characterize the electrical properties of pE-modified $A\beta$ in lipid membranes. We discuss the activity and structure of $A\beta_{pE3-42}$ pores in anionic model cell membranes. We used phosphoethanolamine (PE) and phosphoserine (PS) lipid headgroups to mimic the brains of elderly patients. Phospholipids with ethanolamine (PE) head groups are one of the dominant components in the brains of the elderly [123], and these levels, as well as those of PS [124], have been found to change in AD brains [125, 126]. Using planar lipid bilayer (PLB) electrical recording, we show that $A\beta_{pE3-42}$ induces pore activity in anionic membranes, producing increased membrane permeability with respect to $A\beta_{1-42}$ pores. Using atomistic molecular dynamics (MD) simula-

tions, we model the architecture of $A\beta_{pE3-42}$ pores and correlate them with the activity observed experimentally.

2.3 Methods

$A\beta_{pE3-42}$ was purchased from Bachem (Torrance, CA), and $A\beta_{1-42}$ was purchased from Bachem and Anaspec (Fremont, CA). The phospholipids 1,2-dioleoyl-*sn*-glycero-3-phosphoserine (DOPS) and 1-palmitoyl-2-oleoyl-*sn*-glycero-3-phosphoethanolamine (POPE) were purchased from Avanti Polar Lipids (Alabaster, AL). All other chemicals were purchased from Sigma-Aldrich (St. Louis, MO).

2.3.1 Peptide Handling

$A\beta_{pE3-42}$ and $A\beta_{1-42}$ peptides were dissolved in Milli-Q water to a concentration of 1 mg/mL prior to being aliquoted for storage. These 50 μL aliquots were stored at -80° C for a maximum of 60 days before use. Samples were thawed only once.

2.3.2 Planar Lipid Bilayer Electrical Recording

We prepared PLBs using the so-called "painted" technique [96]. Bilayers were formed from a 1:1 (w/w) mixture of DOPS and POPE in heptane at a total lipid concentration of 20 mg/mL. Spontaneous membrane formation occurs following the addition of lipid directly over a pore with a diameter of $\sim$250 μm in a Delrin septum (Warner Instruments, Delrin perfusion cup, volume 1 mL). In previous studies, this membrane composition was shown to be stable for long recording times ($>$ 4 h) [90]. As the electrolyte, we use 150 mM KCl, 10 mM HEPES (pH 7.4), and 1 mM MgCl2.

Before performing electrical recordings, we verified that the bilayer was stable for several minutes with low conductance (<10 pS) across $\pm$100 mV applied voltage and that the system capacitance was >110 pF. When both criteria were met, peptide was added directly to the *cis* (hot wire) side and stirred for 5 min. Peptide concentration in the bilayer chamber was $\sim$10 μM. Bilayer stability was monitored by periodic capacitance measurements throughout the course of the experiment.

All traces were recorded in voltage clamp mode using the 2 kHz built-in filter cutoff of our BC-535 amplifier (Warner Instruments, Hamden, CT). A sampling frequency of 15 kHz was used for all data acquisition. We used a custom-made LabVIEW program to record the current and Clampfit 10.2 (Molecular Devices, Sunnyvale, CA) to analyze traces. For representation in Figures, we have filtered the recorded current versus time traces with a digital Gaussian low-pass filter with a cutoff frequency of 50 Hz.

2.3.3 Atomistic Molecular Dynamics Simulations

Two U-shaped $A\beta$ monomer conformations with the β-strand-turn-β-strand motif were extracted from $A\beta_{1-42}$ fibrils, where the structure was defined by hydrogen/deuterium-exchange NMR data, side-chain packing constraints from pairwise mutagenesis, ssNMR and EM (PDB code: 2BEG) [127], and small Aβ_{1-40} protofibrils (PDB codes: 2LMN and 2LMO) [128], where the structure was based on a ssNMR model. In both structures, the N-terminal coordinates, residues 1-16 for the former and 1-8 for the latter structure, are missing due to disorder. We used the Aβ_{1-16} coordinates, in the absence of Zn^{2+} (PDB code: 1ZE7) [129], for the missing portions of the peptides. For each combination of the N-terminal structure with the U-shaped motifs, two $A\beta_{1-42}$ conformers were generated [82, 87, 83]. Conformer 1 has a turn at Ser26-Ile31, and conformer 2 at Asp23-Gly29. In the latter conformer, two C-terminal residues, Ile41 and Ala42, were added to create $A\beta_{1-42}$. To simulate pE, we removed the first two residues, Asp1 and Ala2, from each conformer and converted Glu3 into pE3, generating $A\beta_{pE3-42}$. Because the standard CHARMM [130] force field does not provide a force field for pE, we first created the pE molecular topology using the Avogadro software [131]. Then, we calculated partial charges, bond lengths, angles, and torsional angles for the atoms in the pE residue using the Gaussian09 program [132] on a Biowulf cluster at the NIH. The calculated parameters can be directly adopted in the CHARMM [130] program.

Two $A\beta_{pE3-42}$ conformers, each derived from the wild-type (WT) $A\beta_{1-42}$ conformers with different turns, still retain the U-shaped structure with the β-strand-turn-β-strand motif. To construct $A\beta_{pE3-42}$ barrel structures, we inclined $A\beta_{pE3-42}$ monomers

$\sim$37° relative to the pore axis [89]; then, an 18-fold rotational symmetry operation was performed with respect to the pore axis creating an 18-mer $A\beta_{pE3-42}$ barrel (Figure 2.1). We modeled $A\beta$ barrels with the β-sheet structure by mimicking naturally occurring β-barrels observed in transmembrane proteins that are found frequently in the outer membranes of bacteria, mitochondria, and chloroplasts. The β-barrel motif is a large β-sheet composed of an even number of β-strands. Some known structures of β-barrel membrane proteins have β-strands ranging in size from 8 to 22 [133]. We modeled 18-mer $A\beta$ barrels, with 18 β-strands enclosing the solvated pore. This number is also in the range of the number of β-strands for natural β-barrels ranging from 8 to 22, which can form a β-barrel motif. Our previous simulations for $A\beta$ channels indicate that different numbers of $A\beta$ monomers could produce channels with different outer and pore dimensions [45, 82, 87, 85, 46, 89, 83, 90, 134, 135, 136, 137]. We found that $A\beta$ channels obtained a preferred size range of 16-24 β-strands lining the pores [85, 46] This range was also found to hold for other toxic β-sheet channels: K3 channels with 24 β-strands [50], 18- and 24-mer hIAPP channels [138], 26 PG-1 channels with 16-20 β-strands [56, 139], and MAX channels with 20 β-strands [140]. In agreement with AFM data, these channels have outer and pore dimensions within the range found with AFM. In this work, the outer/pore diameters of the 18-mer $A\beta_{pE3-42}$ barrels are in good agreement with the experimental AFM ranges [23] and the computational 18-mer wild-type $A\beta$ barrels [82, 83]. The AFM experiments provide images of channels with a wide variety of sizes and shapes, but simulated $A\beta$ barrels are limited to cover all ranges of channel sizes that are imaged by AFM.

To obtain a lipid bilayer, we constructed a unit cell containing two layers of lipids. In the middle of the unit cell, lipid molecules were randomly selected from the library of the preequilibrated state and replaced by pseudo vdW spheres at the positions of the lipid headgroups, constituting the lipid bilayer topology [141]. For a given number of lipid molecules, the optimal value of lateral cell dimensions can be determined. An anionic lipid bilayer composed of DOPS and POPE with a mole ratio 1:2, containing a total of 420 lipids constitutes the unit cell with TIP3P waters added at both sides. Updated CHARMM [130] all-atom additive force field for lipids (C36) [142] and the modified TIP3P water model [143] were used to construct the set of starting points and

to relax the systems to a production-ready stage. The system contains Mg^{2+}, K^{+}, Ca^{2+}, and Zn^{2+} at the same concentration of 25 mM to satisfy a total cation concentration near 100 mM. The bilayer system containing an $A\beta_{pE3}$ barrel, lipids, salts, and water has almost 200,000 atoms. We generated at least 10 different initial configurations for each conformer $A\beta_{pE3-42}$ barrel for the relaxation process to obtain the best initial configuration for a starting point. In the pre-equilibrium stages, a series of minimizations was performed for the initial configurations to remove overlaps of the alkane chains in the lipids and to gradually relax the solvents around the harmonically restrained peptides. The initial configurations were gradually relaxed through dynamic cycles with electrostatic cutoffs (12 Å). The harmonic restraints were gradually diminished with the full Ewald electrostatics calculation and constant temperature (Nosé–Hoover) thermostat/barostat at 303K. For $t < 30$ ns, our simulation employed the NPAT (constant number of atoms, pressure, surface area, and temperature) ensemble with a constant normal pressure applied in the direction perpendicular to the membrane. After $t = 30$ ns, the simulations employed the NPT ensemble. Production runs of 100 ns for the starting points with the NAMD code [144] were performed on a Biowulf cluster at the NIH. Averages were taken after 30 ns, discarding initial transients. Analysis was performed with the CHARMM programming package [130].

2.4 Results

2.4.1 Pore Activity

PLB electrical recording data demonstrate that $A\beta_{pE3-42}$ peptides induce spontaneous pore activity through lipid membranes presenting the general features observed for $A\beta_{1-42}$ pores (Figure 2.2). At a concentration of 10 μM and at constant voltage both peptides show stepwise changes in the current flowing through the membrane (Figure 2.2A), characteristic of the opening and closing of ion channels. However, unlike ion channels that have regulated activity and possess integer values of a unitary conductance, amyloid pores are not regulated and present multiple conductance values due to the different number of monomers composing the pore and membrane-channel interaction dynamics [85]. The multilevel conductance seen here in both $A\beta_{pE3-42}$ and $A\beta_{1-42}$

is a hallmark of amyloid pores [23].

For both peptides, two distinct types of activity were observed. The first, as seen in Figure 2.2, was characterized by stable, long recording times (>30 min) following the first onset of activity. The second type of activity was characterized by ionic conduction through the membrane that grows rapidly in an exponential-like fashion (Figure 2.3A). When present, this "exponential" phase began within 20 min of the first observed activity and typically led to current saturation of the amplifier within 10 min. This type of growth was seen in 50% (3/6) of $A\beta_{pE3-42}$ and 33% (2/6) $A\beta_{1-42}$ membranes (Table 2.1). At first, only a few pores open (Figure 2.3B), and the membrane stays in the same conductive state for several 10s of seconds (region inside grey rectangle). However, after an abrupt increase in the membrane conductivity due to the opening of a large single pore or several pores simultaneously, the activity is characterized by several short small steps only a few seconds long, suggestive of the opening of several pores in a cascade-like fashion. Despite this rapid growth, discrete steps indicative of pore activity are still clearly observed (Figure 2.3C). In addition, similar to $A\beta_{1-42}$, $A\beta_{pE3-42}$ pores are voltage-independent and can be blocked by Zn^{2+} (Figure 2.3A).

Although the overall characteristics of the membrane activity induced by $A\beta_{pE3-42}$ and $A\beta_{1-42}$ pores are similar, distinct differences are present. Table 1 displays the characteristic parameters observed for the electrical activity of both $A\beta_{pE3-42}$ and $A\beta_{1-42}$. The onset of $A\beta_{1-42}$ activity in PLB can be observed as soon as several minutes following peptide addition into the chamber and was typically seen within $\sim$60 min post-addition with an average of 31.6 ± 25.7 min. $A\beta_{pE3-42}$ demonstrated a significantly longer ($p < 0.05$ for a one-tail t test) and more variable lag time, with an average of 98.2 ± 68.5 min.

We next examined whether there was a difference between $A\beta_{pE3-42}$ and $A\beta_{1-42}$ channel conductances. Figure 2.4 shows the histogram distribution of single-channel conductances calculated from both step and spike activity. The histograms show that the conductances can be sorted into three groups that demonstrate a shift toward higher conductances for $A\beta_{pE3-42}$ pores (Figure 2.4A) compared with $A\beta_{1-42}$ (Figure 2.4B). The first group of conductances, below 100 pS, consisted of 74% of $A\beta_{pE3-42}$ and 91% of $A\beta_{1-42}$ events. The second group is between 100 and 200 pS and, significantly,

shows a second peak of activity for $A\beta_{pE3-42}$ that is absent for $A\beta_{1-42}$. While 21% of the events fall in this range for $A\beta_{pE3-42}$, only 5% of $A\beta_{1-42}$ events are in this range. The third grouping shows similar rates of sparse activity greater than 200 pS (5 and 4% for $A\beta_{pE3-42}$ and $A\beta_{1-42}$, respectively). While the percentage of activity in the high conductivity range is similar, close inspection of the histogram shows higher conductances for $A\beta_{pE3-42}$ in this region. (Note the additional grouping around 600 pS.) Table 2.1 shows that the average conductance in this third region is $\sim$20% higher for $A\beta_{pE3-42}$. These results show an overall trend for higher $A\beta_{pE3-42}$ conductance, which could have relevance to the $A\beta_{pE3-42}$ toxicity mechanism.

2.4.2 $A\beta_{pE3-42}$ Barrel Conformations in the Lipid Bilayer

We performed 100 ns all-atom MD simulations on $A\beta_{pE3-42}$ barrels embedded in an anionic lipid bilayer composed of DOPS/POPE (mole ratio 1:2). The $A\beta_{pE3-42}$ barrels comprising two different U-shaped conformers were initially preassembled as an annular shape. The initial annular conformation is gradually lost via relaxation of the lipid bilayer, and no immediate peptide dissociation in the barrels was observed (Figure A.1). The U-shaped portions of the $A\beta_{pE3}$ barrels (residues 15-42 and 11-42 for the conformer 1 and 2 $A\beta_{pE3-42}$ barrels, respectively; see peptide topologies in Figure 2.1), which mostly include membrane embedded portions, reach equilibration after the initial transient state, while the extramembranous N-termini of the peptides (residues 3-14 and 3-10 for the conformer 1 and 2 $A\beta_{pE3-42}$ barrels, respectively) are disordered (Figure A.2). Small fluctuations in the pore and C-terminal strands in the lipid bilayer retain the U-shaped peptide motif in the $A\beta_{pE3-42}$ barrels (Figure A.3). In our simulations, the $A\beta_{pE3-42}$ peptide also presents heterogeneity in barrel conformations (Figure 2.5), as observed in the WT $A\beta_{1-42}$ [82, 87] and mutant [83, 82, 137] $A\beta$ barrels. The outer diameters for the membrane embedded portion are $\sim$7.6 and $\sim$7.1 nm for the conformer 1 and 2 $A\beta_{pE3-42}$ barrels, respectively. The averaged pore diameters are $\sim$2.2 and $\sim$1.9 nm for the conformer 1 and 2 $A\beta_{pE3-42}$ barrels, respectively. Both outer/pore diameters of $A\beta_{pE3-42}$ barrel are in the range of the WT barrel [82, 87, 134].

Unlike the WT $A\beta_{1-42}$ barrels, where the N-terminal strands normally reside in the bulk water area (Figure A.4), the pE3 N-termini of $A\beta_{pE3-42}$ barrels tend to retreat

to the lipid hydrophobic core due to the hydrophobicity of the lactam ring. To locate the pE3 residue across the bilayer, we calculated the probability distributions for pE3 as well as few selected charged groups in the barrels (Figure 2.6). The distribution curves for pE3 spanning the interior of the lipid bilayer indicate that several pE3 termini interact with the lipid hydrophobic tails. The interaction energy of the pE3 residue with lipids shows strong attraction for several pE3 N-termini (blue bars in Figure A.5), while no strong lipid interactions of the standard N-termini were observed in the WT $A\beta_{1-42}$ and mutant barrels [82, 87, 83, 137]. Relocating the pE3 N-termini into the lipid hydrophobic core significantly reduces the fluctuations of the N-terminal portions of barrels at the lower bilayer leaflet, further stabilizing the barrel conformation. With the pE3 anchoring in the membrane, the $A\beta_{pE3-42}$ barrel would provide a clear channel mouth at the lower bilayer leaflet and hence yield a wide-open water pore for ion leakage, suggesting that $A\beta_{pE3-42}$ pores may lead to high ion conductance.

To observe ion activity in the $A\beta_{pE3-42}$ pores, we calculated the probability distribution for ions across the bilayer (Figure A.6). Peaks in the distribution curves reflect the highly populated ion binding sites in the pore. The locations of ion binding sites in each conformer $A\beta_{pE3-42}$ barrel are similar to those of each corresponding conformer of WT $A\beta_{1-42}$ barrels because both barrels share the same U-shaped motif in the lipid bilayer. To observe ion fluctuation across the pore, we calculated the change in total charge in the pore as a function of the simulation time (Figure 2.7). Two selected pore lengths along the pore axis, $-1.0 < z < 1.0$ nm and $-1.8 < z < 1.8$ nm, were used in the calculation. These pore lengths ensure that the charge fluctuations exclude a contribution of ion interactions with the lipid head groups. For $|z| < 1.0$ nm, the pore of the $A\beta_{pE3-42}$ barrel conformer 1 exhibits larger charge fluctuations than the conformer 2 barrel, because the Glu22 cationic binding site is located at $z \approx 0.6$ nm, attracting more cations into the pore. For the conformer 2 $A\beta_{pE3-42}$ barrel, the Glu22 cationic binding site is located at $z \approx 1.8$ nm near the channel mouth (as indicated by Ca^{2+} peak at $z \approx 1.8$ nm in Figure A.5B). To correlate these charge fluctuations with experimental ion conductance, we calculated the maximum conductance, g_{max} [145], representing the

ion transport, which can be described as

$$g_{max} = \frac{q_e^2}{k_B T L^2} \langle D(z) e^{G_{PMF}(z)/k_B T} \rangle^{-1} \langle e^{-G_{PMF}(z)/k_B T} \rangle^{-1} \tag{2.1}$$

where q_e is the elementary charge, k_B denotes the Boltzmann's constant, T is the simulation temperature, and L represents the pore length of 36 Å. In the bracket, $D(z)$ and $G_{PMF}(z)$ denote the 1D diffusion coefficient and the 1D potential of mean force for ions, respectively. For Mg^{2+}, K^+, Ca^{2+}, and Zn^{2+}, the maximum conductances are 667, 338, 115, 155 pS and 137, 271, 92, 89 pS in the pores of conformers 1 and 2 $A\beta_{pE3-42}$ barrels, respectively. Averaged maximum conductances for ions are relatively higher than those calculated for the WT $A\beta_{1-42}$ barrels [87].

2.5 Discussion

We have shown that the toxic pE-modified $A\beta$ peptides produce pore activity in DOPS/POPE anionic membranes. These pores demonstrate similar activity characteristics (heterogeneous step, spike and burst conductance, Zn^{2+} blockage) as $A\beta_{1-42}$ pores as well as other previously studied pores of the $A\beta$ family. However, there are also some significant differences. The onset of $A\beta_{pE3-42}$ pore activity is generally delayed, but once started, $A\beta_{pE3-42}$ pores show increased propensity for larger conductance events compared with $A\beta_{1-42}$ pores, particularly in the 100-200 pS range (Figure 2.4). Structurally, the lactam ring of $A\beta_{pE3}$ peptides induces a change in the conformation of the N-terminal strands of the $A\beta_{pE3-42}$ pores. While the N-terminal strands of $A\beta_{1-42}$ pores normally reside in the bulk water region, the N-termini of $A\beta_{pE3}$ pores tend to reside in the hydrophobic lipid core, providing the $A\beta_{pE3-42}$ pores with higher stability.

The longer times required for the onset of $A\beta_{pE3-42}$ pore activity are tentatively attributed to (i) the higher hydrophobicity of $A\beta_{pE3-42}$, which decreases the attractive charge-dipole interactions with the zwitterionic lipid heads, thus also decreasing the number of adsorbed $A\beta_{pE3-42}$ oligomers available for subsequent membrane insertion, and (ii) the possible longer times required for pores to assemble in the membrane. Our PLB data demonstrate that the ionic current produced by $A\beta_{pE3-42}$ pores can rapidly rise to levels potentially toxic for cells. Following pore formation, cytotoxicity is produced

by an abrupt change in cell ionic concentration. According to early estimations [57, 59], a single pore with a gigantic 4 nS conductance can produce a change of 10 μM/s in internal Na^+ concentration, producing loss of cell homeostasis in seconds. While no single catastrophic event of this nature was observed (Figure 2.4), the summation of smaller ionic conductance events can have a similar toxic effect. $A\beta_{pE3-42}$ has been shown to be more cytotoxic than $A\beta_{1-42}$ in vitro [122, 146]. We showed that $A\beta_{pE3-42}$ shows a greater propensity for higher conductance values when compared with $A\beta_{1-42}$. This would lead to a more prevalent and rapid dysregulation of cellular ionic homeostasis for $A\beta_{pE3-42}$, thus suggesting increased cytotoxic properties of $A\beta_{pE3-42}$ pores.

The pore structures found for $A\beta_{pE3-42}$ had characteristics and dimensions in accordance with the pores previously reported. Pore structures have been characterized by AFM and modeled using MD simulations for several $A\beta$ peptides. Our previous studies indicate that full-length $A\beta_{1-40/42}$ [48, 23, 82, 87], certain $A\beta$ mutants [23, 83], $A\beta$ fragments [45, 81, 119, 85, 46, 89], as well as other amyloids [48, 23, 50, 56, 44] form heterogeneous pore structures showing 4-6 subunits and shapes varying from rectangular to hexagonal. Our MD simulations suggest similar pore sizes for both peptides but increased stability of the $A\beta_{pE3-42}$ pores inserted in DOPS/POPE membranes. Stability in the membrane is likely more important for the formation and longevity of the larger pores with conductances in the 100-200 pS range. As a result, $A\beta_{pE3-42}$ pores with conductances in this range have a higher population than $A\beta_{1-42}$ pores (Figure 2.4). Pores with conductances $>$ 200 pS likely have similar and fast decay rates for $A\beta_{pE3-42}$ and $A\beta_{1-42}$, and thus both populations are similarly low, although still somewhat larger for $A\beta_{pE3-42}$. Such a scenario would also correlate with the greater in vitro cytotoxicity observed for $A\beta_{pE3-42}$ peptides.

The energy of a pore according to the continuum model is [147]

$$E = \gamma 2\pi r - \sigma \pi r^2, \tag{2.2}$$

where r is the pore radius, *gamma* is the line tension at the pore edge, and σ is the surface tension of the membrane. Our MD results indicate that $A\beta_{pE3-42}$ and $A\beta_{1-42}$ pores have similar diameters and general characteristics, while the main difference is the retreat of the N-termini of $A\beta_{pE3-42}$ into the hydrophobic lipid core. Therefore, this

reconfiguration of the N-termini likely decreases the line tension of $A\beta_{pE3-42}$ pores, minimizing their pore energy and rendering them more stable.

Our results suggest potential mechanisms of cellular disruption. The "exponential" growth of the current, seen in Figure 2.3, would lead to rapid cell death and was observed in 50% (3/6) of the $A\beta_{pE3-42}$ membranes in this study. While pore activity appears to be the only mechanism present during the early stages (grey rectangle in Figure 2.3B), the activity trace suggests that two mechanisms of ionic conductance act simultaneously during exponential saturation: (i) stepwise pore behavior and (ii) nonspecific drift leakage. The nonspecific leakage could be caused by a number of alternative mechanisms leading to $A\beta$-induced membrane permeability, including carpeting and detergent effects [79]. The data suggest that a combined mechanism (pore and nonspecific leakage) may be at work during the rapid growth of the "exponential" phase, at least some of the time. It is important to note that similar behavior was also seen for some of the $A\beta_{1-42}$ membranes. Although this behavior was observed for more membranes with $A\beta_{pE3-42}$ pores, this difference (Table 2.1) was not statistically significant to reach conclusions regarding specific $A\beta_{pE3-42}$ cytotoxity.

2.6 Conclusion

In summary, using PLBs and MD simulations, we have shown that $A\beta_{pE3-42}$ forms ionic pores in DOPS/POPE lipid bilayers. The activity of these pores follows the same general pattern as $A\beta_{1-42}$ pores. Significantly, however, $A\beta_{pE3-42}$ pores display higher conductances than $A\beta_{1-42}$ pores, in particular, in the 100-200 pS range. In addition, the onset of $A\beta_{pE3-42}$ pore activity is delayed compared with $A\beta_{1-42}$ pores. Structurally, $A\beta_{pE3-42}$ and $A\beta_{1-42}$ pores have similar dimensions, but the pE3 residue induces a change in the conformation of the N-terminal strands of the $A\beta_{pE3-42}$ pores. While the N-terminal strands of $A\beta_{1-42}$ pores normally reside in the bulk water region, the N-termini of $A\beta_{pE3}$ pores tend to reside in the hydrophobic lipid core, providing the $A\beta_{pE3-42}$ pores with higher stability compared with the $A\beta_{1-42}$ pores. These studies are a first step in understanding the role of pores in the enhanced toxicity attributed to $A\beta_{pE3}$ peptides.

2.7 Associated Content

Time series of $A\beta_{pE3-42}$ barrel conformations is shown in Figure A.1. Peptide-averaged and residue-averaged RMSDs are shown in Figures A.2 and A.3, respectively. Probability distribution functions for selected residues in the wild type barrels are shown in Figure A.4. Interaction energy of pE3 residue with lipids is shown in Figure A.5. Probability distribution functions for ions are shown in Figure A.6.

Chapter 2 in full is a reprint of the material *Gillman, A.L., Jang, H, Lee, J., Ramachandran, S., Kagan, B.L., Nussinov, R., and Arce, FT. Activity and Architecture of Pyroglutamate-Modified Amyloid-β ($A\beta_{pE3-42}$) Pores.* J Phys Chem B *2014 118 (26), 7335-7344* The dissertation author was the primary author.

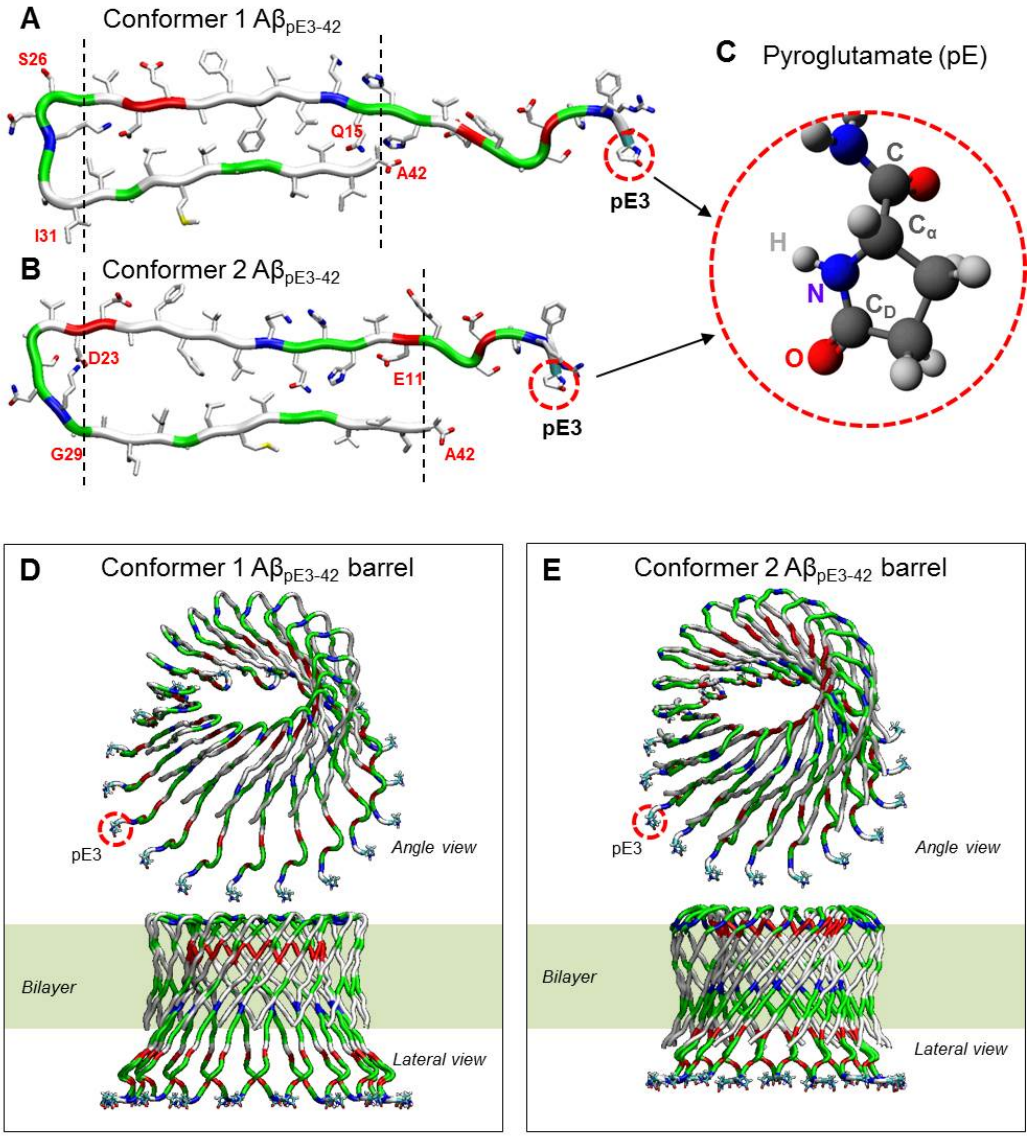

Figure 2.1: **A$\beta_{\mathbf{pE3-42}}$ monomer conformers for MD simulations.** Monomer conformations of **(A)** conformer 1 $A\beta_{pE3-42}$ with turn at Ser26-Ile31 and **(B)** conformer 2 $A\beta_{pE3-42}$ with turn at Asp23-Gly29, and **(C)** highlight of pyroglutamate at residue 3 (pE3). Dotted lines on the monomer structures denote the locations of bilayer surfaces. The initial barrel structures of MD simulations in ribbon representation for the **(D)** conformer 1 and **(E)** conformer 2 $A\beta_{pE3-42}$ barrels. In the peptide ribbon, hydrophobic, polar/Gly, positively charged, and negatively charged residues are colored white, green, blue, and red, respectively. The pE3 N-terminal termini are highlighted as threads.

Table 2.1: **Characteristic parameters of Aβ_{1-42} and Aβ_{pE3-42} electrical activity in anionic membranes**. $A\beta_{pE3-42}$ showed a greater percentage of activity at higher conductance values, in particular in the $100-200$ pS range, as well as a longer lag period between the addition of peptide and the first observed activity.

peptide	no. of membranes	total events	time to first activity (mean ± SD) (min)	% of membranes with apparent exponential current growth	% event 0-100 pS average conductance	% event 100-200 pS average conductance	% event >200 pS average conductance
$A\beta_{1-42}$	6	1192	31.6 ± 25.7	33.33	90.77% 33.25 ± 22.35 pS	4.95% 140.92 ± 27.05 pS	4.28% 362.43 ± 143.82 pS
$A\beta_{pE3-42}$	6	1400	98.2 ± 68.5	50	73.98% 34.58 ± 24.28 pS	20.87% 158.85 ± 28.43 pS	5.15% 436.97 ± 139.59 pS

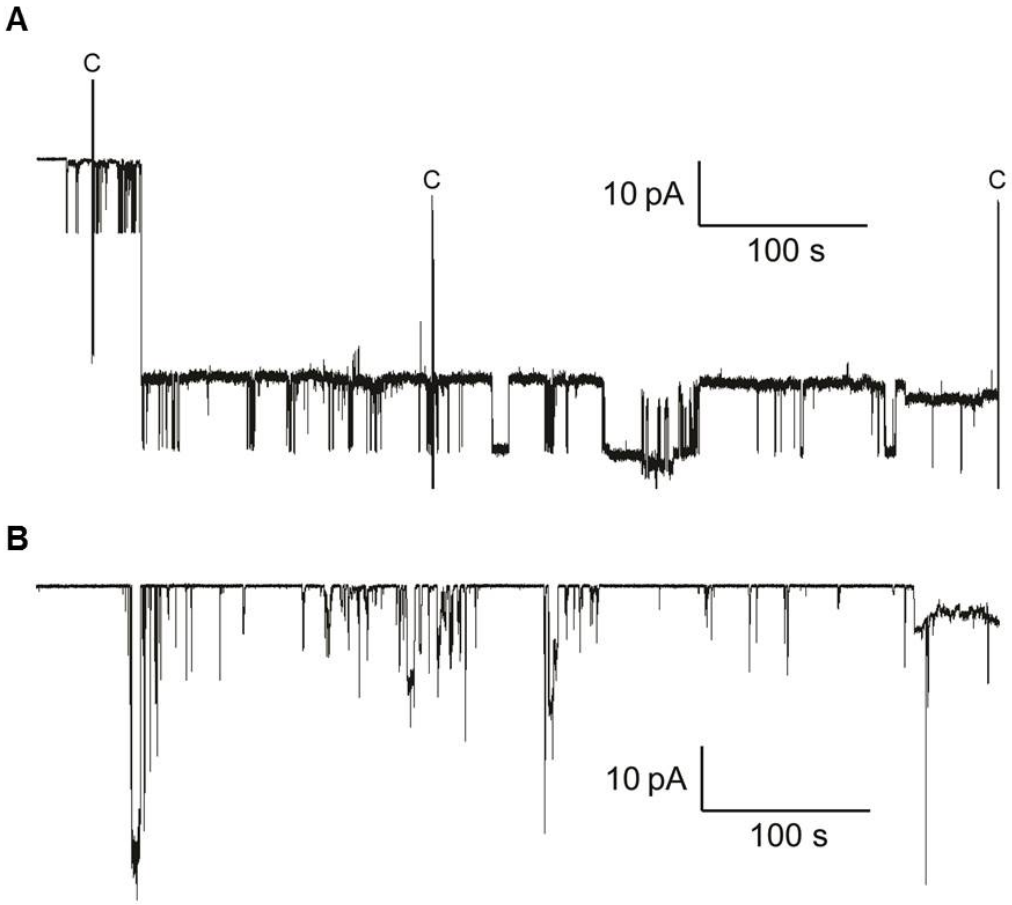

Figure 2.2: **Pore activity of $A\beta_{pE3-42}$ and $A\beta_{1-42}$.** $A\beta_{pE3-42}$ and $A\beta_{1-42}$ produce pore activity in anionic lipid membranes. Representative traces for the activity of **(A)** $A\beta_{pE3-42}$ and **(B)** $A\beta_{1-42}$ pores in stable membrane recording. These types of traces were common to both membranes. The activity seen in both membranes, namely step, spike, and burst behavior is characteristic of amyloid ion channels. Bilayers were formed by the painted technique using 1:1 (w/w) mixture of DOPS/POPE. Both sides of the bilayer chamber contained as electrolyte 150 mM KCl, 1 mM $MgCl_2$, and 10 mM HEPES (pH 7.4). -50 mV bias potential is applied.

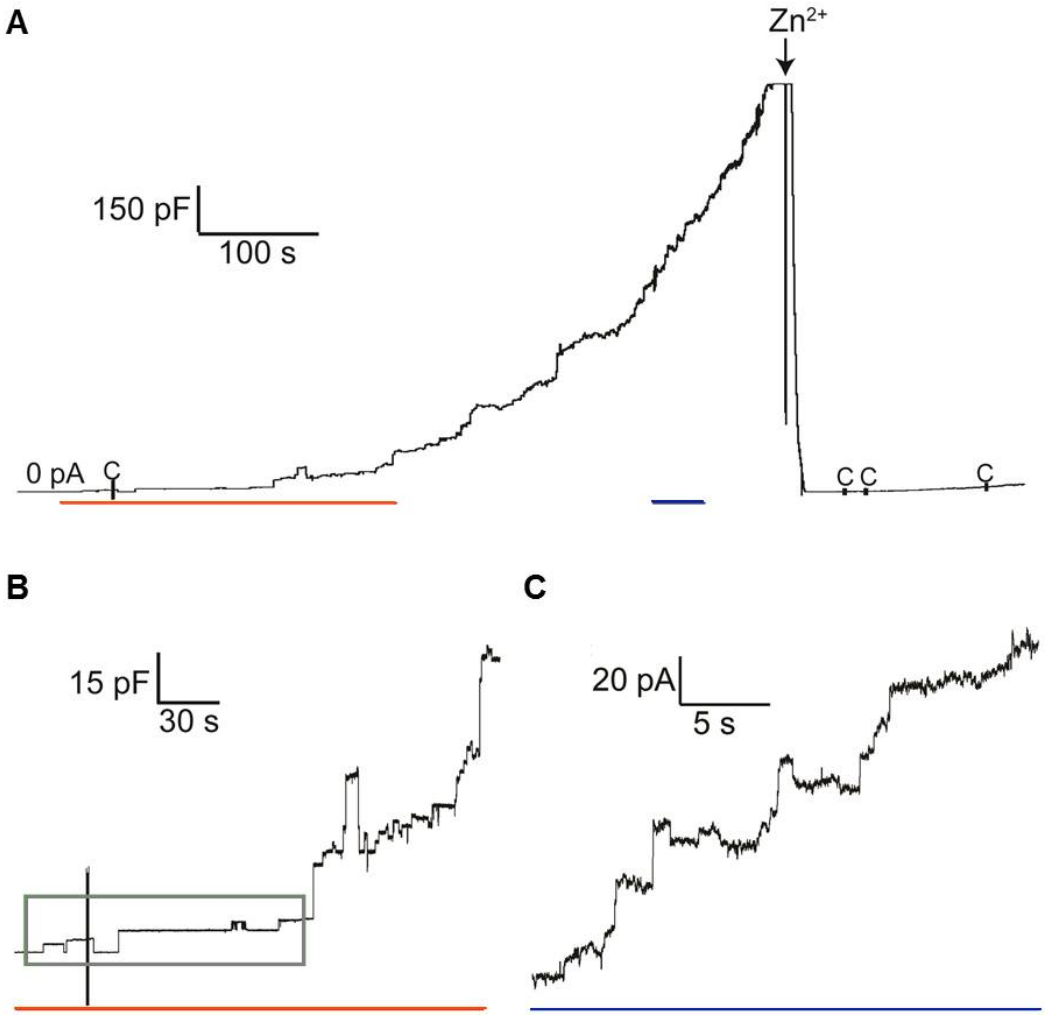

Figure 2.3: **"Exponential'" current growth of A$\beta_{\mathbf{pE3-42}}$.** A +50 mV bias potential is applied. This type of membrane activity was observed in 50% of $A\beta_{pE3-42}$ membranes and 33% of $A\beta_{1-42}$ membranes. **(A)** The current across the membrane increased rapidly upon disruption of the membrane, exceeding the 1.1 nA saturation current of our amplifier. Addition of Zn^{2+} ions rapidly inhibits $A\beta_{pE3-42}$ activity. **(B)** Enlargement of the time period indicated by the orange line. The transition from stable step behavior to "exponential" growth is highlighted. An abrupt increase in the membrane conductivity due to the opening of a large single pore or several pores simultaneously leads to the opening of several pores in a cascade-like fashion. **(C)** Clear step behavior is still observed during exponential current growth (region indicated by the short blue line in (A). A mixed mechanism involving both channel activity and nonspecific leakage is likely involved.

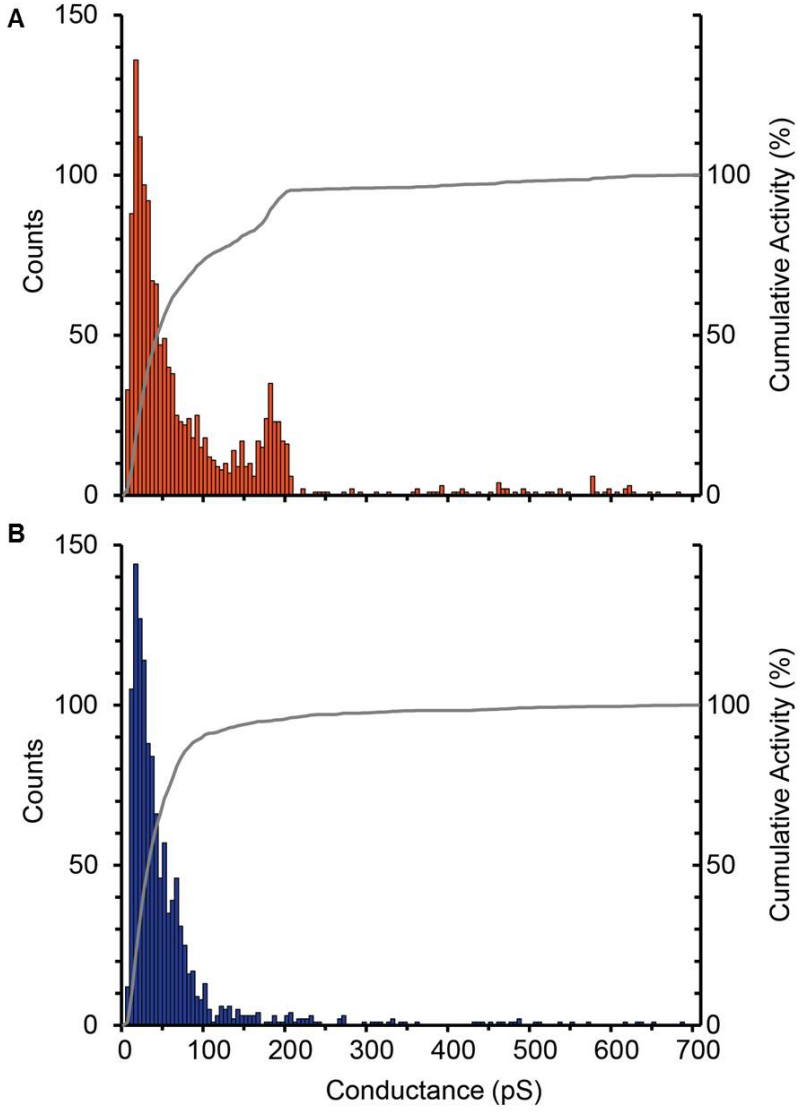

Figure 2.4: **Histogram of $A\beta_{1-42}$ vs. $A\beta_{pE3-42}$ activity.** Analysis of **(A)** $A\beta_{pE3-42}$ and **(B)** $A\beta_{1-42}$ conductances shows that there is an increased propensity for higher conductance events for $A\beta_{pE3-42}$. Both histograms are binned at 5 pS. Solid lines plot the cumulative percentage of total events. Both sets of conductances can be sorted into three groups; <100 pS, $100-200$ pS and >200 pS, as shown in Table 1.1. $A\beta_{pE3-42}$ presents significantly more events than $A\beta_{1-42}$ in the $100-200pS$ interval. Data sample size was 1400 for $A\beta_{pE3-42}$ and 1192 $A\beta_{1-42}$. Data were collected in the $\pm$50 mV range, with peptide at a concentration of 10 μM. The electrolyte used was 150 mM KCl, 1 mM $MgCl_2$, and 10 mM HEPES (pH 7.4). Bilayers were made by the painted technique with DOPS/POPE lipids dissolved in heptane.

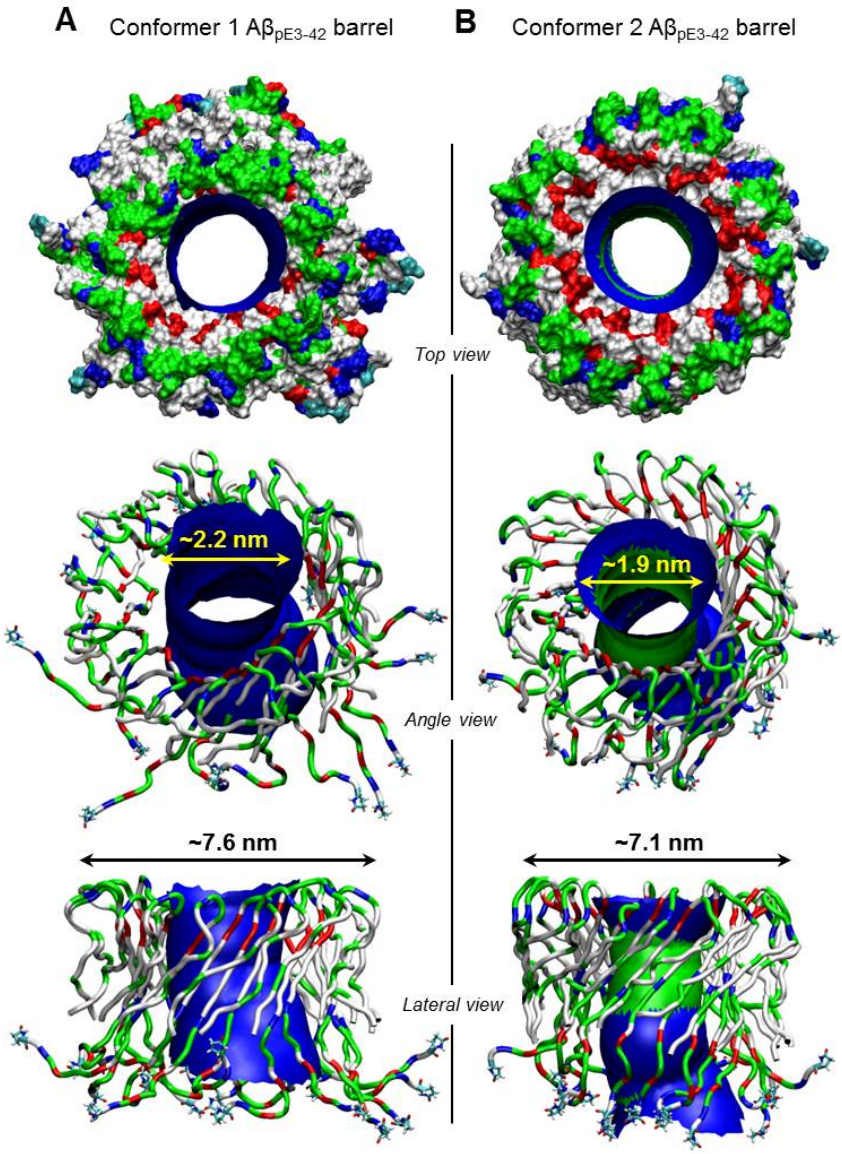

Figure 2.5: **Averaged pore structure of conformer 1 and conformer 2.** The averaged pore structures were calculated with HOLE [148] embedded in the average barrel conformations during the simulations for **(A)** conformer 1 and **(B)** conformer 2 $A\beta_{pE3-42}$ barrels. In the barrel structures with the surface (top view) and the ribbon representations (angle and lateral views), hydrophobic, polar/Gly, positively charged, and negatively charged residues are colored white, green, blue, and red, respectively. For the pore structures, red denotes pore diameter of $d < 1.4$ nm, green denotes pore diameter in the range, 1.4 nm$\leq d \leq$2.0 nm, and blue denotes pore diameter of $d > 2.0$ nm.

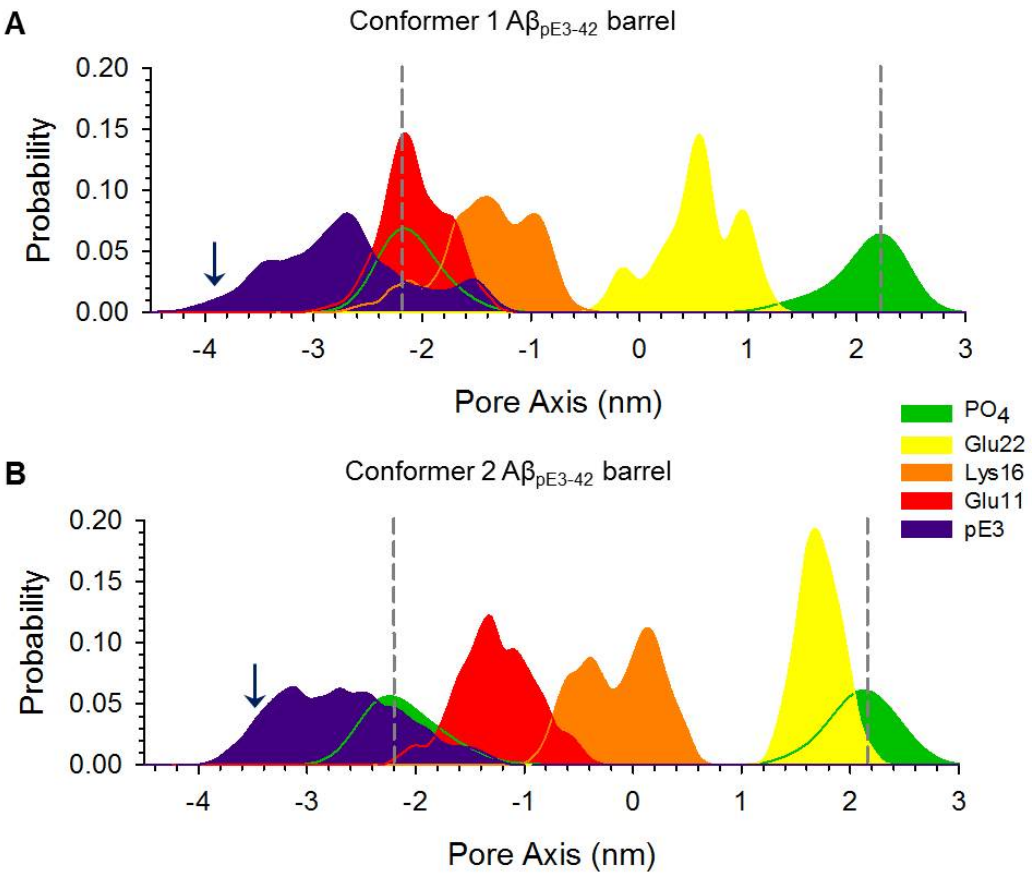

Figure 2.6: **Probability distribution functions for Aβ_{3-42} as a function of distance along the pore center axis.** pE3 (purple), Glu11 (red), Lys16 (orange), and Glu22 (yellow), and the phosphate group of lipid head, PO4 (green), are represented for **(A)** conformer 1 and **(B)** conformer 2 $A\beta_{pE3-42}$ barrels. Dotted lines indicate the locations of bilayer surfaces. Initial locations of pE3 are marked by arrows.

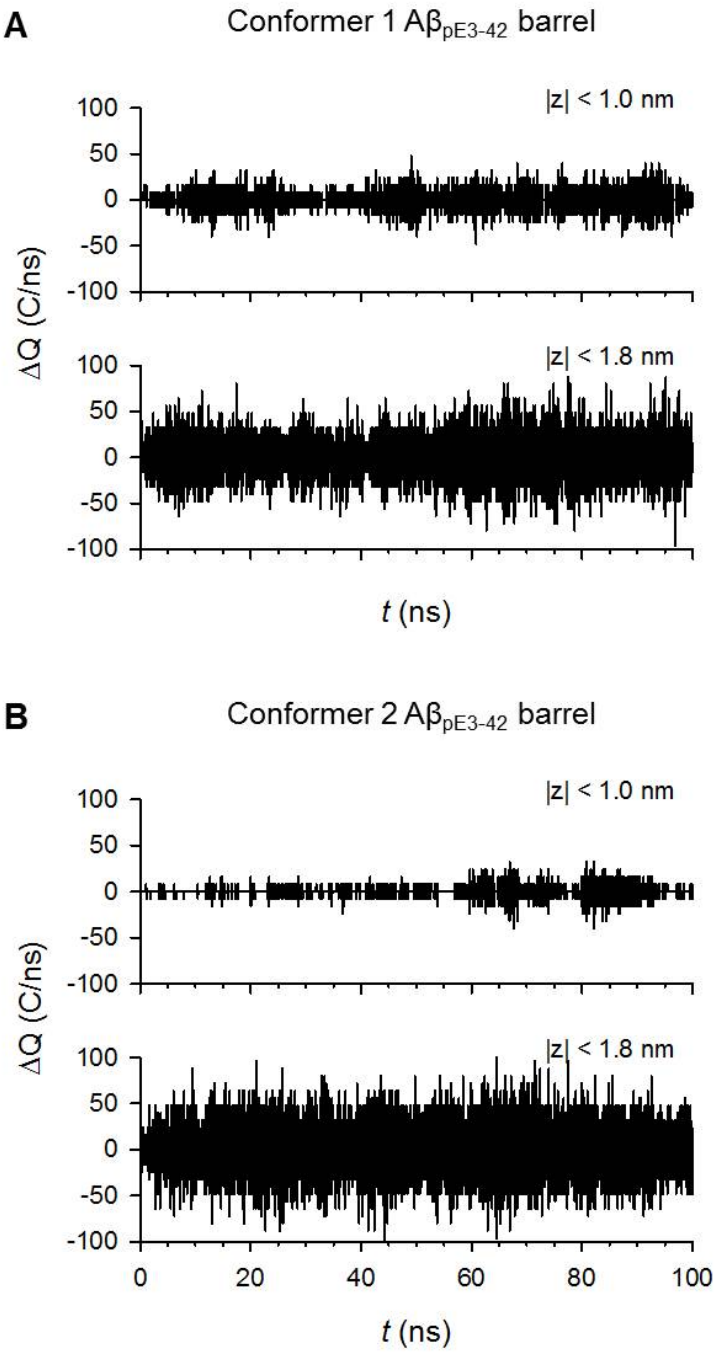

Figure 2.7: **Change in total charge in the pore as a function of the simulation time.** **(A)** conformer 1 and **(B)** conformer 2 $A\beta_{pE3-42}$ barrels. The pore heights with cutoff along the pore axis, -1.0< z < 1.0 nm and -1.8< z < 1.8 nm were used.

Chapter 3

Development of a new analytical method for quantification of $A\beta$ pore toxicity in bilayer recordings

3.1 Abstract

Ion channels are membrane protein complexes essential to signaling and communication between cells of living systems. The dysfunction of ion channels has been widely studied and directly related to the pathology of numerous diseases and has been linked to cell death in Alzheimer's disease (AD). The amyloid channel hypothesis of AD theorizes that $A\beta$ induced ionic leakage of Na^+, K^+, and Ca^{2+} could disrupt membrane potential and cellular homeostasis leading to cell death. Amyloid poration of membranes is studied electrically in model membrane systems. Unfortunately, traditional analysis of membrane channels is unsuitable for amyloid peptides. Investigation of amyloid toxicity has suffered from the lack of a quantitative analysis that directly links changes in ionic current to cytotoxicity and provides a benchmark for comparison between peptide species. Comparison of amyloid pore activity is most often accomplished via histograms of the single channel conductance for the ensemble, which is not necessarily a good indicator of toxicity. To address this issue, here we present a custom analysis program that determines the total ionic conductance across the membrane. As

proof of principle for our system, we reanalyze the data from Chapter 2.

3.2 Introduction

Ion channels are essential proteins embedded within the cellular membranes of living systems. Ion channels are involved in a wide range of physiological functions including neuronal signaling, muscle contraction, cardiac pacemaking, hormone secretion, cell volume regulation and cell proliferation [149, 150, 151]. Due to their important role, dysfunctions of channel proteins are closely related to a variety of diseases. These channelopathies are often caused by mutations in the ion channel encoding genes and can lead to either a loss or a gain of channel function [149].

The cellular membrane in live cells is very complex involving many variables which are very difficult to isolate and control. Consequently, studying the ionic flux across a cellular membrane due to specific membrane proteins is extremely challenging. This is not a problem for many types of channels which exhibit well defined and uniform behavior. Through fluorescent labeling, specific channels of interest can be localized and studied within the living cell membrane. Other membrane permeabilizing peptides, such as amyloids, do not exhibit this uniform behavior [57, 23, 22, 116, 90] and cannot be studied effectively by patch-clamping. As a result, ionic flux across lipid bilayers is studied in the model BLM system. By using a model membrane we ensure a pure system that isolates specific membrane permeabilizing peptides.

The variable nature of amyloid activity introduces challenges for their analysis. No current commercial software program is capable of properly analyzing the channel activity of heterogeneous peptides, such as amyloids. While qualitative conclusions can be drawn by observing the traces, without unitary conductance, quantitative assessment is time consuming and labor intensive. As demonstrated in Chapter 2 (Figure 2.4), histogram analysis of single channel conductivity is often used to characterize $A\beta$ channels and is used as a means to compare toxicity between various species [90, 91]. The matter of analyzing $A\beta$ cytotoxicity is complicated by the different activity types highlighted in Figure 1.6 (spike, burst, step) [22, 107], which could erroneously bias histogram analysis toward prevalent but short lived pores that may not hold significance to dysregulation

of cellular ionic balance. Furthermore, in addition to pore formation, $A\beta$-induced toxicity mechanisms include lipid extraction by peptides on the membrane surface [120, 79]. These mechanisms are not mutually exclusive, as a recent study suggested that pore formation precedes nonspecific fragmentation of the lipid membrane during amyloid fiber formation [88]. For these reasons, current techniques make it difficult to draw conclusions about amyloid peptide cytotoxicity from the BLM alone and even more challenging to make meaningful comparisons between different amyloid species.

The channel hypothesis of $A\beta$ toxicity suggests that ionic leakages of Na^+, K^+, and Ca^{2+} could disrupt membrane potential and cellular homeostasis leading to cell death [57, 59, 61]. Initial calculations by Arispe et al. show that a giant 4 nS channel could cause the intracellular concentration of each of these ions to change by as much as 10 μM/s, leading to irreversible disruption of cellular homeostasis in a matter of seconds [57]. From this it is clear that the total ionic total flux through the bilayer is the key parameter that should be analyzed with respect to cytotoxicity. To address this issue, we have developed a custom Python analysis program that allows for more accurate understanding of the characteristics and behavior of amyloid channels. Proper understanding of toxicity will improve diagnosis, therapeutic development, and ultimately the prevention of amyloid channel diseases and disorders. As proof of concept for the program, here we reanalyze the data presented in Chapter 2.

3.3 Methods

3.3.1 Materials and peptide handling

As previously described in Chapter 2: $A\beta_{pE3-42}$ was purchased from Bachem (Torrance, CA), and $A\beta_{1-42}$ was purchased from Bachem and Anaspec (Fremont, CA). The phospholipids 1,2-dioleoyl-*sn*-glycero-3-phosphoserine (DOPS) and 1-palmitoyl-2-oleoyl-*sn*-glycero-3-phosphoethan-olamine (POPE) were purchased from Avanti Polar Lipids (Alabaster, AL). All other chemicals were purchased from Sigma-Aldrich (St. Louis, MO). $A\beta_{pE3-42}$ and $A\beta_{1-42}$ peptides were dissolved in Milli-Q water to a concentration of 1 mg/mL prior to being aliquoted for storage. These 50 μL aliquots were stored at -80° C for a maximum of 60 days before use. Samples were thawed only once.

3.3.2 Planar Lipid Bilayer Recording

BLM/PLB recordings of $A\beta_{1-42}$ and $A\beta_{pE3-42}$ were previously described in Chapter 2. Briefly: Painted bilayers were formed over a ~ 250 μm pore in a Delrin septum (Warner Instruments, Delrin perfusion cup, volume 1 mL) from a 1:1 (w/w) mixture of DOPS and POPE in heptane. As the electrolyte, we use 150 mM KCl, 10 mM HEPES (pH 7.4), and 1 mM $MgCl_2$. Bilayer stability was verified to ensure low conductance (< 10 pS) across ± 100 mV applied voltage and system capacitance > 110 pF. When both criteria were met, peptide was added directly to the cis (hot wire) side to a concentration of 10 μM and stirred for 5 min. Bilayer stability was monitored by periodic capacitance measurements throughout the course of the experiment. Traces were recorded in voltage clamp mode using the 2 kHz built-in filter cutoff of our BC-535 amplifier (Warner Instruments, Hamden, CT) at a sampling frequency of 15 kHz. We used a custom-made LabVIEW program to record the current and Clampfit 10.2 (Molecular Devices, Sunnyvale, CA) to analyze traces. For representation in figures, we have filtered the recorded current versus time traces with a digital Gaussian low-pass filter with a cutoff frequency of 50 Hz.

3.3.3 Software Development

Custom Python code was written to analyze the total conductance through the membrane. Total conductance was calculated by modification of the formula for conductance as given by Ohm's Law. By summing the conductance over a given time period the total ionic flux through the membrane was calculated as a right-handed Riemann sum of the area under the curve for current, as follows:

$$\Phi_g = \sum_{i=1}^{T} \frac{I_i - I_{(b|V_i)}}{V_i} \Delta t \tag{3.1}$$

where Φ_g is the total conductance, T is the total time of integration, I_i is the present value of the current, $I_{(b|V_i)}$ is the baseline current at the present voltage, V_i is the applied bias voltage, and Δt is the time step between data points. Since data is collected at discrete time points a summation rather than integral was calculated, with the summation

equaling the integral in the limit as Δt approaches 0. Total ionic flux was calculated in terms of conductance rather than charge to account for the increase in charge movement at higher voltages. To account for small fluctuations due to noise, exclusion criteria was established within the code. Any deviations below the set threshold (which can be altered by the user) do not contribute to the calculation.

An easy to navigate user interface was designed for the analysis of total conductive flux. The user workflow follows several easy steps, as highlighted in Figure 3.1. 1) Add file(s). Several files can be stitched together and the full recording time of a membrane can be viewed in a single window, something that is usually not done with other packages as the large amount of data can overwhelm the program. 2) Set the viewer window limits. The time (x) axis zoom is adjusted with the sliders at the bottom of the screen while the current (y) axis is adjusted by clicking and dragging the cursor across the desired region. 3) Initialize subintegral sliders. Since multiple voltages may be present, we have included the ability to piece-wise cover the time period of interest. The user is prompted to enter the bias voltage (V_i) for each slider set that is initialized. 4) Set baseline and adjust integral limits. The baseline current at the appropriate voltage ($I_{(b|V_i)}$) is set by the green slider, while the integration limits are set by the red pair. 5) Repeat steps 3 & 4 as needed. 6) Compute the total conductive flux. The contribution of each subintegral is summed and the total conductance is displayed in units of nS·s.

3.3.4 $A\beta_{1-42}$ & $A\beta_{pE3-42}$ membrane analysis

The data from Chapter 2 was reanalyzed using the total conductance program introduced here. $A\beta_{1-42}$ ($n = 6$) and $A\beta_{pE3-42}$ ($n = 6$) were run through the software and the total time, from first activity event, to reach the toxicity threshold was recorded. Based on the calculations of Arispe et al. [57, 59], which estimate that a giant 4 nS channel would lead to a loss of ionic homeostasis and cell death in a only a few seconds, we have set the toxicity threshold at 15 nS·s. Using this notation a 1 nS channel would reach toxicity after being open for 15 s while a 100 pS channel would require 150 s.

3.4 Results

As proof of principle for our newly designed program, we analyzed the total conductive flux through $A\beta_{1-42}$ and $A\beta_{pE3-42}$ pores and determined the time to the cytotoxicity threshold (15 nS·s). $A\beta_{pE-42}$ membranes reached toxicity after an average of 4.94 ± 5.80 min (Mean $\pm$ SD) as compared to 13.20 ± 17.89 min for $A\beta_{1-42}$ (Table 3.1). The shorter average time to toxicity for $A\beta_{pE-42}$ is indicative of greater cellular toxicity, though the results were not statistically significant. This is in line with previous reports on the toxicity of $A\beta_{pE3-42}$ [41, 152, 42] as well as with the conclusions drawn in Chapter 2. We note that these results are highly variable with the standard deviation exceeding the mean in both cases. This is unsurprising giving the wide range of single channel conductances seen in Figure 2.4. Interestingly, for both peptides, Trial 3 appears to be an outlier with a much longer lifetime before toxicity than any of the other cases. When these trials are excluded, $A\beta_{pE3-42}$ still shows shorter time to threshold (2.62 ± 1.23 min) when compared to $A\beta_{1-42}$ (6.07 ± 4.36 min). While the variability in the measurement is greatly reduced, the results still do not reach statistical significance.

$A\beta_{1-42}$ pores demonstrate more spike and burst behavior (Figure 3.2) than $A\beta_{pE3-42}$ pores (Figure 3.3) which could explain the longer time to threshold. Spikes and bursts, due to their short lifespans, do not contribute as much to the total conductance as steps. This is one of the key advantages of our system as it does not give equal weight to all activity. $A\beta_{1-42}$ membranes that showed spike and burst activity had extended time periods that contributed little to toxicity (Figure 3.2A) followed by more concentrated regions (Figure 3.2B). $A\beta_{pE3-42}$ appeared to preferentially show step activity (Figure 3.3A) with toxicity occurring relatively quickly. While histogram analysis is only able to address defined conductance events, we show that nonspecific membrane leakage, which would contribute significantly to cytotoxicity, is properly incorporated into the summation (Figure 3.3B). Overall, the results validate our analysis system.

3.5 Discussion

We have shown that total conductive flux can be used to effectively determine, and compare, toxicity of different $A\beta$ species in model membrane systems. In the pro-

cess we have verified the function of our new analysis program. This program has several advantages over traditional analysis of amyloid pores. The biggest of these advantages is that it provides a direct quantitative means of comparing a biologically relevant measure of cytotoxicity in a model system. Previous quantitative analysis of amyloid peptides [91, 87] relied on histograms of single channel conductivity in an attempt to draw ensemble level comparisons.

While informative, such histograms are of dubious significance to cellular toxicity as they are unfairly biased toward prevalent, but short-lived, events that may not significantly contribute to disruption of ionic homeostasis. While large spikes and bursts can be of significance to toxicity, they need to occur with some regularity to induce the kinds of ionic flux that lead to cell death. As seen in Figure 3.2, it is not until activity is continuous, or closely spaced, that ionic flux will reach toxic levels. This is especially true considering that cells are not static entities and have mechanisms in place to actively maintain ionic homestasis [153]. As a result intermittent transients, with long refractory periods, caused by spiking amyloid pores are likely to play no role in cell death. The formula used in our analysis does not currently include a clearance term, and while it likely would not make much difference in the case of continuous activity, the addition of one would lead to a more accurate depiction of the cellular environment.

Comparison of the activity suggested that spikes and bursts are more prevalent for $A\beta_{1-42}$ than $A\beta_{pE-42}$. $A\beta_{pE-42}$ showed little spike behavior, with there being a strong preference for steps (Figure 3.3A). Given this activity, it is not surprising that we see $A\beta_{pE-42}$ reach the cytotoxicity threshold more quickly. Our MD simulations in Chapter 2 suggested increased stability of $A\beta_{pE-42}$ pores which would lead to the continuous activity seen with step behavior and could explain its greater in vitro cytotoxicity [91]. In addition to the step behavior, nonspecific leakage—seen as an overall growth of ionic current without any defined conductance event—is demonstrated (Figure 3.3B). While analyzed here and clearly relevant to toxicity, such behavior is ignored by the creation of activity histograms.

The analysis that goes into creating histograms is time consuming and tedious. Creation of the histograms in Figure 2.4 took nearly two weeks of work, as compared to less than a single day to run the analysis on the 12 membranes shown in Table 3.1. While

we gain speed and direct toxicity relevance, we lose data quantity and increase variability. Histograms can give > 1000 data points for relatively few membranes and allow for an ensemble level view of activity. Reducing the combined effect of these pores to a single value (i.e. time to toxicity threshold) gives only a single data point per membrane. From our analysis it is clear that the opening of a large channel would destabilize cellular homeostasis much more quickly than burst behavior of a small one. Given the heterogeneous nature of $A\beta$ pores, this is seemingly random, introducing more variability in our analysis and requiring that more membrane experiments be run to get statistically relevant data. While the data we present here seems to point toward confirmation of $A\beta_{pE-42}$ as more toxic, with it taking less time to reach the toxicity threshold, the results are far from statistically significant—this is true even when excluding the outlier trial of each peptide.

The simplicity and speed of our program allows for the analysis of the quantities of experiments that will be needed to draw meaningful conclusions with regards to toxicity. Unfortunately, bilayer recording itself is an inherently tedious and low throughput technique. Performing experiments with the large numbers of membranes that will be required is extremely difficult and time consuming using current techniques. However, in recent years, new technology has emerged that could facilitate large numbers of bilayer experiments. Two German companies, Nanion and Ionera, have worked together to introduce a high throughput automated bilayer recording system. The Nanion Orbit16 makes used of Ionera's MECA16 chip to enable rapid formation of 16 stable bilayers that are recorded in parallel [154, 155, 156, 157]. While currently cost prohibitive, one could imagine having 100+ membranes to analyze using this system which would allow for statistically meaningful analysis that provides great insight into toxicity mechanisms of $A\beta$ and other amyloid peptides.

3.6 Conclusion

In summary, we have created a new analysis system for the study of $A\beta$ membrane poration that provides more relevant info for toxicity than current tools. By reanalyzing the data from Chapter 2, we have successfully provided a proof of principle

for our software while demonstrating improvement over traditional analysis of channels, which rely on histograms. The system requires more data and membranes which can be accomplished by new technology. While statistically meaningful analysis will require many more bilayer recording experiments, emerging high throughput technologies provide the means to reach this goal. Our analysis platform is able to quickly process this data and will be extremely useful for the study of $A\beta$, and other amyloid, cytotoxicity.

Chapter 3 is original content. The dissertation author was the primary author of the content. Thanks are given to Joe Phaneuf for his assistance in development and implementation of the Python code used for the analysis in this chapter.

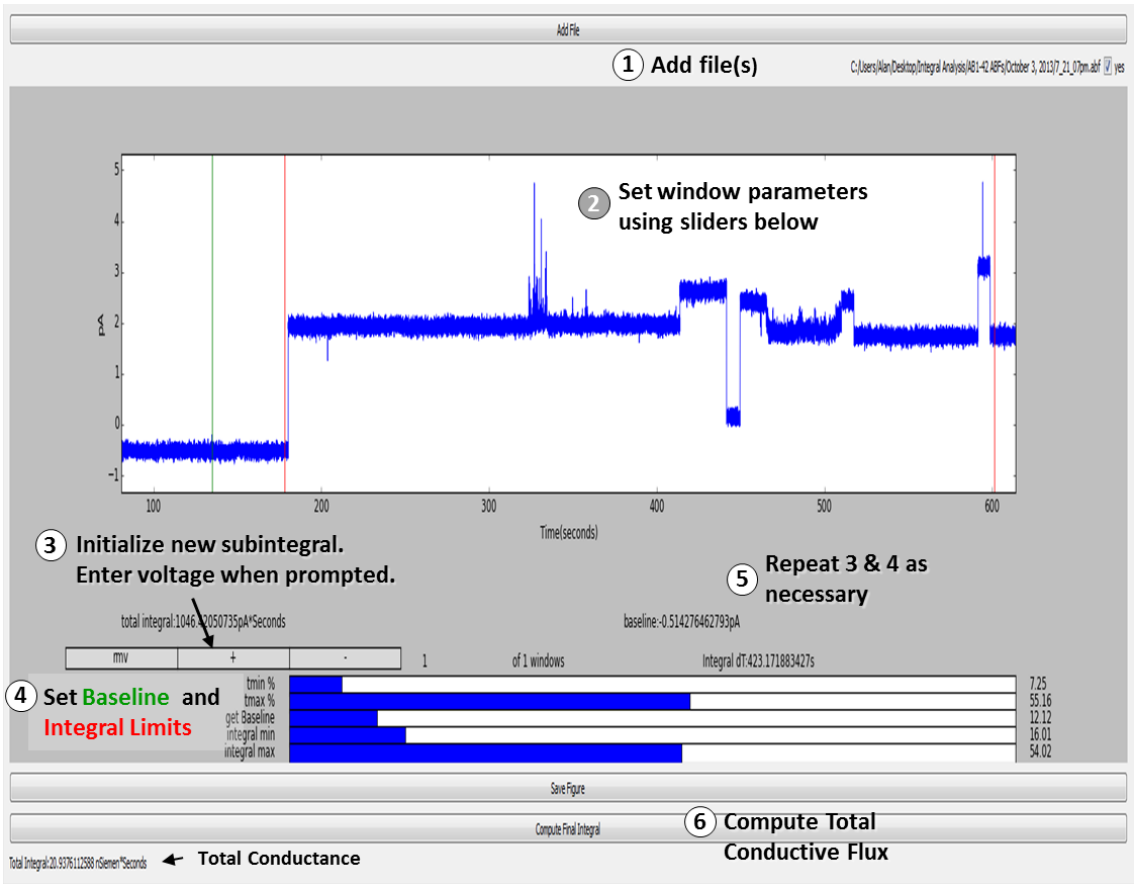

Figure 3.1: **User interface for total flux analysis.** Our program provides the user great flexibility in an easy to navigate interface. The workflow for membrane analysis is highlighted. File(s) are added (1) and the user adjusts the limits of the viewer window (2). Initializing an integral set prompts the user to enter the applied bias voltage (3). Using the slider bars at the bottom, the baseline—at this voltage—and the integral limits are adjusted (4). The user may repeat the previous steps as necessary to cover their region of interest (5). The total conductance is then computed with the click of a button (6) and displayed in the bottom left corner in nS·s.

Table 3.1: **Time to cytotoxicity threshold for Aβ_{1-42} and Aβ_{pE3-42}.** All trials are shown for each peptide. The toxicity threshold was set at 15 nS·s. $A\beta_{pE3-42}$ pores reached toxicity faster and with less variability in the measurement than $A\beta_{1-42}$ pores.

Trial	Time to Threshold (min)	
	$A\beta_{1\text{-}42}$	$A\beta_{pE3\text{-}42}$
1	10.04	2.56
2	11.06	2.74
3	48.85	16.56
4	3.26	4.54
5	0.92	2.08
6	5.06	1.18
Mean	13.20	4.94
SD	17.89	5.80

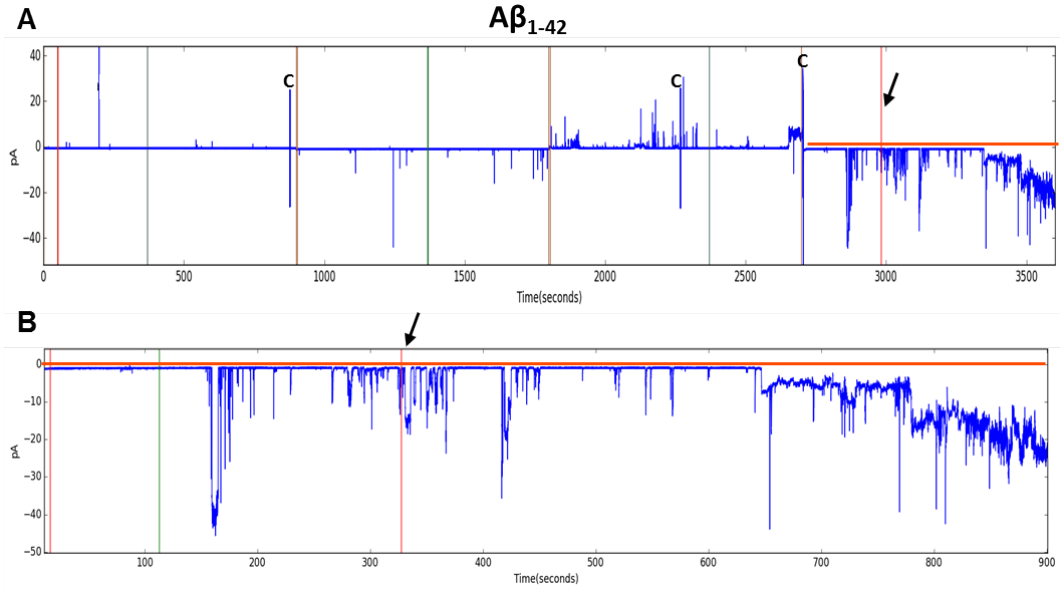

Figure 3.2: **Aβ_{1-42} pores show spike and burst activity.** $A\beta_{1-42}$ activity shows more spike and burst behavior than $A\beta_{pE3-42}$ pores which could contribute to its increased time to the toxicity threshold. The integration limits are seen as vertical red lines while the toxicity threshold is indicated by the arrow. **A)** Full recording of Trial 3 for $A\beta_{1-42}$. While activity us seen throughout the trace, the majority of the early activity is spikey in nature. These spikes do not contribute significantly to destabilization of cellular homeostasis. More concentrated regions with abundant bursts and steps follow. **B)** Enlargement of the time period indicated by the orange line. The toxicity threshold is reached as indicated by the arrow. Activity persists beyond the threshold and is therefore erroneously counted when creating activity histograms.

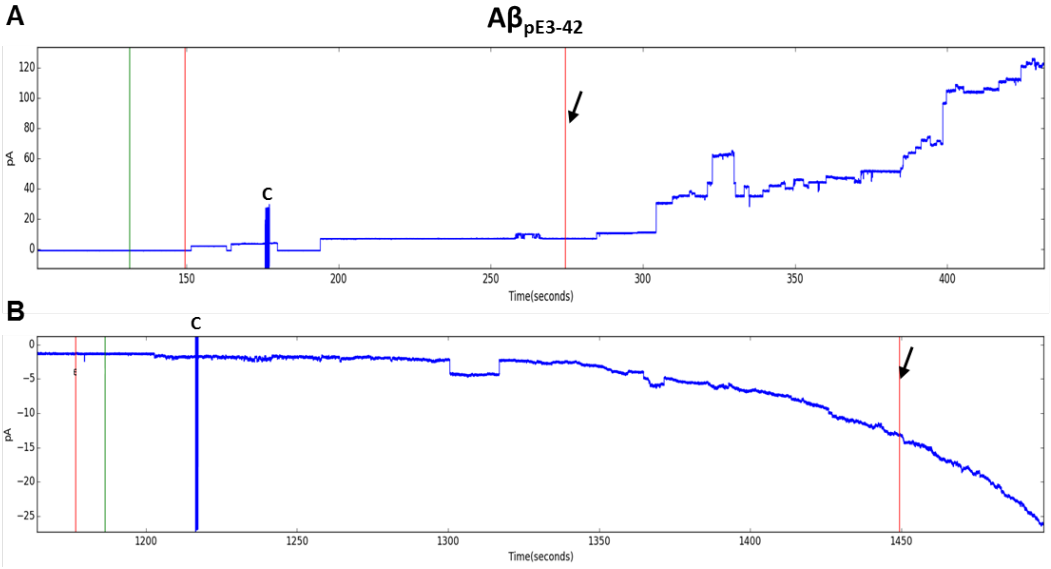

Figure 3.3: **A$\beta_{\mathbf{pE3-42}}$ pores preferentially show step behavior and faster toxicity.** Two separate trials of a $A\beta_{pE3-42}$ are presented showing that toxicity (indicated by the arrow) is rapidly reached. **A)** Step activity is preferred with little to no spike behavior seen. As shown in Figure 3.2, activity extends well beyond the point that toxicity is reached. These extra events are irrelevant to toxicity. **B)** Our analysis takes non-specific leakage into account, something that is missed by histograms of event conductance.

Chapter 4

Membrane embedded anle138b compound modulates $A\beta$ pore activity

4.1 Abstract

According to the amyloid cascade hypothesis, accumulation of amyloid-β ($A\beta$) peptides in the brain is the primary driver of pathogenesis in AD, including synapse loss and neuronal cell death. The channel hypothesis for $A\beta$ oligomers postulates that unregulated $A\beta$ ion channels result in a loss of ionic homeostasis (primarily through a gain of Ca^{2+}) and neuronal death is one of the oldest explanations of the neuronal dysfunction and toxicity. To date, there has not been a pharmaceutical compound that would block pores and be active in mammalian animal models, a necessary element for disease modulation. In this work, we examine biophysical properties and pore activity modulation mechanisms of the diphenylpyrazol (DPP) compound anle138b which was previously optimized for the reduction of prion protein aggregation relevant for Creutzfeld Jakob Disease (CJD) as well as α-Synuclein aggregation relevant in Parkinson's disease (PD). We show modulation of of $A\beta$ induced electrical activity by anle138b in black lipid membranes despite no change in the membrane embedded pore structure, as seen by AFM. This suggests that a conformational change within the core of the pore is responsible for the activity modulation.

4.2 Introduction

$A\beta$ and tau are the two proteins whose aggregation is linked to Alzheimer's disease (AD). The role of the two proteins in causing dysfunction of neurons and their cell death is still unclear. According to the amyloid cascade hypothesis, accumulation of amyloid-β ($A\beta$) peptides in the brain is the primary driver of pathogenesis in AD, including synapse loss and neuronal cell death [110, 111, 112, 35, 18]. In patients, synapses are lost disproportionally to neurons and this correlates best with dementia [158, 159, 160]. Oligomers are considered to be the drivers of dysfunction through spine loss [161] and cell death [75, 120, 41, 146, 162, 163, 164, 165, 28, 166, 135, 167, 168, 48, 23, 25]. Spine loss in brain slices was shown to be reversible by inhibitors of aggregation of $A\beta$ as well as by antibodies reducing the $A\beta$ load. The channel hypothesis for $A\beta$ oligomers, which postulates that unregulated $A\beta$ ion channels result in a loss of ionic homeostasis (primarily through a gain of Ca^{2+}) and neuronal death, as proposed by Arispe et al [59, 61], is one of the oldest explanations of the neuronal dysfunction and toxicity.

In vivo evidence for this mechanism is still missing and other mechanisms such as $A\beta$ oligomer induced NMDA endocytosis [161, 12] and modulation of α-amino-3-hydroxy-5-methyl-4-isoxazole propionic acid surface receptors [12] potentially mediated by prion protein acting as an $A\beta$ oligomer receptor [169] have been proposed. Nevertheless, the channel mechanism was corroborated by the direct observation of pore structures in black lipid membranes [59, 57] and in AFM studies [48] and by correlating blocking of $A\beta$ pores by the small molecules, MRS2481 and MRS2485 [170] and EGCG [170] reduced $A\beta$ toxicity in cell based AD models. EGCG was shown to have similar activity also on α-Synuclein pore formation [117] and rescues α-Synuclein induced neurotoxicity in cell based assays [171]. However, so far there has not been a compound that would block pores and be active in mammalian animal models leaving the request by Arispe and coworkers [59]: "We further propose that a useful strategy for drug discovery for treatment of Alzheimer's disease may include screening compounds for their ability to block or otherwise modify $A\beta$P (i.e. $A\beta$ protein) channels" unsatisfied.

In this work, we examine biophysical properties and pore activity modulation

mechanisms of the diphenylpyrazol (DPP) compound anle138b. Anle138b was previously optimized for the reduction of prion protein aggregation relevant for Creutzfeld Jakob Disease (CJD) as well as α-Synuclein aggregation relevant in Parkinson's disease (PD). It has shown therapeutic efficacy in PD and CJD mouse models [172, 173, 174] and blocked α-Synuclein oligomer induced pores in black lipid membranes (BLMs). Using BLM, we show that these compounds modulate the activity of $A\beta_{1-42}$ pores. With AFM, we observe similar $A\beta_{1-42}$ pore structures in membranes in the presence or absence of anle138b despite the dramatic change in their conductivity. This suggests the functional modulation of the membrane bound oligomers as a mechanism for neuroprotection and rescue of neuronal dysfunction by anle138b.

4.3 Methods

$A\beta 1-42$ was purchased from Bachem and Anaspec (Fremont, CA). The phospholipids 1,2-dioleoyl-*sn*-glycero-3-phosphoserine (DOPS) and 1-palmitoyl-2-oleoyl-*sn*-glycero-3-phosphoethanolamine (POPE) were purchased from Avanti Polar Lipids (Alabaster, AL). All other chemicals were purchased from Sigma-Aldrich (St. Louis, MO).

4.3.1 Peptide Handling

For BLM experiments, $A\beta_{1-42}$ peptides were dissolved in Milli-Q water to a concentration of 1 mg/mL prior to being aliquoted for storage. These 50 μL aliquots were stored at -80° C for a maximum of 60 days before use. Samples were thawed only once. For ThT and AFM experiments, powder form of $A\beta_{1-42}$ (Bachem, Torrance, CA) was first dissolved in 1% ammonium hydroxide until the peptides were completely dissolved. They were subsequently sonicated for approximately 2 min. Small volume of peptides were then aliqouted and lyophilized using a lyophilizer (Labconco FreeZone 2.5 Plus, Kansas City, KS). The aliquots were stored at -80° C until used. For every experiment, aliquoted peptides were thawed and hydrated in 20 mM NaOH and HEPES buffer solutions at pH 7.4, sequentially. The peptide concentration was measured using the 280 nm UV absorbance ($\varepsilon = 1490\ \mathrm{M}^{-1} \cdot cm^{-1}$).

4.3.2 Planar Lipid Bilayer Electrical Recording

We prepared planar lipid bilayers using the so-called "painted" technique [96]. Anle138b was mixed with a 1:1 (w/w) solution of DOPS and POPE in chloroform at a concentration of 10 mM with respect to the volume of the lipids. A lipid specific gravity of 0.8 was used for the calculation. This mixture was subsequently dried in a Rotavapor R-210 (Buchi) and resuspended in decane at a total lipid concentration of 20 mg/mL. Bilayers with embedded Anle138b were formed from this solution. Spontaneous membrane formation occurs following the addition of lipid directly over a pore with a diameter of $\sim$250 μm in a Delrin septum (Warner Instruments, Delrin perfusion cup, volume 1 mL). In previous studies, this membrane composition was shown to be stable for long recording times ($>$ 4 h) [90, 91]. Control experiments establishing the stability of membranes formed with the addition of Anle138b were performed. As the electrolyte, we use 150 mM KCl, 10 mM HEPES (pH 7.4), and 1 mM $MgCl_2$.

Before performing electrical recordings, we verified that the bilayer was stable for several minutes with low conductance ($<$ 10 pS) across $\pm$100 mV applied voltage and that the system capacitance was $>$ 110 pF. When both criteria were met, peptide was added directly to the *cis* (hot wire) side and stirred for 5-10 min. Peptide concentration in the bilayer chamber was approximately 10 μM. Bilayer stability was monitored by periodic capacitance measurements throughout the course of the experiment.

All traces were recorded in voltage clamp mode using the 2 kHz built-in filter cutoff of our BC-535 amplifier (Warner Instruments, Hamden, CT). A sampling frequency of 15 kHz was used for all data acquisition. We used a custom-made LabVIEW program to record the current and Clampfit 10.2 (Molecular Devices, Sunnyvale, CA) to analyze traces. For representation in Figures, we have filtered the recorded current versus time traces with a digital Gaussian low-pass filter with a cutoff frequency of 50 Hz.

4.3.3 Lipid Bilayer Preparation for AFM Imaging

For liposome preparation, DOPS and POPE lipids were used in a 1:1 ratio. Liposomes were prepared by mixing 20 μL of each lipid (5 mg/mL) dissolved in chloroform

and anle138b also dissolved in chloroform was added to have 1000:1 lipid to anle138b molar ratio. Then they were allowed to dry overnight in vacuum. The dried lipid film (and anle138b) was hydrated with peptide solution to facilitate peptide incorporation in the lipid bilayer, resulting in proteoliposome formation. For control, the dried lipid film (and anle138b) was hydrated with 200 μL of HEPES buffer and vortexed occasionally for an hour. The large multilamellar vesicles formed with this procedure were sonicated for 5 min. Supported lipid bilayers were formed by (proteo)liposome rupture and fusion on the mica substrate [48, 45, 82, 83, 175]. Lipid concentrations of $\sim 0.1 - 1$ mg/mL were deposited on freshly cleaved mica and incubated for $\sim$10 min on a hot plate above the lipid transition temperature to facilitate fusion of the ruptured proteoliposomes on the mica surface. As a last step, samples were rinsed with buffer to remove unruptured proteoliposomes still in solution.

4.3.4 AFM Imaging

Topographic images were acquired using a Multimode AFM equipped with a Nanoscope V controller (Bruker, Santa Barbara, CA). Silicon Nitride cantilevers with nominal spring constants of 0.08 N/m (OMCL-TR400, Olympus) were employed for imaging in fluid using tapping mode. Resonance frequencies of $\sim$8 kHz and drive amplitudes under 100 mV were used. All experiments were performed at room temperature. Actual spring constants were measured to be within 10% of its nominal value using thermal tune before the experiments. To measure outer pore diameters, tip broadening was taken into account by modeling the inserted oligomers as a spherical cap protruding a height, h above the surface of the lipid bilayer in contact with a spherical tip of radius, R [84].

4.4 Results

In order to gain further insight in the potential mode of action, we analyzed the effect of anle138b on the pore formation potential of $A\beta$ in lipid membranes, as well as the structural features of these pores seen by AFM.

4.4.1 Effect of compounds on $A\beta_{1-42}$ pore activity

We used BLM electrical recording to examine the activity of $A\beta_{1-42}$ pores in lipid membranes (POPE/DOPS 1:1) treated with 10 mM anle138b (with respect to the lipid volume). $A\beta_{1-42}$ pore activity is indicated by discrete features in the ionic current passing through the lipid membrane (Figure 4.1). Unlike ion channels which have regulated activity and possess integer values of a unitary conductance, amyloid pores are not regulated and present multiple conductance values [48, 23, 59, 57, 90, 91, 85, 22, 65]. For compound-treated membranes, bulk membrane activity was reduced in 50% of trials (3 of 6) to $< 10\%$ of the maximum value measured in membranes without compound (Figure 4.1). In all cases of membranes without compound, the overall current through the membrane kept increasing and eventually reached the saturation value of our electrical current amplifier (Figure 4.1A). The current grows in a stepwise fashion indicative of channel activity, with newly formed or opened channels adding to the bulk activity of the membrane. While half of the anle138b membranes also showed this pattern, we observe clear differences in the activity pattern induced by the compound in the other trials. Necessary elements of the BLM experimental setup can help to account for the activity seen in unsuccessful trials and will be discussed further below. Anle138b membranes showed fewer simultaneously active pores and increased membrane stability (Figure 4.2, B & C).

4.4.2 Effect of compounds on the structure of $A\beta_{1-42}$ pores

The structural properties of $A\beta$ pores inserted in lipid bilayers have been characterized by AFM. Our previous studies using 1,2-dioleoyl-sn-glycero-3-phosphocholine (DOPC) lipid bilayers indicate that full-length $A\beta_{1-40/42}$ [48, 23, 82], certain $A\beta$ mutants [23, 83], $A\beta$ fragments [45, 85, 119, 89], as well as other amyloids [48, 23, 44, 50] form heterogeneous pore structures, typically protrude < 2 nm above the membrane plane, have inner pore diameters of $1-2$ nm, typical outer diameters in the range of $8-12$ nm and possess 3-6 subunits [48, 23, 45, 82, 83]. These pore structures and in particular the subunits are difficult to detect because of additional non-pore forming oligomer populations inserted in the membrane, as well as the experimental difficulties

associated with observing disordered pore structures [84].

Here, we studied the structure of $A\beta_{1-42}$ pores in POPE/DOPS (1:1) membranes treated with anle138b. Untreated membranes phase separate in lateral POPE and DOPS domains (Figure 4.2A), discernible by a difference of $\sim$0.5 nm in bilayer thickness. For membranes reconstituted with $A\beta_{1-42}$, the pore structures have similar doughnut-shaped morphologies (Figure 4.2B), as the pores previously observed in DOPC membranes. We observed similar $A\beta_{1-42}$ pore structures in membranes pre-treated with anle138b (Figure 4.2C). The outer pore diameters in these membranes (Table 4.1) are not significantly different to the pore diameters in membranes without compound, and within the range of pore dimensions observed previously with DOPC membranes [48, 23, 45, 82, 83].

4.5 Discussion

The question of which mechanism on the molecular level induces synaptic dysfunction and neurotoxicity is still under debate. Since synaptic function relies on the integrity of membranes and their ability to modulate ion fluxes in a voltage dependent way, we investigated more closely whether anle138b would modulate the pore forming activity of $A\beta$ that has been proposed to be a mechanism for impaired function and cell death already more than 20 years ago [59, 61]. This mechanism was also found in cell based models for EGCG [170] as well as MRS2481 and MRS2485 [170]. It was also found for anle138b interacting with α-Synuclein and discussed as a potential mechanism in neuroprotection [172, 173].

The pore activity was investigated in well-established black lipid membrane electrophysiological experiment (Figure 4.1). The individual steps in BLM recordings provide true single-channel conductance resolution. The stepwise growth of bulk membrane conductance, in the absence of compound (Figure 4.1A), indicates that the activity increases through the combined action of many individual pores. This "stacking" effect is the result of prolonged pore lifetimes and the formation and/or opening of additional conducting pores. Pores close and/or break apart (notice that there are closing events seen in Figure 4.1A) but, given a long enough period of time, $A\beta_{1-42}$ always leads to a saturating membrane current. In our experiments, this typically occurs no more than 2

h after the first activity is observed.

The significantly reduced pore activity observed in anle138b-doped membranes (Figure 4.1, B & C) suggests activity of fewer $A\beta_{1-42}$ pores compared to the number of active pores in membranes without compound. The individual single channel conductance of the pores does not appear to be significantly altered by the compound. Individual channels demonstrated conductances in the range of $10-700$ pS, similar to the range previously reported for $A\beta_{1-42}$ [90, 91]. Instead, the pore dynamics appear to be affected, resulting in less stable and shorter lived "open" pores, and a reduction in the total number of conducting pores. Since $A\beta_{1-42}$ is characterized by heterogeneous conductance, discreet events of the same conductance suggest the activity of a single pore. Figure 4.1B highlights three distinct conductance levels—additional smaller conductance events are seen by the increased noise midway through the trace. Multiple openings and closings return to these distinct conductance levels, suggesting multiple open-close cycles for the same three individual pores rather than contributions from additional new pores. The short lifespan of the "open" state does not allow for the conductance of multiple channels to add together which keeps the bulk membrane conductance far lower than in the absence of the compound. One membrane did exhibit pore conductance "stacking" but only two individual channels were involved and all other events followed the pattern described here (Figure 4.1C).

While pore activity modulation is only observed in 50% of cases, this is likely the result of the BLM membrane preparation. Anle138b was dissolved in decane along with the lipids prior to membrane painting. Since Anle138b is soluble in both the decane and the lipids, the distribution of compound in the lipid membrane that spontaneously forms upon lipid deposition over the aperture can vary. Lipid monolayers bind to either side of the partition and the bilayer membrane forms as the monolayers fuse together at the center, excluding the decane solvent to the perimeter. This solvent annulus acts as a bridge to the Delrin partition and is essential for membrane stability [97]. If a significant proportion of the Anle138b is mobile in the decane, the compound could be partitioned to the solvent annulus rather than incorporated into the membrane leading to BLM results that appear similar to that seen with $A\beta_{1-42}$ in the absence of compound.

We then compared with AFM the structure of $A\beta$ oligomers in membranes as

well as membranes doped with anle138b. The scale and sensitivity differences between BLM and AFM introduce experimental challenges for imaging different pore states. While membranes with $\sim$100 μm diameter are monitored by BLM, the areas observed by AFM to detect pore structures are $\sim 10^5$ smaller. Therefore pore densities of $\sim 10^{-4}$ pores/μm^2 are detectable by BLM, while densities of $\sim 10 - 100$ pores/μm^2 are optimal for AFM imaging. Our BLM data suggest that only a handful of pores in anle138b treated membranes are active at any given time over this large area. Therefore, the probability of imaging compound treated pores, with AFM, in the "open" state is quite small and pore-like structures found in the membranes are more likely in the closed state. Attempts to increase the pore density for AFM imaging by increasing the peptide:lipid ratio, are complicated by the additional populations of membrane-associated $A\beta$ oligomers also observed [84].

The similar pore structures observed by AFM in untreated and anle138b-treated membranes (Figure 4.2, B & C) with the apparent diameters of around 10 nm listed in Table 4.1 suggest that pores remain seemingly intact at the pore mouths imaged by the AFM tip, and the decrease in pore activity can be attributed to changes that occur in pore regions embedded in the hydrophobic lipid core of the membranes (Figure 4.2C), where the AFM tip does not penetrate during imaging. These changes could stem from the binding of anle138b molecules to intramembranous pore regions consequently producing blockage of the pore, or they could be due to conformational changes of the pore induced by the compound molecules.

Numerous potential modulation mechanisms can be envisioned to explain the observed structural and conductance properties (Figure 4.3). These mechanisms can be broadly broken down into three cases: i) the oligomers are unable to insert into the lipid bilayer (Figure 4.3A); ii) once inserted, oligomers cannot form into pore structures (Figure 4.3B); iii) a structural change is induced that leads to a non-conducting (collapsed) pore (Figure 4.3C). Our data contradicts the first scenario. However, it cannot discern between the latter two mechanisms. Even though a population of pores is still observed in anle138b-doped membranes, decreased pore formation due to anle138b binding to smaller oligomers is possible. Thioflavin T and NMR data obtained with the hydrophilic compound anle138c, differing by only one carbon atom from anle138b (manuscript

in preparation), indicates that $A\beta$ aggregation is inhibited by anle138c binding to $A\beta$ oligomers. A statistically significant comparison of pore populations is complicated by experimental difficulties in observing large numbers of $A\beta$ pores. In the absence of anle138b, $A\beta$ oligomers insert into lipid bilayers and form pores that are long lived. When anle138b is doped into the lipids, oligomers insert into the membrane most probably with a similar efficiency as in the absence of DPP compounds, but the vast majority of pores are inhibited from passing ionic currents across the membrane. The pores that do conduct stay open much shorter and are in rapid exchange with non-conducting pores (Figure 4.3C).

Our current data suggests it is likely that anle138b induces a conformational change within $A\beta$ pores that greatly reduces or, in most pores eliminates, toxic ionic flux. Steric blockage by anle138b without conformational change of the pore is energetically unfavorable due to the hydrophobicity of anle138b, as this scenario would require anle138b to be in contact with water molecules inside the pore. The above mentioned mechanisms provide further insight into the method of action in preventing pore activity and reducing Alzheimer's pathogenicity.

4.6 Conclusion

Biophysical characterization of the effect anle138b shows the ability of the compound to significantly modify the activity of $A\beta$ oligomer induced pores in black lipid membranes while largely unaffecting the pore morphology. Careful analysis of this activity indicates that the oligomers are still in the membrane but have a changed conductivity profile, mainly staying open for shorter time and lacking the possibility of building up large currents as seen in the absence of the compounds. While this mechanism is established only in vitro on $A\beta$ it has been found already previously on hydrophilic compounds [170] and on anle138b acting on α-Synuclein [172, 173]. In the future, this mechanism is worth being investigated further in-vivo in cell based models.

Chapter 4 in whole contains material currently being prepared for publication. Thanks are given to the co-authors of the manuscript: Hernandez Martinez, A., Lee, J.,

Ryazanov, S., Agbemenyah, H.Y., Li, Q., Leonov, A., Benz, R., Giese, A., Arce, FT., Korte, M., Lal, R., Griesinger, C., Eichele, G., and Fischer, A. The dissertation author was the primary author of the material contained within the chapter.

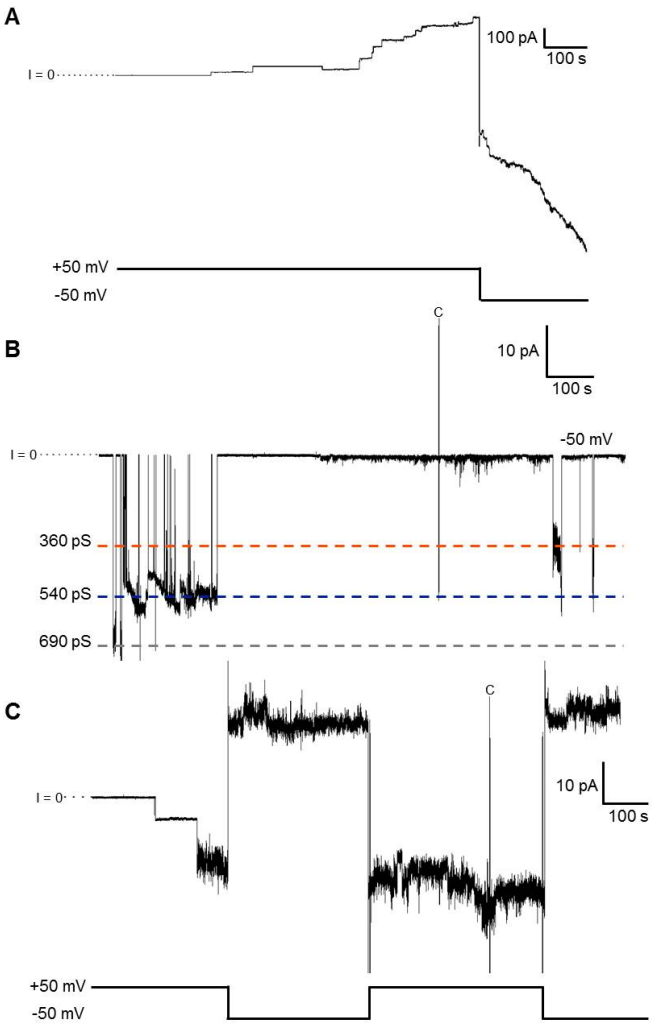

Figure 4.1: **Anle138b modulates channel activity of Aβ_{1-42} in BLMs.** BLM recordings of $A\beta_{1-42}$ in the **A)** absence and **B)** presence of anle138b in DOPS/POPE. **A)** $A\beta_{1-42}$ induces pore-like step ionic current increases across lipid bilayer membranes. The stepwise growth of bulk membrane conductance indicates that the activity increases through the combined action of many individual pores. This "stacking" effect is the result of prolonged pore lifetimes and the formation and/or opening of additional conducting pores. Given a long enough period of time, $A\beta_{1-42}$ always leads to a saturating membrane current. **B)** The presence of anle138b in the membrane modulates activity and prevents the concurrent activity of many channels that leads to membrane saturation. Discreet conductance levels are highlighted showing multiple opening and closing events for three individual pores. **C)** Pore "stacking" was observed in one Anle138b treated membrane that demonstrated activity modulation, but current saturation was inhibited. This is likely due to the large area of BLM membranes which could allow individual pores to form in isolated membrane regions where they do not encounter the compound.

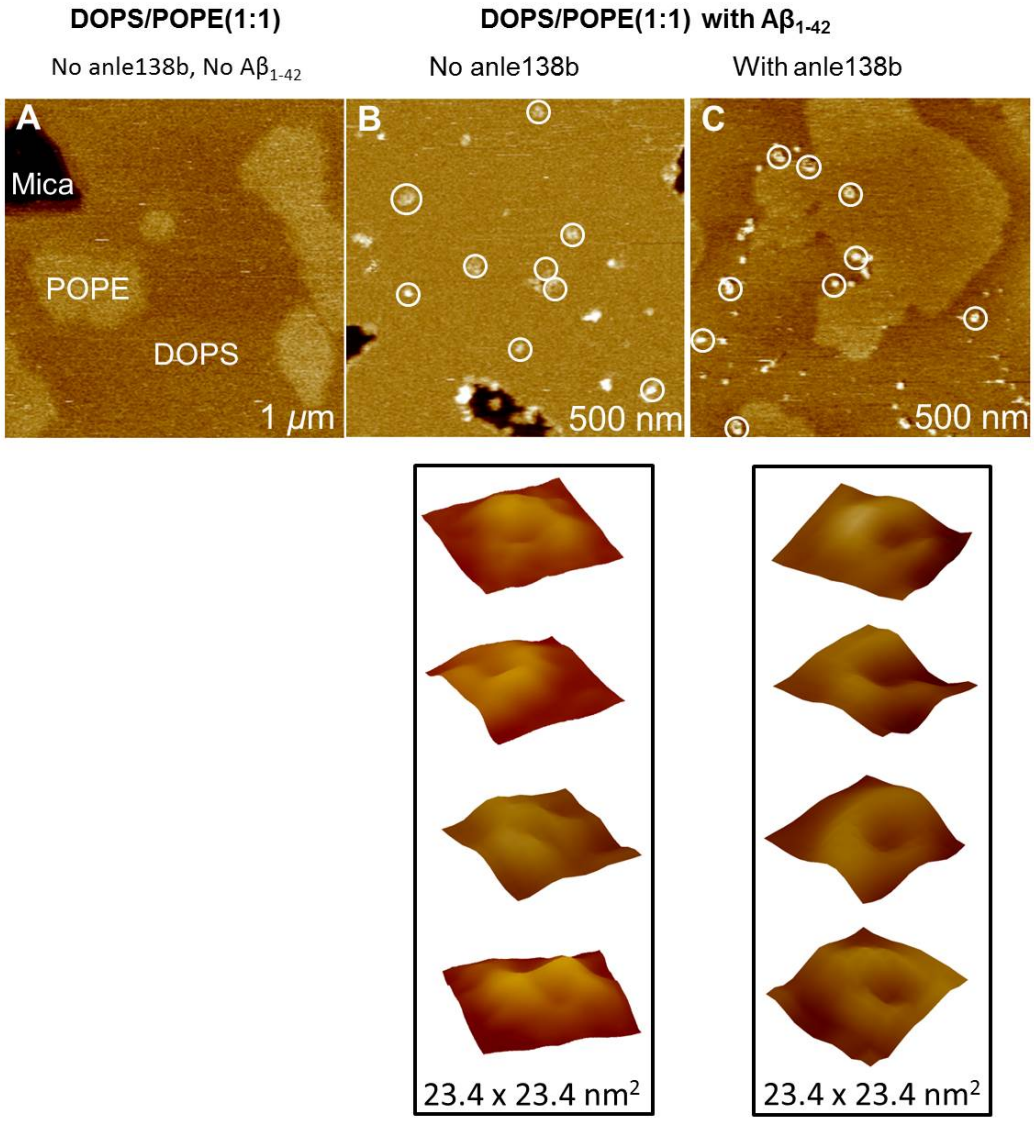

Figure 4.2: **Observation of Aβ_{1-42} pores by AFM in anle138b-doped membranes.** AFM tapping mode images showing similar pore structures in membranes with and without anle138b. **A)** POPE/DOPS (1:1) membranes without compound and not exposed to $A\beta_{1-42}$ showing lateral phase separation. **B)** Membrane with the same lipid composition as in A) without compound reconstituted with $A\beta_{1-42}$ at a 1:60 peptide/lipid molar ratio. **C)** Membrane with the same lipid composition as above with anle138b (10 mM with respect to lipid volume) and reconstituted with $A\beta_{1-42}$ (1:60 peptide/lipid molar ratio).

Table 4.1: **Effect of anle138b on pore size.**
The pore size is not changed. ***Expand on this very briefly***

No. of pores	Measured diameter (nm)	Corrected diameter (nm)
	Without anle138b	
n = 18	13.2 ± 2.7	7.9 ± 2.3
	With anle138b	
n = 15	13.8 ± 3.7	8.1 ± 3.3

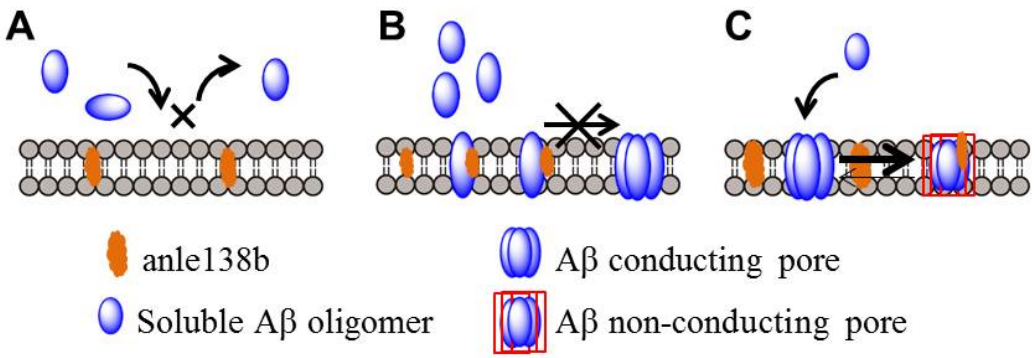

Figure 4.3: **Schematic of potential anle138b mediated pore modulation mechanisms.** We propose that the observed changes induced by anle138b could be explained by any of the following pore modulation mechanisms. At this time we are unable to further distinguish the precise mechanism. **A)** $A\beta$ oligomers are prevented from inserting into the lipid bilayer. **B)** Once inserted, oligomers are unable to aggregate into pore structures by bound anle138b molecules. **C)** Anle138b binds to $A\beta$ pores formed in the membrane leading to a structural change of the monomers and a non-conducting (collapsed) pore.

Chapter 5

Reduction in β-sheet character prevents neurotoxic ionic flux through $A\beta_{1-42}$ pores

5.1 Abstract

A common mechanism underlying Alzheimer's disease (AD) pathophysiology relies upon increased levels of soluble amyloid-beta ($A\beta$) oligomers. These oligomers induce uncontrolled, neurotoxic, ion flux across cellular membranes resulting in the dysregulation of ionic homeostasis, particularly calcium ions. High calcium is known to cause neuronal degeneration and death that might underlie AD cognitive impairment. Previous 3D structural analysis, using atomic force microscopy (AFM), in our laboratory has shown that $A\beta$ forms multi-subunit pores. These pore structures are complemented by the expected ionic permeability and conductance in isolated single channel studies. Since amyloid pore structure-activity relationships are tightly interlinked, pharmacological and small molecule interventions that modulate channel activity could be then become an effective strategy to prevent or ameliorate their toxic activity. In this study, we examined the effectiveness of a small molecule pharmacologic agent in preventing increases in intracellular calcium and reducing ionic flux through $A\beta$ pores. Co-incubation of the compound with $A\beta_{1-42}$ effectively prevented influx of intracellu-

lar calcium in B103 rat neuronal cells while short pre-incubation ($\sim 10-15$ min) prior to bilayer introduction was needed to prevent ionic conductance. Thioflavin-T and circular dichroism indicate a reduction in β-sheet character during the incubation period. We suggest that β-sheet secondary structure is the key structural element of $A\beta_{1-42}$ permeability of cellular membranes and should be a target for future drug development.

5.2 Introduction

Alzheimer's disease (AD) is one of the most devastating diseases associated with aging. It is diagnosed clinically by progressive severe cognitive deficit and substantiated postmortem by the presence of amyloid-β ($A\beta$) plaques in the brains of patients. Brains of AD patients contain extracellular plaques and intracellular neurofibrillary tangles, as well as fewer synapses and neurons [176]. According to the amyloid cascade hypothesis, accumulation of $A\beta$ peptides in the brain is the primary driver of pathogenesis in AD, including synapse loss and neuronal cell death [110, 111, 112, 35, 18]. The plaques are composed of $A\beta$ peptides aggregated into oligomeric and fibrillar species. The full-length $A\beta_{1-40/42}$ peptide is formed via APP cleavage by the action of β- and γ-secretases [111, 36]. A smaller fragment, $A\beta_{17-42}$ (p3), is originated by APP cleavage with α- and γ-secretases [36, 45]. Although amyloid fibrils were believed to be the cytotoxic species in AD [21], increasing evidence indicates that intermediate $A\beta$ oligomers are the most toxic species [75, 120, 41, 146, 162, 163, 164, 165, 28, 166, 177, 135, 167, 168, 48, 23, 25]. A growing number of results suggest that Aβ oligomers inserted in the cell membrane form pore structures [25, 59, 57, 116, 94, 86, 22, 117, 118, 81]. Pore activity has been observed for full length $A\beta$s [48, 23, 59, 57, 82, 87], $A\beta$ fragments [45, 65, 119, 85, 46, 89, 91, 84], and point substitutions [45, 83, 82]. Cytotoxicity results from an abrupt change in cell ionic concentration, in particular the increase in intracellular calcium levels, producing loss of cell homeostasis [66, 67, 68].

Although there have been several approaches for therapeutic intervention, there is currently no cure for AD [118, 178, 179]. These approaches included the clearing of $A\beta$ plaques [118, 180], but plaque removal did not prevent progressive neurodegeneration [118, 181]. Numerous other approaches focused on the processing of the amyloid

precursor protein (APP) by secretase enzymes [118, 178, 179, 180]. The p3 fragment is generally believed to be non-pathogenic, thus reducing the concentration of toxic $A\beta$s by increasing α-secretase activity in the brain (i.e. producing more p3) emerged as a potential therapeutics strategy [182]. A widely used approach has been the use of β-secretase [β-site APP-cleaving enzyme 1 (BACE1)] inhibitors to reduce $A\beta_{1-40/42}$ production [118, 178, 179]. Other approaches included the reduction of $A\beta_{1-40/42}$ production by inhibition of γ-secretase activity [118, 183, 184], and active immunotherapy [178, 180].

Here we discuss the biophysical properties and pore activity modulation mechanism of an aqueous soluble small-molecule compound. The compound, NPT-440-1, was designed as an aggregation blocker of $A\beta_{1-42}$ to prevent the formation of toxic pore structures (Figure 5.1). We show that the compound impedes $A\beta_{1-42}$ aggregation, normalizes intracellular calcium levels, and inhibits the electrical activity of $A\beta_{1-42}$ pores. We suggest that a likely mechanism of action involves a compound induced conformational change leading to disruption of the β-barrel structure for membrane-embedded pore sections leading to nonconducting, and likely, collapsed pores.

5.3 Methods

$A\beta_{1-42}$ was purchased from Bachem and Anaspec (Fremont, CA). The phospholipids 1,2-dioleoyl-sn-glycero-3-phosphoserine (DOPS) and 1-palmitoyl-2-oleoyl-sn-glycero-3-phosphoethanolamine (POPE) were purchased from Avanti Polar Lipids (Alabaster, AL). The water soluble compound NPT-440-1 was graciously provided by Neuropore Therapies, Inc. (San Diego, CA). All other chemicals were purchased from Sigma-Aldrich (St. Louis, MO).

5.3.1 Peptide Handling

For PLB and ThT experiments, lyophilized $A\beta_{1-42}$ powder was dissolved in Milli-Q water to a concentration of 1 mg/mL (221.5 μM) prior to being aliquoted for storage. These 50 μL aliquots were stored at -80 °C for a maximum of 60 days before use. Lyophilized NPT-440-1 powder was dissolved in DMSO to a final concentration

of 10 mM, aliquoted and stored long-term at -20 °C. Compound stock solution was then further diluted to 0.5 mM (for 10:1 peptide:compound condition) or 5 mM (1:1 condition) in DMSO and stored at 4 °C for a maximum of 3 days before use. Samples were thawed only once.

5.3.2 SDS-PAGE

$A\beta_{1-42}$ (American Peptide Company, Sunnyvale CA) was aggregated by incubating the peptides with different concentrations of NPT-440-1 at 37 °C for 16 hr, followed by 6 hr incubation at 56 °C. Western blot analysis was performed as previously described by Masliah et al, 2000 [185] on a 4-12% SDS-polyacrylamide gel (Life Technologies, Carlsbad CA) and blotted onto a PVDF membrane. Blots were labeled with a mouse monoclonal antibody against $A\beta_{1-42}$ (1:1000) (Covance, Princeton NJ), followed by anti-mouse secondary antibodies (1:5000) (American Qualex, San Clemente CA).

5.3.3 Calcium Assay

B103 rat neuronal cells were co-incubated with 1 μM of oligomerized $A\beta_{1-42}$ and different concentrations of NPT-440-1 for 16 hrs, followed by Fluo-4 MW Calcium imaging studies (Life Technologies, Carlsbad CA).

5.3.4 Planar Lipid Bilayer Recording

As before, we prepared planar lipid bilayers using the "painted" technique [96]. 1:1 (w/w) solution of DOPS and POPE in chloroform was dried in a Rotavapor R-210 (Buchi) and resuspended in heptane to a total lipid concentration of 20 mg/mL. Bilayers were spontaneously formed from this solution by direct lipid apposition over a $\sim$ 250 μm diameter aperture in a Delrin septum (Warner Instruments, Delrin perfusion cup, volume 1 mL). In previous studies, this membrane composition was shown to be stable for long recording times (4+ hrs) [91, 90]. As the electrolyte, we use 150 mM KCl, 10 mM HEPES (pH 7.4), and 1 mM $MgCl_2$. Control experiments establishing the stability of membranes formed with the addition of NPT-440-1 were performed.

Before performing electrical recordings, we verified that the bilayer was stable for several minutes with low conductance (< 10 pS) across ± 100 mV applied voltage and that the system capacitance was > 110 pF. When both criteria were met, peptide was added directly to the cis (hot wire) side and stirred for 5 min. For the compound added trials, NPT-440-1 was added directly to the peptide aliquot at the desired molar ratio. The peptide/compound mixture was then either added immediately to the chamber or allowed to preincubate for $10 - 15$ min prior to addition. Peptide concentration in the bilayer chamber was 10 μM and DMSO content was $\sim 0.2\%$. Bilayer stability was monitored by periodic capacitance measurements throughout the course of the experiment.

All traces were recorded in voltage clamp mode using the 2 kHz built-in filter cutoff of our BC-535 amplifier (Warner Instruments, Hamden, CT). A sampling frequency of 15 kHz was used for all data acquisition. We used a custom-made LabVIEW program to record the current and Clampfit 10.2 (Molecular Devices, Sunnyvale, CA) to analyze traces. For representation in figures, we have filtered the recorded current versus time traces with a digital Gaussian low-pass filter with a cutoff frequency of 50 Hz.

5.3.5 Thioflavin-T (ThT) Fluorescence

Stock solution of 500 μM ThT in water was prepared and 2 μL were added to 100 μL HEPES (pH 7.4) buffer in 96-well white-walled plates (Nuncatom, Denmark) to make 10 μM ThT solutions. For peptides, 221.5 μ M stock aliquots were mixed to equilibrate peptide populations amongst the test conditions and then diluted to a concentration of 10 μM with 150 mM KCl, 10 mM HEPES (pH 7.4), 1 mM $MgCl_2$ buffer in the plate well. NPT440-1 dissolved in DMSO was added at desired final concentration before adding the peptide solution. Thioflavin T (ThT) fluorescence (450 nm excitation, 490 nm emission) was monitored every 5 min at 25 $^\circ$C for the indicated times using a SPECTRAmax Gemini EM fluorescent plate reader (Molecular Devices, Sunnyvale, CA). Samples were run in quadruplicate and initial fluorescence intensity was normalized to zero.

5.3.6 Circular Dichroism (CD) Spectroscopy

An Aviv410 CD spectrometer (Aviv Biomedical, Lakewood, NJ) was used to measure the differential absorbance of left- and right-handed circularly polarized light. Aliquots of 221.5 μM $A\beta_{1-42}$ were diluted in water to a final peptide concentration of 44.02 μM (0.199 mg/mL). NPT-440-1 powder was solubilized in DMSO prior to addition to $A\beta_{1-42}$ at the desired molar ratio and subsequent dilution in water. To reduce the effect of DMSO on the CD spectra, DMSO content was lowered as much as possible to $\sim 0.12\%$ of the cuvette volume. Samples were allowed to sit for $10-15$ min prior to loading the cuvette. The spectra was recorded as the average of 9 scans over a wavelength range of $260-180$ nm with 1 nm resolution and an averaging time of 0.5 sec. A 1 mm path length cuvette was used for all measurements. Background signal, using water (for $A\beta_{1-42}$ alone) or water + DMSO (for $A\beta_{1-42}$ + compound), was subtracted from the measurement and the observed signal, S in millidegrees, converted to the mean residue extinction coefficient ($\Delta\varepsilon_{MRW}$) by the following equation [186, 187]:

$$\Delta\varepsilon_{MRW} = \frac{S \times MRW}{32980 \times C_{mg/ml} \times L} M^{-1}cm^{-1} \tag{5.1}$$

where L is path length (in cm), $C_{mg/ml}$ is the peptide concentration in mg/ml, and MRW is the mean residue weight (107.5 for $A\beta_{1-42}$).

5.4 Results

5.4.1 Inhibition of $A\beta_{1-42}$ Aggregation in solution

We first looked at the effect of NPT-440-1 on the aggregation of $A\beta_{1-42}$ in solution. Our SDS-PAGE data (Fig. 5.2) shows that NPT-440-1 effectively reduces the formation of aggregates even at compound concentrations ten times smaller than the peptide content. Co-incubation of NPT-440-1 with $A\beta$ reduced the formation of dimers, trimers, tetramers and higher order oligomers. There is a concentration-dependent inhibition of overall oligomer formation, though this effect plateaus for the 2, 5, and 7 μM cases (Figure 5.2, bar graph).

5.4.2 Recovery of intracellular Ca^{2+} levels

The effectiveness of NPT-440-1 in maintaining normal intracellular Ca^{2+} levels in B103 rat neuronal cells during incubation with $A\beta_{1-42}$ was investigated (Figure 5.3). The presence of $A\beta_{1-42}$ induced a significant increase ($p < 0.01$) in intracellular Ca^{2+} (Figure 5.3B). Addition of NPT-440-1 (1:1 molar ratio) during incubation prevented this increase and Ca^{2+} levels remained comparable to the vehicle control (Figure 5.3C). This suggests that the presence of NPT-440-1 prevented the cellular membrane disruption that leads to $A\beta_{1-42}$ oligomer induced increases in intracellular calcium.

5.4.3 Inhibion of pore activity

The electrical activity of $A\beta_{1-42}$ pores in lipid membranes (POPE/DOPS 1:1) treated with NPT-440-1 was investigated via PLB recording. $A\beta_{1-42}$ pore activity is indicated by discrete features in the tracing of ionic current passing through the lipid membrane (Figure 5.4A). Amyloid pores, unlike ion channels, are not regulated and do not exhibit integer values of a characteristic unitary conductance. Instead amyloid pores present with multilevel conductance values [45, 23, 57, 22, 65, 85, 91, 80]. The current grows in a stepwise fashion indicative of channel activity, with newly formed or opened channels adding to the bulk activity of the membrane (Figure 5.4A). In all trials with the sole addition of $A\beta_{1-42}$ the overall current through the membrane kept increasing and eventually reached the saturation value of our current amplifier. The effect of NPT-440-1 treatment was first examined at a 10:1 peptide:compound ratio. As shown above, this ratio showed effects on $A\beta_{1-42}$ aggregation and intracellular calcium. Simultaneous direct addition of the compound to the test chamber showed no effect on the observed activity with multilevel conductance events clearly present (Figure 5.4B) eventually leading to amplifier saturation. This pattern held true even when the compound concentration was increased tenfold to a 1:1 ratio (Figure 5.4C). However, when NPT-440-1 was allowed to incubate with $A\beta_{1-42}$ for $10-15$ min–at 10:1 peptide:combound–prior to introduction to the test chamber, all activity was prevented (Figure 5.4D). In 100% of trials ($n = 6$) this held true, with no deviation from baseline detected in at least 4 hr of recording.

5.4.4 Reduction in β-sheet character

As $A\beta_{1-42}$ fibrils are known to demonstrate β-sheet secondary structure, we next studied the effect of NPT-440-1 on peptide secondary structure. As with the gel data, our ThT fluorescence results indicate a concentration-dependent inhibitory effect of NPT-440-1 on $A\beta_{1-42}$ aggregation (Figure 5.5A). At both 10:1 and 1:1 peptide:compound ratios the maximum ThT signal was significantly reduced ($p < 0.001$) by 43% and 63% respectively. This pattern is seen even within the first 15 min of monitoring (Figure 5.5A, inset), with significant reduction in ThT fluorescence intensity at both 10:1 ($p < 0.05$) and 1:1 ($p < 0.001$). The CD spectra of $A\beta_{1-42}$ showed β-sheet secondary structure with a characteristic positive peak at 195 nm and a negative peak at 218 nm (Figure 5.5B). The 10:1 NPT-440-1 treated $A\beta_{1-42}$ did not have as clean of a spectrum, due to the presence of DMSO [187], particularly in the far UV region below 200nm. As a result, it is difficult to make conclusions about these wavelengths. However, a small, but clear, upward shift is observed in the 218 nm peak indicating a reduction in β-character. This result agrees very well with the reduction in ThT staining under this treatment condition after 15 min of incubation.

5.5 Discussion

We have observed that incubation of NPT-440-1 with $A\beta_{1-42}$ can effectively normalize oligomer induced increases in intracellular levels (Figure 5.3) and eliminate $A\beta_{1-42}$ pore activity in POPE:DOPS (1:1) membranes (Figure 5.4D). A detailed explanation of pore modulation is difficult to determine because of the numerous potential modulation mechanisms, compounded by missing knowledge about aspects of pore formation, structure and conduction mechanisms. For the small molecular compound used in this study, the potential activity modulation mechanisms include: a) prevention of $A\beta$ binding and membrane insertion, b) prevention of $A\beta$ pore assembly inside the membrane, or c) inducing a nonconducting or collapsed pore. These modulation events are not necessarily mutually exclusive and a combination of multiple effects if certainly possible. All of these potential events could be explained by an induced conformational change in $A\beta_{1-42}$ oligomer structure.

Our SDS-PAGE data (Figure 5.2) indicate that NPT-440-1 inhibits aggregation of $A\beta_{1-42}$ monomers and small oligomers into intermediate oligomers, which are now thought to be the toxic species. These oligomers induce membrane deficits, or pores, which have been shown to lead to increases in intracellular calcium levels. Prevention of intermediate oligomer formation should lessen, or prevent, the influx of calcium. We find that incubation of oligomerized $A\beta_{1-42}$ protein with B103 rat neuronal cells leads to a significant increase ($p < 0.01$) in intracellular calcium (Figure 5.3B) when compared to vehicle (Figure 5.3A). This effect is prevented by 1:1 co-incubation of NPT-440-1 and $A\beta_{1-42}$ with intracellular calcium levels being significantly reduced ($p < 0.001$) when compared to the non-compound treated case (Figure 5.3C). Treatment with NPT-440-1 normalizes the amyloid induced membrane disturbances and leads to observed intracellular calcium levels comparable to vehicle control.

Given the success of NPT-440-1 in normalizing cellular calcium levels, we decided to look specifically at the ability of the compound to prevent pore formation in lipid bilayers. Using PLB electrophysiological recordings we monitored the ionic current crossing a model membrane system. PLB provides true single channel resolution of conduction through the membrane. As expected, $A\beta_{1-42}$ demonstrated multilevel conductance events when exposed to the DOPS:POPE (1:1 w/w) bilayer (Figure 5.4A). Fluctuations in the recorded current represent ionic conductance across the membrane with clear step events indicative of a channel opening/closing (a movement away from baseline is an opening). As seen in Figure 5.4A, these channels can be open simultaneously and the individual channel conductances stack together to grow the bulk ionic conductance across the membrane. Given sufficient time, $A\beta_{1-42}$ activity leads to the saturation of the current amplifier. An effective inhibitor of channel behavior would prevent this activity from occurring.

Simultaneous addition of $A\beta_{1-42}$ and NPT-440-1 to the test chamber showed no tangible effect on ionic conductance when compared to the peptide alone for both 10:1 (Figure 5.4B) and 1:1 (Figure 5.4C) peptide: compound ratios. In both cases the activity demonstrated multilevel conductance steps with periods of spike and burst activities that are also commonly seen in amyloid recordings. As with the untreated case, the activity led to saturation of the current amplifier. However, when the compound was allowed

to pre-incubate with $A\beta_{1-42}$ prior to being added to the test chamber, all activity was prevented (Figure 5.4D). This effect was seen reliably in all cases with preincubation ($n = 6$) at a 10:1 peptide:compound ratio.

The results without incubation are clearly not the result of insufficient concentration, since activity was still seen with ten times more compound than was effective in the incubated case (Figures 5.4B and 5.4C). From this result it is clear that some change in the peptide must occur during this incubation period, prior to the introduction of peptide to bilayer membrane. $A\beta_{1-42}$ pores are composed of various numbers of mobile subunits of small oligomers that must find assemble within the membrane [85]. The variable nature of these pores leads to the heterogenous conductance levels that are seen in PLB recordings of all amyloid proteins tested so far [23]. The need for pre-incubation, even at high compound concentrations, suggest that in direct addition at least a minority population of these subunits insert quickly when exposed to the lipid bilayer in PLB, where they are shielded from the effect of the compound and are free to assemble into conducting pores. Preincubation appears to allow time for a conformational change to be induced prior to exposure to the membrane. Conformational change could prevent membrane insertion, channel formation, or induce a collapsed pore, all of which would lead to no activity being seen in our recordings. To test among these possibilities, structural studies with high resolution AFM would be a natural progression for the expertise of our lab [48, 23, 47, 82, 84].

Numerous MD simulations of $A\beta$ pores have pointed to a β-barrel structure for the intramembrane region of the pore [85, 89, 84, 82, 90]. We have previously shown that $A\beta_{1-42}$ containing a point substituted proline (F19P) showed pore structure by AFM but did not demonstrate ionic conductance [45, 83, 90]. The chemical structure of proline introduces a "kink" in the peptide's secondary structure, which is known to disrupt β-sheet formation. MD simulations of F19P $A\beta$ barrel structure showed that β-sheet destabilization led the highly charged N-terminal regions to bind at the peptide mouth and collapsed the pore [45, 83]. Our current data suggests it is likely that NPT-440-1 induces a conformational change within $A\beta$ subunits that greatly eliminates toxic ionic flux.

Based on the previous studies, we decided to look at whether NPT-440-1 had

any effect on the β-sheet character of $A\beta_{1-42}$. We first monitored fibril formation via ThT fluorescence. As with the gel data, our ThT fluorescence results indicate a concentration-dependent inhibitory effect of NPT-440-1 on $A\beta_{1-42}$ aggregation (Figure 5.5A). It is interesting to note that while aggregation was monitored via ThT fluorescence over the course of 42 hr, a clear and significant ($p < 0.05$) effect of treatment with the compound was observed within the first 15 min at the same 10:1 ratio that prevented ionic conductance in PLB. As ThT primarily detects β-sheet structures [188], these results suggest that NPT-440-1 may inhibit $A\beta_{1-42}$ aggregation into β-sheet containing pore structures acting in the membrane.

This theory is bolstered when analyzing the CD data (Figure 5.5B). The far UV portion of the compound treated spectra is clouded by the known incompatibility of DMSO with CD at these wavelengths [187]. While the DMSO content was lowered as much as possible, increased noise and perturbations are seen below 200 nm. DMSO is a widely used solvent for small molecule drug screening [189]. Though not ideal for use in CD spectroscopy, the DMSO content does not fully skew our results. A clearly noticeable upward shift is seen in the spectra at 218 nm, after 15 min of incubation, for the compound treated peptide when compared to compound free case. The upward shift of this peak is indicative of a reduction in β-sheet content [186]. When combined with our ThT experiments, these results are highly suggestive of disruption of the β-sheet secondary structure found in $A\beta_{1-42}$. Taken together, the studies suggest that β-sheet structure is necessary for toxic conductance through $A\beta$ channels.

5.6 Conclusion

We demonstrate that NPT-440-1 reduces aggregation of $A\beta_{1-42}$ into the intermediate oligomers that are implicated in cytotoxicity. Treatment of B103 rat neuronal shows that addition of the compound prevents the increases in intracellular calcium levels induced by peptide addition to culture. This result implies that the inhibition of oligomer formation prevented the membrane poration that led to calcium influx. Our PLB recordings show that preincubation of the compound with $A\beta_{1-42}$ effectively eliminates ionic flux across the membrane while introduction to the bilayer prior to incuba-

tion shows no effect. Investigation of the peptide secondary structure strongly suggests that NPT-440-1 reduces the β-sheet character of $A\beta_{1-42}$. We propose that NPT-440-1 and other pharmacologic agents that target the β-sheet nature of amyloid proteins could prove effective in slowing or preventing the progression of AD and other amyloid mediated neurodegenerative diseases and should be investigated further.

Chapter 5 in part contains material currently being prepared for publication. Thanks are given to the co-authors of the manuscript: Lee, J., Ramachandran, S., Capone, Masliah, E., and Lal, R. Thanks are also given to Neuropore Therapies Inc. for generously providing NPT-440-1. The dissertation author was the primary author of the material contained within.

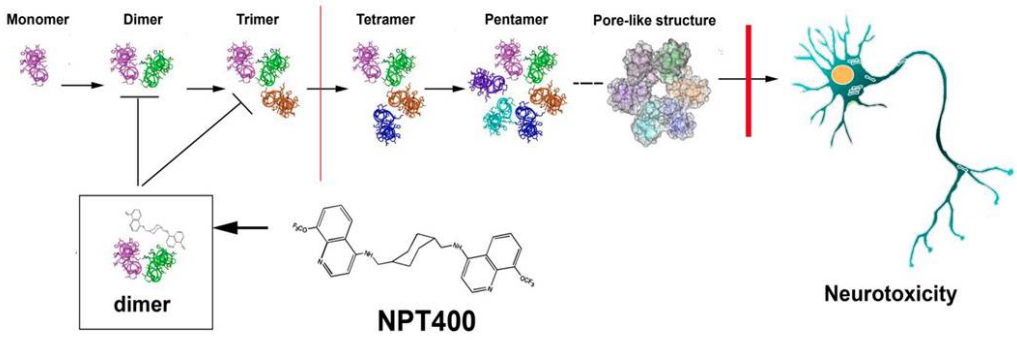

Figure 5.1: **Method of action for NPT-440-1.** NPT-440-1 was designed as an aggregation inhibitor of $A\beta_{1-42}$ into intermediate oligomers capable of forming unregulated cation permeable pores, which are toxic to cells.

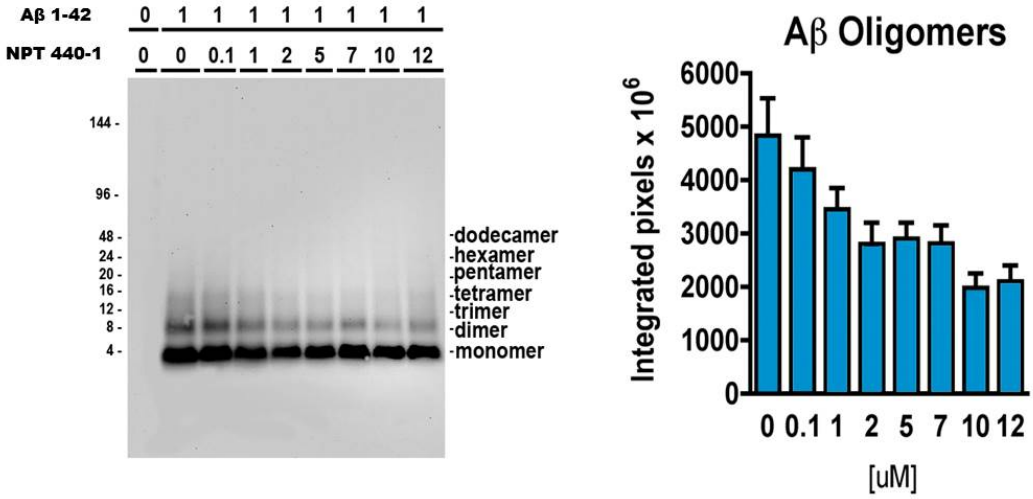

Figure 5.2: **SDS-PAGE immunoblot analysis of Aβ_{1-42} aggregation.** 1 μM $A\beta_{1-42}$ was allowed to aggregate during incubation with NPT-440-1 at different concentrations ($0.1 - 12$ μM) in a cell free in vitro system. NPT-440-1 reduced the formation of $A\beta$ dimers, trimers, tetramers and higher order oligomers.Aggregation reduction is dose dependent, but a response is seen even at a 10:1 peptide:compound ratio.

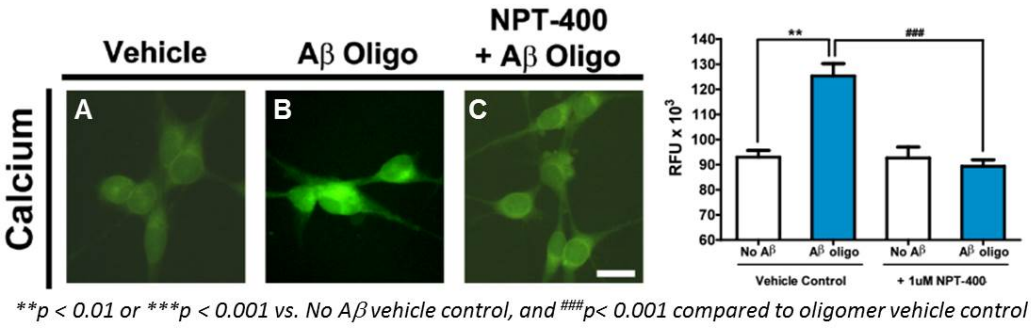

Figure 5.3: **Oligomer-induced increases in intracellular Ca^{2+} are normalized by NPT-440-1.** B103 rat neuronal cells were incubated for 16 hr, followed by Fluo-4 MW Calcium imaging studies (Life Technologies, Carlsbad CA) under the following conditions: **A)** No $A\beta$ vehicle control; **B)** 1 μM of oligomerized $A\beta_{1-42}$; **C)** 1:1 co-incubation of oligomerized $A\beta_{1-42}$ with NPT-440-1. A significant increase ($p < 0.01$) of intracellular Ca^{2+} was induced in the presence $A\beta_{1-42}$ (B). The addition of NPT-440-1 during incubation with $A\beta_{1-42}$ prevented this increase and Ca^{2+} levels remained comparable to the vehicle control (C).

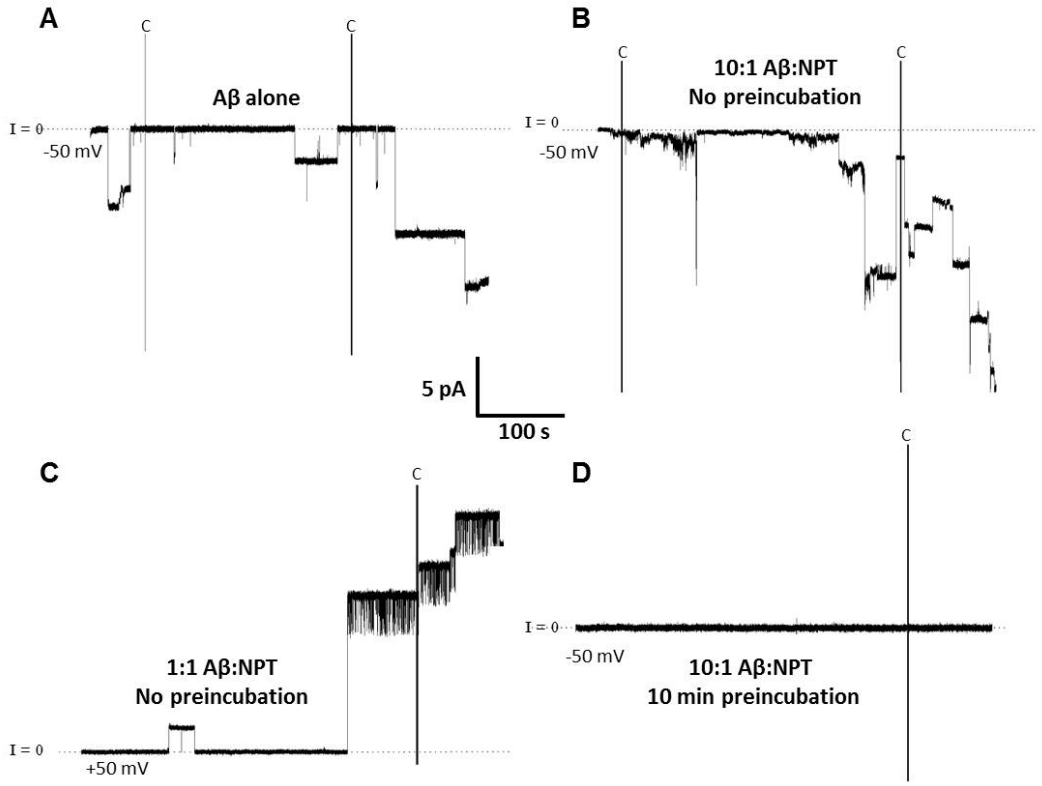

Figure 5.4: **Preincubation prior to membrane introduction is necessary to prevent pore activity. A)** $A\beta_{1-42}$ alone shows the expected multi-level conductance behavior; **B)**10:1 without preincubation shows no modulation in pore activity; **C)** 1:1 without preincubation also shows no modulation of pore activity despite the ten times greater NPT-440-1 concentration; **D)** 10:1 preincubated $10-15$ min prior to addition into the PLB recording chamber showed no pore activity over 4+ hrs of recording. A structural change is likely induced within the peptide during incubation. Further, the need for preincubation prior to membrane introduction implies fast binding/insertion of the peptide into the membrane where it is shielded from the effects of the compound.

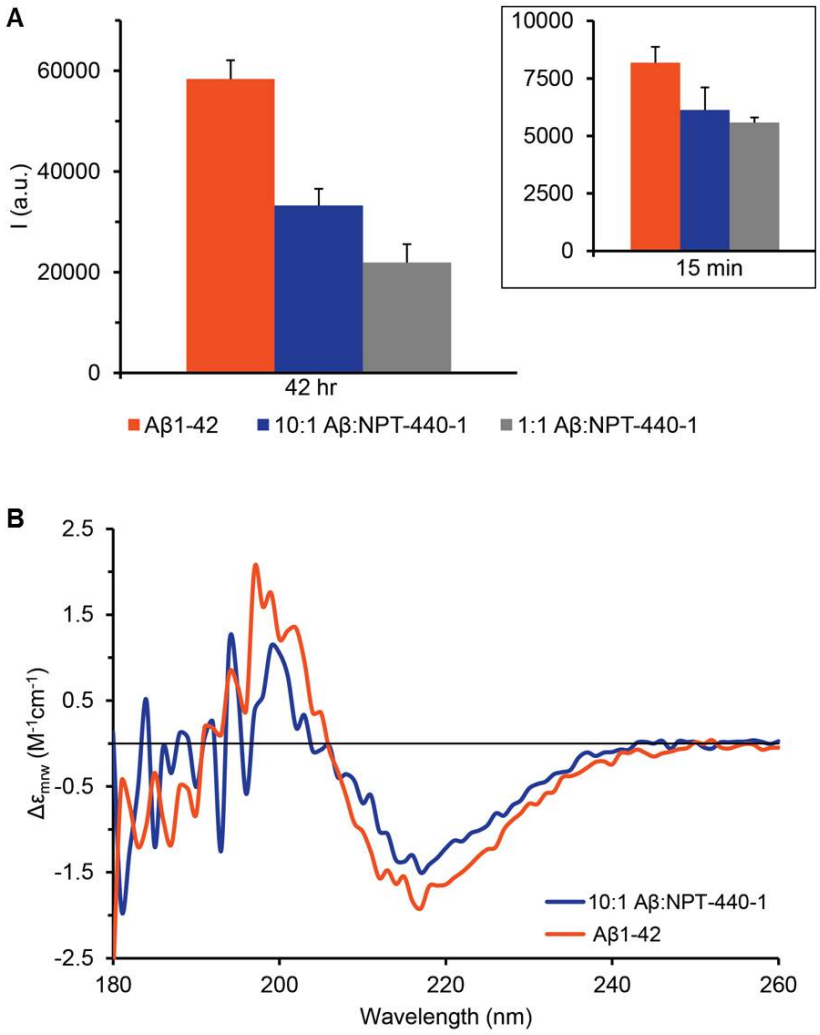

Figure 5.5: **NPT-440-1 causes a reduction in β-sheet secondary structure. A)** ThT fluorescence indicates a concentration-dependent inhibitory effect of NPT-440-1 on $A\beta_{1-42}$ aggregation. Both 10:1 (blue) and 1:1 (grey) peptide:compound ratios significantly reduced ($p < 0.001$) the maximum ThT signal. This pattern is seen even within the first 15 min (inset), with significant reduction in ThT fluorescence intensity at both 10:1 ($p < 0.05$) and 1:1 ($p < 0.001$). **B)** The CD spectra of $A\beta_{1-42}$ (orange) shows β-sheet secondary structure with a characteristic positive peak at 195 nm and a negative peak at 218 nm. 10:1 treatment with NPT-440-1 shows a small, but clear, upward shift at 218 nm indicating a reduction in β-character after 15 min of incubation.

Chapter 6

Conclusions

Over the past several decades, the prevailing hypothesis for AD pathophysiology has taken shape and points to dysregulation of intracellular ionic homeostasis as a key element in the $A\beta$-induced cascade that leads to neuronal death. While the end result is clear, the mechanism underlying this dysregulation is not fully understood. Since the introduction of the channel hypothesis, now more than 20 years ago, BLM/PLB has played an important role in characterizing the ionic flux caused by various amyloid peptides, including $A\beta$. But while we can observe the end result—ionic flux—the necessarily structural elements and mechanism of pore formation/insertion are not completely clear. Understanding these underlying mechanisms is crucial to the development of effective pharmaceutical interventions.

In Chapter 2, we used BLM and MD simulations to show that $A\beta_{pE3-42}$ forms ionic pores following the same general activity pattern as $A\beta_{1-42}$ pores. Significantly, $A\beta_{pE3-42}$ pores display higher conductance than $A\beta_{1-42}$, particularly in the $100-200$ pS range. Structurally, $A\beta_{pE3-42}$ and $A\beta_{1-42}$ pores have similar dimensions, but the N-termini of $A\beta_{pE}$ pores tend to reside in the hydrophobic lipid core, providing the $A\beta_{pE3-42}$ pores with higher stability compared with the $A\beta_{1-42}$ pores. We attribute the enhanced in vitro cytotoxicity of $A\beta_{pE}$ peptides to the increased conductance and greater stability as compared to $A\beta_{1-42}$.

While we attributed the increased cytotoxicity of $A\beta_{pE3-42}$ to the higher conductances seen in our histogram, the true relevance of this measure to cell death was questionable. To address this, Chapter 3 presents a newly developed analysis program

that measures the total conductive flux through the membrane. This program corrects for the bias toward spike and burst activity that histograms introduce and provides an objection threshold for toxicity comparison. We show proof of concept by analyzing the previous data on $A\beta_{pE3-42}$ and $A\beta_{1-42}$ recordings. While statistically meaningful analysis will require many more bilayer recording experiments, emerging high throughput technologies provide the means to achieve this benchmark.

Chapters 4 & 5 focused on two small molecule compounds targeted at preventing $A\beta_{1-42}$ pore activity. In Chapter 4 we used a membrane embedded compound and found that while pore dimensions remained largely unaffected, the electrical activity was modulated, but not completely inhibited, by presence of the compound. Based on our results we suggest that activity modulation is likely the result of either a structural change within the pore body or compound binding within the pore. Chapter 5 presents an aqueous mobile compound. We demonstrate that the compound completely inhibits pore activity when preincubated with $A\beta_{1-42}$ suggesting a conformational change during incubation. Investigation of the peptide secondary structure strongly suggests that there was a reduction in β-sheet character during the incubation. We propose that pharmacologic agents that target the β-sheet nature of amyloid proteins could prove effective in slowing or preventing the progression of AD and should be investigated further.

In summary, the work in this dissertation has aimed to understand the reasons for differential levels of toxicity amongst $A\beta$ species, while developing new tools for their study. Additionally we have used small molecule agents to provide insight into the mechanistic and structural pathways of pore formation. The studies contained within will aid the future design of small molecule pharmaceuticals for the treatment/prevention AD.

The content of Chapter 6 is original. The dissertation author was the primary author.

Appendix A

Supplementary Figures for Chapter 2

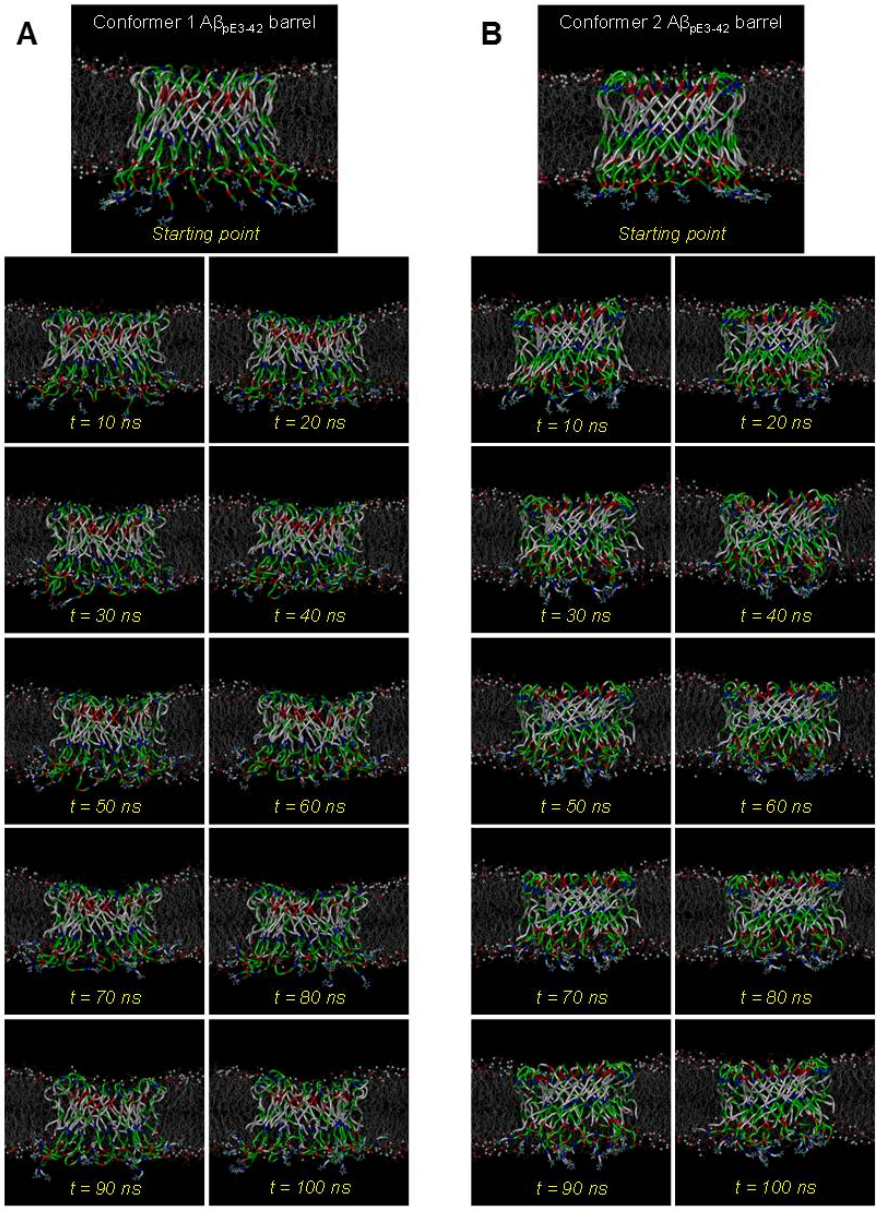

Figure A.1: **Time series of A$\beta_{\mathbf{pE3-42}}$ barrel conformations.** Conceptual design of annular structure for the 18-mer $A\beta_{pE3-42}$ barrels represented in the starting point of production run in the DOPS/POPE (mole ratio 1:2) bilayer and snapshots of the barrel conformations at each 10 ns for the **(A)** conformer 1 and **(B)** conformer 2 $A\beta_{pE3-42}$ barrels. In the peptide ribbon, hydrophobic, polar/Gly, positively charged, and negatively charged residues are colored white, green, blue, and red, respectively. The pE3 N-terminal termini are highlighted as threads. In lateral view of the bilayer, lipid tail as gray thread and phosphate atoms as small gray and red beads for POPE and DOPS, respectively, are shown.

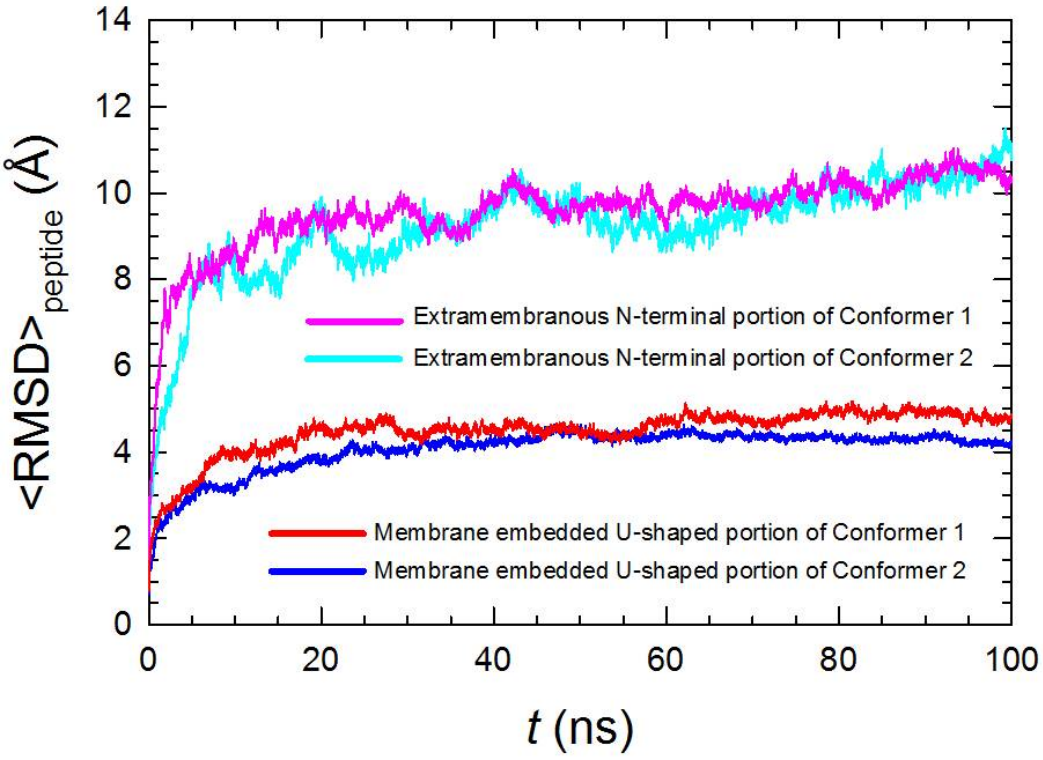

Figure A.2: **Time series of peptide averaged root-mean-squared deviation.** Root-mean-squared deviation ($< RMSD >_{peptide}$) from the starting point during MD simulation is plotted for backbone heavy atoms of the membrane embedded U-shaped portion and extramembranous N-terminal portion of $A\beta_{pE3-42}$ barrels.

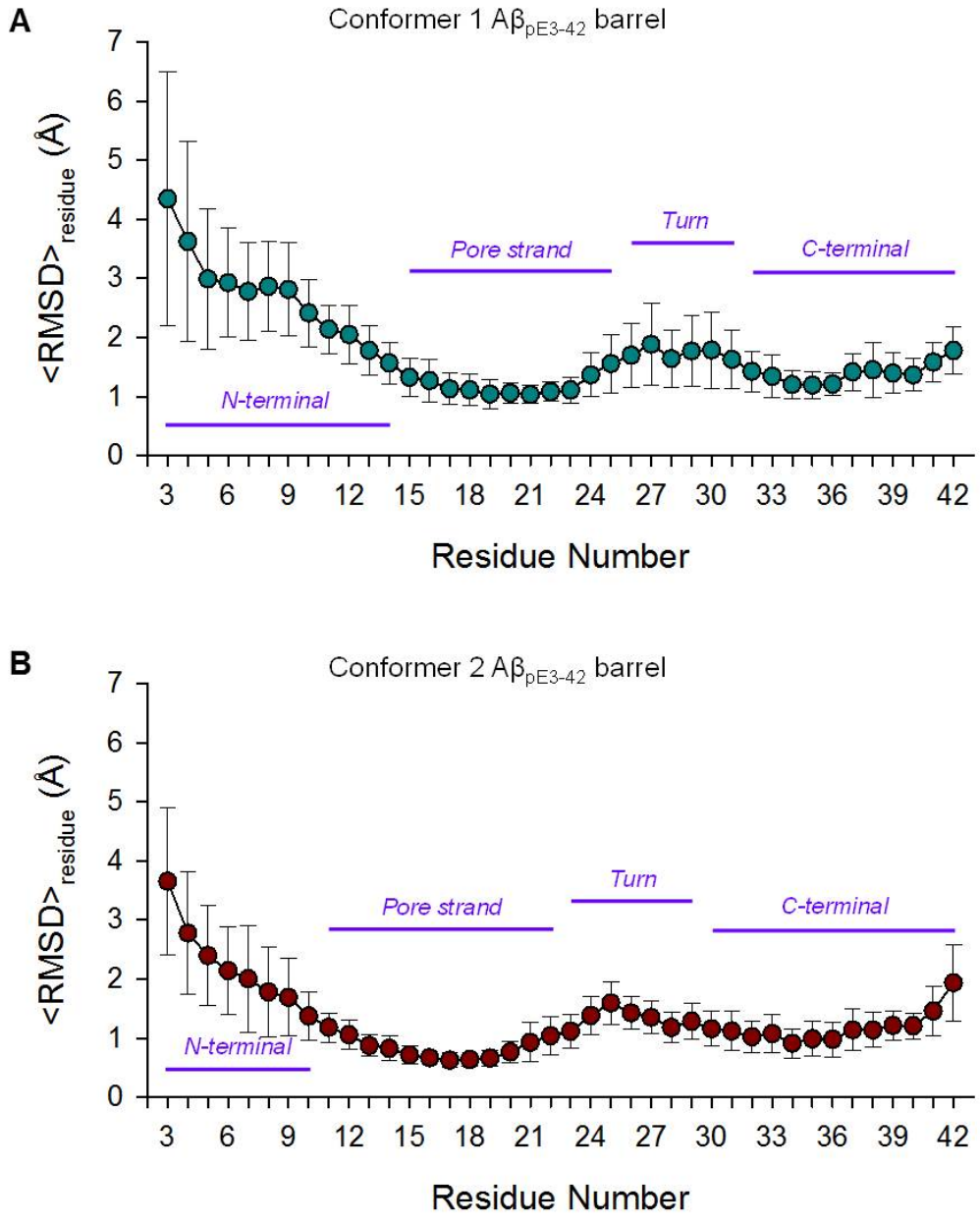

Figure A.3: **Residue averaged root-mean-squared deviation over the simulation time.** $< RMSD >_{residue}$ from the starting point for backbone heavy atoms of the peptides and then averaged over the simulation time for **(A)** conformer 1 and **(B)** conformer 2 $A\beta_{pE3-42}$ barrels.

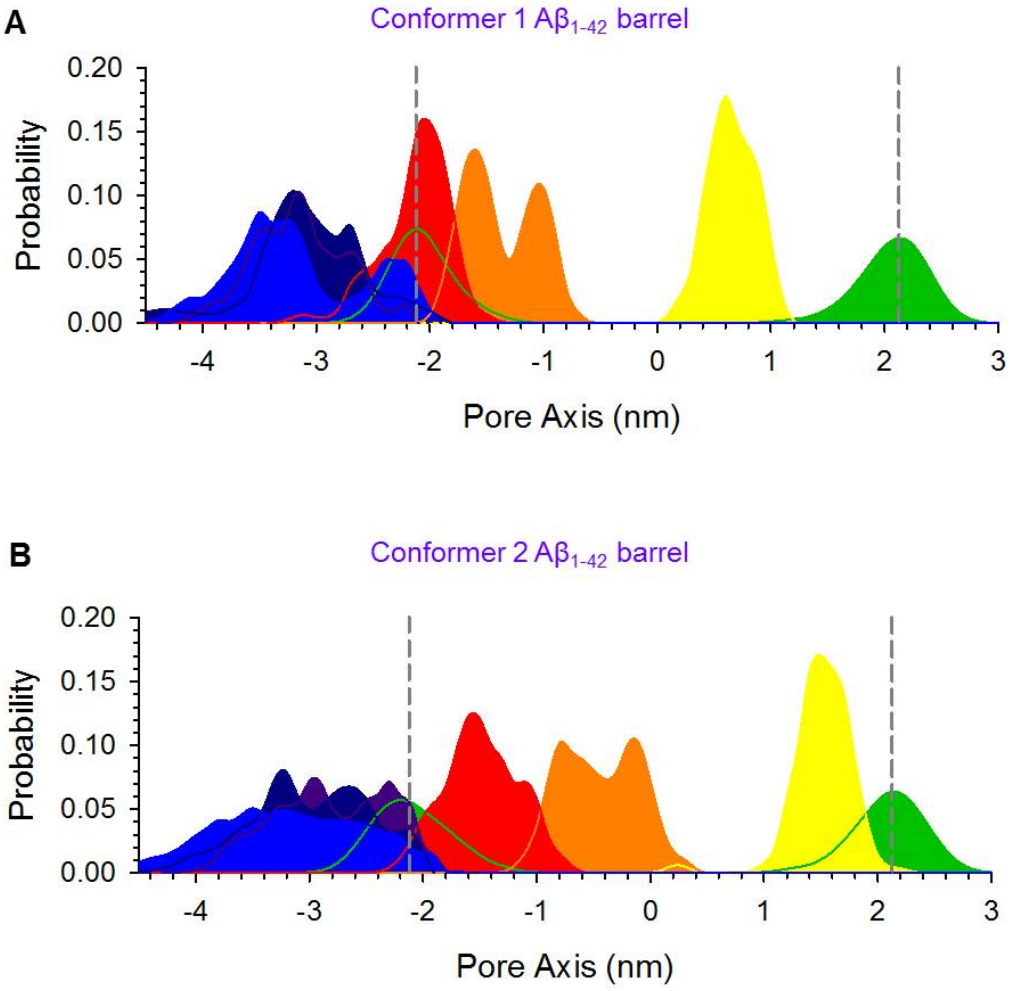

Figure A.4: **Probability distribution functions for selected residues in the wild-type Aβ_{1-42} barrels** Asp1 (blue), Glu3 (dark blue), Arg5 (purple), Glu11 (red), Lys16 (orange), Glu22 (yellow), and the phosphate group of lipid head, PO4 (green),as a function of the distance along the pore center axis for **(A)** conformer 1 and **(B)** conformer 2 $A\beta_{1-42}$ barrels in an anionic bilayer composed of DOPS and POPE with a mole ratio 1:2. Dotted lines indicate the locations of bilayer surfaces.

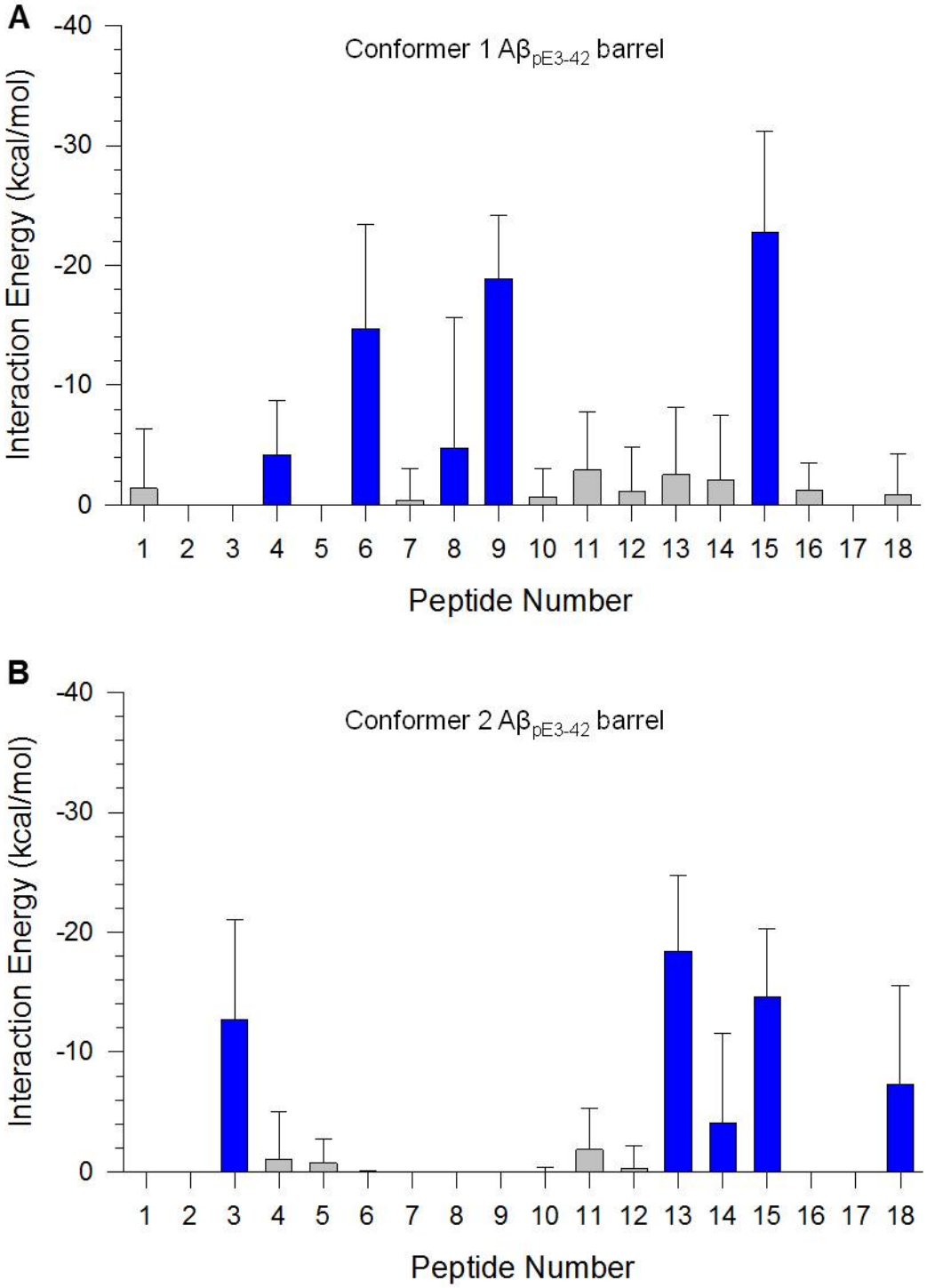

Figure A.5: **Interaction energies of pE3 residue with lipids.** **(A)** conformer 1 and **(B)** conformer 2 $A\beta_{pE3-42}$ barrels. Blue bars denote the strong pE3/lipid interaction.

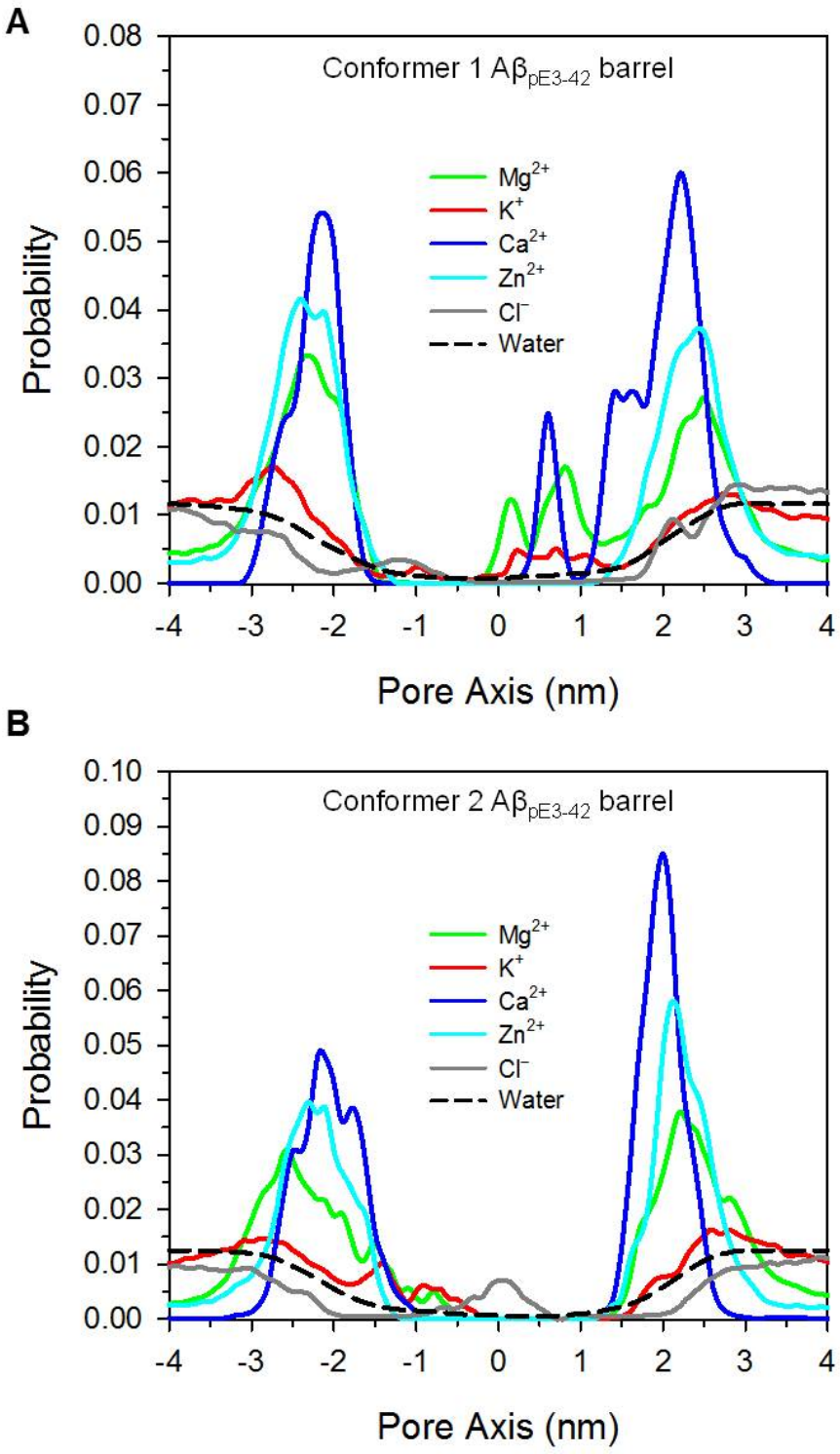

Figure A.6: **Probability distribution functions for ions.** Mg^{2+} (green line), K^{+} (red line), Ca^{2+} (blue line), Zn^{2+} (cyan line), Cl^{-} (gray line), and water (black dashed line) as a function of the distance along the pore center axis for **(A)** conformer 1 and **(B)** conformer 2 $A\beta_{pE3-42}$ barrels.

References

[1] Alzheimer A (1907) Über eine eigenartige Erkrankung der Hirnrinde. Allg Zschr Psychiatr Psych gerichtl Med : 146–148.

[2] Alzheimer A (1911) Über eigenartige Krankheitsfälle des späteren Alters. Z Ges Neurol Psychiatr : 356–385.

[3] Bielschowsky M (1902) Die Silberimprägnation der Achsencylinder. Neurologisches Zentralblatt : 579–584.

[4] Hardy J (2006) A hundred years of Alzheimer's disease research. Neuron 52: 3–13.

[5] Dahm R (2006) Alzheimer's discovery. Current biology : CB 16: R906–10.

[6] Blessed G, Tomlinson BE, Roth M (1968) The association between quantitative measures of dementia and of senile change in the cerebral grey matter of elderly subjects. British Journal of Psychiatry 114: 797–811.

[7] Tomlinson BE, Blessed G, Roth M (1968) Observations on the brains of non-demented old people. Journal of the Neurological Sciences 7: 331–356.

[8] Tomlinson B, Blessed G, Roth M (1970) Observations on the brains of demented old people. Journal of the Neurological Sciences 11: 205–242.

[9] Barker WW, Luis CA, Kashuba A, Luis M, Harwood DG, Loewenstein D, Waters C, Jimison P, Shepherd E, Sevush S, Graff-Radford N, Newland D, Todd M, Miller B, Gold M, Heilman K, Doty L, Goodman I, Robinson B, Pearl G, Dickson D, Duara R (2002) Relative Frequencies of Alzheimer Disease, Lewy Body, Vascular and Frontotemporal Dementia, and Hippocampal Sclerosis in the State of Florida Brain Bank. Alzheimer Disease & Associated Disorders 16: 203–212.

[10] Wilson RS, Segawa E, Boyle PA, Anagnos SE, Hizel LP, Bennett DA (2012) The natural history of cognitive decline in Alzheimer's disease. Psychology and aging 27: 1008–17.

[11] Alzheimer's Association (2015) 2015 Alzheimer's disease facts and figures. Alzheimer's & Dementia 11: 332–384.

[12] Querfurth HW, LaFerla FM (2010) Alzheimer's disease. The New England journal of medicine 362: 329–44.

[13] Selkoe DJ (1989) Amyloid beta protein precursor and the pathogenesis of Alzheimer's disease. Cell 58: 611–2.

[14] Selkoe DJ (1989) Aging, amyloid, and Alzheimer's disease. The New England journal of medicine 320: 1484–7.

[15] Selkoe DJ (1991) The molecular pathology of Alzheimer's disease. Neuron 6: 487–98.

[16] Selkoe DJ (1991) Alzheimer's disease. In the beginning... Nature 354: 432–3.

[17] Wolfe MS, Selkoe DJ (2010) Giving Alzheimer's the old one-two. Cell 142: 194–6.

[18] Hardy Ja, Higgins Ga (1992) Alzheimer's disease: the amyloid cascade hypothesis. Science (New York, NY) 256: 184–185.

[19] Motte J, Williams RS (1989) Age-related changes in the density and morphology of plaques and neurofibrillary tangles in Down syndrome brain. Acta neuropathologica 77: 535–546.

[20] Joachim CL, Morris JH, Selkoe DJ (1989) Diffuse senile plaques occur commonly in the cerebellum in Alzheimer's disease. The American journal of pathology 135: 309–19.

[21] Sipe JD, Cohen aS (2000) Review: history of the amyloid fibril. Journal of structural biology 130: 88–98.

[22] Kagan BL, Azimov R, Azimova R (2004) Amyloid peptide channels. Journal of Membrane Biology 202: 1–10.

[23] Quist A, Doudevski I, Lin H, Azimova R, Ng D, Frangione B, Kagan B, Ghiso J, Lal R (2005) Amyloid ion channels: a common structural link for protein-misfolding disease. Proceedings of the National Academy of Sciences of the United States of America 102: 10427–10432.

[24] Kagan BL, Hirakura Y, Azimov R, Azimova R (2001) The channel hypothesis of Huntington's disease. Brain research bulletin 56: 281–4.

[25] Kagan BL, Hirakura Y, Azimov R, Azimova R, Lin MC (2002) The channel hypothesis of Alzheimer's disease: Current status. Peptides 23: 1311–1315.

[26] Kagan BL (2011) Antimicrobial Amyloids? Biophys J 100: 1597–1598.

[27] Kyle RA (2001) Amyloidosis: a convoluted story. British journal of haematology 114: 529–38.

[28] Chiti F, Dobson CM (2006) Protein misfolding, functional amyloid, and human disease. Annu Rev Biochem 75: 333–366.

[29] Temussi PA, Masino L, Pastore A (2003) From Alzheimer to Huntington: Why is a structural understanding so difficult? EMBO Journal 22: 355–361.

[30] Walsh DM, Selkoe DJ (2007) A beta oligomers - a decade of discovery. Journal of neurochemistry 101: 1172–1184.

[31] Merlini G, Bellotti V (2003) Molecular mechanisms of amyloidosis. The New England journal of medicine 349: 583–96.

[32] Gillmore JD, Hawkins PN, Pepys MB (1997) Amyloidosis: a review of recent diagnostic and therapeutic developments. British journal of haematology 99: 245–56.

[33] Soto C (2003) Unfolding the role of protein misfolding in neurodegenerative diseases. Nature reviews Neuroscience 4: 49–60.

[34] Murray ME, Lowe VJ, Graff-Radford NR, Liesinger AM, Cannon A, Przybelski SA, Rawal B, Parisi JE, Petersen RC, Kantarci K, Ross OA, Duara R, Knopman DS, Jack CR, Dickson DW (2015) Clinicopathologic and 11C-Pittsburgh compound B implications of Thal amyloid phase across the Alzheimer's disease spectrum. Brain : a journal of neurology 138: awv050–.

[35] Hardy J, Selkoe DJ (2002) The amyloid hypothesis of Alzheimer's disease: progress and problems on the road to therapeutics. Science (New York, NY) 297: 353–356.

[36] Thinakaran G, Koo EH (2008) Amyloid precursor protein trafficking, processing, and function. Journal of Biological Chemistry 283: 29615–29619.

[37] Karran E, Mercken M, De Strooper B (2011) The amyloid cascade hypothesis for Alzheimer's disease: an appraisal for the development of therapeutics. Nature reviews Drug discovery 10: 698–712.

[38] O'Brien RJ, Wong PC (2011) Amyloid precursor protein processing and Alzheimer's disease. Annual review of neuroscience 34: 185–204.

[39] Zhang Yw, Thompson R, Zhang H, Xu H (2011) APP processing in Alzheimer's disease. Molecular brain 4: 3.

[40] Nilsberth C, Westlind-Danielsson A, Eckman CB, Condron MM, Axelman K, Forsell C, Stenh C, Luthman J, Teplow DB, Younkin SG, Näslund J, Lannfelt L (2001) The 'Arctic' APP mutation (E693G) causes Alzheimer's disease by enhanced Abeta protofibril formation. Nature neuroscience 4: 887–93.

[41] Jawhar S, Wirths O, Bayer Ta (2011) Pyroglutamate amyloid-β (Aβ): A hatchet man in alzheimer disease. Journal of Biological Chemistry 286: 38825–38832.

[42] Saido TC, Iwatsubo T, Mann DM, Shimada H, Ihara Y, Kawashima S (1995) Dominant and differential deposition of distinct beta-amyloid peptide species, Aβ N3(pE), in senile plaques. Neuron 14: 457–466.

[43] Joachim CL, Mori H, Selkoe DJ (1989) Amyloid beta-protein deposition in tissues other than brain in Alzheimer's disease. Nature 341: 226–30.

[44] Jang H, Arce FT, Mustata M, Ramachandran S, Capone R, Nussinov R, Lal R (2011) Antimicrobial protegrin-1 forms amyloid-like fibrils with rapid kinetics suggesting a functional link. Biophysical Journal 100: 1775–1783.

[45] Jang H, Arce FT, Ramachandran S, Capone R, Azimova R, Kagan BL, Nussinov R, Lal R (2010) Truncated beta-amyloid peptide channels provide an alternative mechanism for Alzheimer's Disease and Down syndrome. Proceedings of the National Academy of Sciences of the United States of America 107: 6538–6543.

[46] Jang H, Teran Arce F, Ramachandran S, Capone R, Lal R, Nussinov R (2010) Structural convergence among diverse, toxic beta-sheet ion channels. Journal of Physical Chemistry B 114: 9445–9451.

[47] Lal R, Lin H, Quist AP (2007) Amyloid beta ion channel: 3D structure and relevance to amyloid channel paradigm. Biochimica et Biophysica Acta - Biomembranes 1768: 1966–1975.

[48] Lin H, Bhatia R, Lal R (2001) Amyloid beta protein forms ion channels: implications for Alzheimer's disease pathophysiology. The FASEB journal : official publication of the Federation of American Societies for Experimental Biology 15: 2433–2444.

[49] Lin H, Zhu YJ, Lal R (1999) Amyloid beta protein (1-40) forms calcium-permeable, Zn2+-sensitive channel in reconstituted lipid vesicles. Biochemistry 38: 11189–96.

[50] Mustata M, Capone R, Jang H, Arce FT, Ramachandran S, Lal R, Nussinov R (2009) K3 fragment of amyloidogenic β2-microglobulin forms ion channels: Implication for dialysis related amyloidosis. Journal of the American Chemical Society 131: 14938–14945.

[51] Parbhu A, Lin H, Thimm J, Lal R (2002) Imaging real-time aggregation of amyloid beta protein (1 – 42) by atomic force microscopy. Neuroscience Research 23: 1265–1270.

[52] Rhee SK, Quist AP, Lal R (1998) Amyloid β protein-(1-42) forms calcium-permeable, Zn2+-sensitive channel. Journal of Biological Chemistry 273: 13379–13382.

[53] Zhu YJ, Lin H, Lal R (2000) Fresh and nonfibrillar amyloid beta protein(1-40) induces rapid cellular degeneration in aged human fibroblasts: evidence for AbetaP-channel-mediated cellular toxicity. FASEB journal : official publication of the Federation of American Societies for Experimental Biology 14: 1244–54.

[54] Haass C, Hung AY, Selkoe DJ (1991) Processing of beta-amyloid precursor protein in microglia and astrocytes favors an internal localization over constitutive secretion. The Journal of neuroscience : the official journal of the Society for Neuroscience 11: 3783–93.

[55] Selkoe DJ (1989) Biochemistry of altered brain proteins in Alzheimer's disease. Annual review of neuroscience 12: 463–90.

[56] Capone R, Mustata M, Jang H, Arce FT, Nussinov R, Lal R (2010) Antimicrobial protegrin-1 forms ion channels: Molecular dynamic simulation, atomic force microscopy, and electrical conductance studies. Biophysical Journal 98: 2644–2652.

[57] Arispe N, Pollard HB, Rojas E (1993) Giant multilevel cation channels formed by Alzheimer disease amyloid beta-protein [A beta P-(1-40)] in bilayer membranes. Proceedings of the National Academy of Sciences of the United States of America 90: 10573–10577.

[58] Arispe N, Pollard HB, Rojas E (1994) beta-Amyloid Ca(2+)-channel hypothesis for neuronal death in Alzheimer disease. Molecular and cellular biochemistry 140: 119–25.

[59] Arispe N, Rojas E, Pollard HB (1993) Alzheimer disease amyloid beta protein forms calcium channels in bilayer membranes: blockade by tromethamine and aluminum. Proceedings of the National Academy of Sciences of the United States of America 90: 567–571.

[60] Durell SR, Guy HR, Arispe N, Rojas E, Pollard HB (1994) Theoretical models of the ion channel structure of amyloid beta-protein. Biophysical journal 67: 2137–45.

[61] Pollard HB, Rojas E, Arispe N (1993) A new hypothesis for the mechanism of amyloid toxicity, based on the calcium channel activity of amyloid β protein

(AβP) in phospholipid bilayer membranes. Annals of the New York Academy of Sciences 695: 165–168.

[62] Pollard JR, Arispe N, Rojas E, Pollard HB (1994) A geometric sequence that accurately describes allowed multiple conductance levels of ion channels: the "three-halves (3/2) rule". Biophysical journal 67: 647–55.

[63] Hirakura Y, Kagan BL (2001) Pore formation by beta-2-microglobulin: a mechanism for the pathogenesis of dialysis associated amyloidosis. Amyloid : the international journal of experimental and clinical investigation : the official journal of the International Society of Amyloidosis 8: 94–100.

[64] Hirakura Y, Lin MC, Kagan BL (1999) Alzheimer amyloid abeta1-42 channels: effects of solvent, pH, and Congo Red. Journal of neuroscience research 57: 458–466.

[65] Lin McA, Kagan BL (2002) Electrophysiologic properties of channels induced by Abeta25-35 in planar lipid bilayers. Peptides 23: 1215–1228.

[66] Mattson MP, Cheng B, Davis D, Bryant K, Lieberburg I, Rydel RE (1992) beta-Amyloid peptides destabilize calcium homeostasis and render human cortical neurons vulnerable to excitotoxicity. The Journal of neuroscience : the official journal of the Society for Neuroscience 12: 376–89.

[67] Loo DT, Copani A, Pike CJ, Whittemore ER, Walencewicz AJ, Cotman CW (1993) Apoptosis is induced by beta-amyloid in cultured central nervous system neurons. Proceedings of the National Academy of Sciences of the United States of America 90: 7951–5.

[68] Smale G, Nichols NR, Brady DR, Finch CE, Horton WE (1995) Evidence for apoptotic cell death in Alzheimer's disease. Experimental neurology 133: 225–30.

[69] Lorenzo A, Yankner BA (1994) Beta-amyloid neurotoxicity requires fibril formation and is inhibited by congo red. Proceedings of the National Academy of Sciences of the United States of America 91: 12243–7.

[70] Tjernberg LO, Näslund J, Lindqvist F, Johansson J, Karlström AR, Thyberg J, Terenius L, Nordstedt C (1996) Arrest of β-Amyloid Fibril Formation by a Pentapeptide Ligand. Journal of Biological Chemistry 271: 8545–8548.

[71] McLean Ca, Cherny Ra, Fraser FW, Fuller SJ, Smith MJ, Beyreuther K, Bush AI, Masters CL (1999) Soluble pool of Aβ amyloid as a determinant of severity of neurodegeneration in Alzheimer's disease. Annals of Neurology 46: 860–866.

[72] Bhatia R, Lin H, Lal R (2000) Fresh and globular amyloid beta protein (1-42) induces rapid cellular degeneration: evidence for AβP channel-mediated cellular toxicity. FASEB journal : official publication of the Federation of American Societies for Experimental Biology 14: 1233–1243.

[73] Walsh DM, Klyubin I, Fadeeva JV, Cullen WK, Anwyl R, Wolfe MS, Rowan MJ, Selkoe DJ (2002) Naturally secreted oligomers of amyloid beta protein potently inhibit hippocampal long-term potentiation in vivo. Nature 416: 535–539.

[74] Näslund J, Haroutunian V, Mohs R, Davis KL, Davies P, Greengard P, Buxbaum JD Correlation between elevated levels of amyloid beta-peptide in the brain and cognitive decline. JAMA 283: 1571–7.

[75] Bucciantini M, Giannoni E, Chiti F, Baroni F, Formigli L, Zurdo J, Taddei N, Ramponi G, Dobson CM, Stefani M (2002) Inherent toxicity of aggregates implies a common mechanism for protein misfolding diseases. Nature 416: 507–511.

[76] Etcheberrigaray R, Ito E, Kim CS, Alkon DL (1994) Soluble beta-amyloid induction of Alzheimer's phenotype for human fibroblast K+ channels. Science (New York, NY) 264: 276–9.

[77] Gibson G, Gunasekera N, Lee M, Lelyveld V, El-Agnaf OMA, Wright A, Austen B (2004) Oligomerization and neurotoxicity of the amyloid ADan peptide implicated in familial Danish dementia. Journal of neurochemistry 88: 281–90.

[78] Koistinaho M, Ort M, Cimadevilla JM, Vondrous R, Cordell B, Koistinaho J, Bures J, Higgins LS (2001) Specific spatial learning deficits become severe with age in beta -amyloid precursor protein transgenic mice that harbor diffuse beta -amyloid deposits but do not form plaques. Proceedings of the National Academy of Sciences of the United States of America 98: 14675–80.

[79] Williams TL, Serpell LC (2011) Membrane and surface interactions of Alzheimer's Aβ peptide - Insights into the mechanism of cytotoxicity. FEBS Journal 278: 3905–3917.

[80] Arispe N, Pollard HB, Rojas E (1994) The ability of amyloid beta-protein [A beta P (1-40)] to form Ca2+ channels provides a mechanism for neuronal death in Alzheimer's disease. Annals of the New York Academy of Sciences 747: 256–266.

[81] Jang H, Connelly L, Teran Arce F, Ramachandran S, Kagan BL, Lal R, Nussinov R (2013) Mechanisms for the insertion of toxic, fibril-like β-amyloid oligomers into the membrane. Journal of Chemical Theory and Computation 9: 822–833.

[82] Connelly L, Jang H, Teran Arce F, Capone R, Kotler SA, Ramachandran S, Kagan BL, Nussinov R, Lal R (2012) Atomic force microscopy and MD simulations reveal pore-like structures of all-D-enantiomer of AlzheimerâĂŹs β-amyloid peptide: relevance to the ion channel mechanism of AD pathology. The Journal of Physical Chemistry B 116: 1728–1735.

[83] Connelly L, Jang H, Teran Arce F, Ramachandran S, Kagan BL, Nussinov R, Lal R (2012) Effects of point substitutions on the structure of toxic Alzheimer's β-amyloid channels: Atomic force microscopy and molecular dynamics simulations. Biochemistry 51: 3031–3038.

[84] Lee J, Gillman AL, Jang H, Ramachandran S, Kagan BL, Nussinov R, Teran Arce F (2014) Role of the fast kinetics of pyroglutamate-modified amyloid-β oligomers in membrane binding and membrane permeability. Biochemistry 53: 4704–4714.

[85] Jang H, Arce FT, Capone R, Ramachandran S, Lal R, Nussinov R (2009) Misfolded amyloid ion channels present mobile β-sheet subunits in contrast to conventional ion channels. Biophysical Journal 97: 3029–3037.

[86] Demuro A, Smith M, Parker I (2011) Single-channel Ca(2+) imaging implicates Abeta1-42 amyloid pores in Alzheimer's disease pathology. J Cell Biol 195: 515–24.

[87] Capone R, Jang H, Kotler Sa, Connelly L, Teran Arce F, Ramachandran S, Kagan BL, Nussinov R, Lal R (2012) All-d-enantiomer of β-amyloid peptide forms ion channels in lipid bilayers. Journal of Chemical Theory and Computation 8: 1143–1152.

[88] Sciacca MFM, Brender JR, Lee DK, Ramamoorthy A (2012) Phosphatidylethanolamine enhances amyloid fiber-dependent membrane fragmentation. Biochemistry 51: 7676–7684.

[89] Jang H, Arce FT, Ramachandran S, Capone R, Lal R, Nussinov R (2010) β-Barrel Topology of Alzheimer's β-Amyloid Ion Channels. Journal of Molecular Biology 404: 917–934.

[90] Capone R, Jang H, Kotler Sa, Kagan BL, Nussinov R, Lal R (2012) Probing structural features of Alzheimers amyloid-β pores in bilayers using site-specific amino acid substitutions. Biochemistry 51: 776–785.

[91] Gillman AL, Jang H, Lee J, Ramachandran S, Kagan BL, Nussinov R, Teran Arce F (2014) Activity and architecture of pyroglutamate-modified amyloid-β (AβpE3-42) pores. Journal of Physical Chemistry B 118: 7335–7344.

[92] Kotler Sa, Walsh P, Brender JR, Ramamoorthy A (2014) Differences between amyloid-β aggregation in solution and on the membrane: insights into elucidation of the mechanistic details of Alzheimer's disease. Chemical Society reviews 43: 6692–700.

[93] Cerf E, Sarroukh R, Tamamizu-Kato S, Breydo L, Derclaye S, Dufrêne YF, Narayanaswami V, Goormaghtigh E, Ruysschaert JM, Raussens V (2009) Antiparallel beta-sheet: a signature structure of the oligomeric amyloid beta-peptide. The Biochemical journal 421: 415–23.

[94] Prangkio P, Yusko EC, Sept D, Yang J, Mayer M (2012) Multivariate analyses of amyloid-beta oligomer populations indicate a connection between pore formation and cytotoxicity. PLoS ONE 7: e47261.

[95] Ahmed M, Davis J, Aucoin D, Sato T, Ahuja S, Aimoto S, Elliott JI, Van Nostrand WE, Smith SO (2010) Structural conversion of neurotoxic amyloid-beta(1-42) oligomers to fibrils. Nature structural & molecular biology 17: 561–7.

[96] Mueller P, Rudin DO, Tien HT, Wescott WC (1962) Reconstitution of cell membrane structure in vitro and its transformation into an excitable system. Nature 194: 979–980.

[97] White SH (1972) Analysis of the torus surrounding planar lipid bilayer membranes. Biophysical journal 12: 432–445.

[98] Montal M, Mueller P (1972) Formation of bimolecular membranes from lipid monolayers and a study of their electrical properties. Proceedings of the National Academy of Sciences of the United States of America 69: 3561–6.

[99] Anzai K, Ogawa K, Ozawa T, Yamamoto H (2001) Quantitative comparison of two types of planar lipid bilayers–folded and painted–with respect to fusion with vesicles. Journal of biochemical and biophysical methods 48: 283–91.

[100] Labarca P, Coronado R, Miller C (1980) Thermodynamic and kinetic studies of the gating behavior of a K+-selective channel from the sarcoplasmic reticulum membrane. The Journal of general physiology 76: 397–24.

[101] Lattorre R (1986) The large calcium-activated potassium channel. In: Miller C, editor, Ion Channel Reconstitution, Boston, MA: Springer US. pp. 431–467. doi: 10.1007/978-1-4757-1361-9.

[102] Moczydlowski E, Garber SS, Miller C (1984) Batrachotoxin-activated Na+ channels in planar lipid bilayers. Competition of tetrodotoxin block by Na+. The Journal of general physiology 84: 665–86.

[103] Haydon DA, Hladky SB (1972) Ion transport across thin lipid membranes: a critical discussion of mechanisms in selected systems. Quarterly Reviews of Biophysics 5: 187.

[104] Sakmann B, Neher E (1984) Patch clamp techniques for studying ionic channels in excitable membranes. Annual review of physiology 46: 455–72.

[105] Molleman A (2003) Patch Clamping: An Introductory Guide to Patch Clamp Electrophysiology. John Wiley & Sons.

[106] Mirzabekov TA, Silberstein AY, Kagan BL (1999) Use of planar lipid bilayer membranes for rapid screening of membrane active compounds. Methods in enzymology 294: 661–74.

[107] Kourie JI, Henry CL, Farrelly P (2001) Diversity of amyloid beta protein fragment [1-40]-formed channels. Cellular and molecular neurobiology 21: 255–84.

[108] Hebert LE, Weuve J, Scherr PA, Evans DA (2013) Alzheimer disease in the United States (2010-2050) estimated using the 2010 census. Neurology 80: 1778–83.

[109] Kotler SA (2011) Probing Structural Features of Amyloid-Beta Ion Channels in Membranes Using A-Beta Mutants. M.S. thesis, University of California, San Diego, La Jolla.

[110] Tanzi RE, Bertram L (2005) Twenty Years of the Alzheimer's Disease Amyloid Hypothesis-A Genetic Perspective. Cell 120: 545–555.

[111] Iversen LL, Mortishiresmith RJ, Pollack SJ, Shearman MS (1995) The Toxicity in-Vitro of Beta-Amyloid Protein. Biochem J 311: 1–16.

[112] Jakob-Roetne R, Jacobsen H (2009) Alzheimer's disease: from pathology to therapeutic approaches. Angewandte Chemie (International ed in English) 48: 3030–3059.

[113] Saido TC, Yamao-Harigaya W, Iwatsubo T, Kawashima S (1996) Amino- and carboxyl-terminal heterogeneity of β-amyloid peptides deposited in human brain. Neuroscience Letters 215: 173–176.

[114] Piccini A, Russo C, Gliozzi A, Relini A, Vitali A, Borghi R, Giliberto L, Armirotti A, D'Arrigo C, Bachi A, Cattaneo A, Canale C, Torrassa S, Saido TC, Markesbery W, Gambetti P, Tabaton M (2005) β-amyloid is different in normal aging and in Alzheimer disease. Journal of Biological Chemistry 280: 34186–34192.

[115] Tabaton M, Piccini A (2005) Role of water-soluble amyloid-beta in the pathogenesis of Alzheimer's disease. Int J Exp Pathol 86: 139–145.

[116] Capone RF, Quiroz FG, Prangkio P, Saluja I, Sauer AM, Bautista M, Turner RS, Yang J, Mayer M (2009) Amyloid-β Ion Channels in Artificial Lipid Bilayers and Neuronal Cells. Resolving a Controversy. Biophysical Journal 96: 389a.

[117] Kim HY, Cho MK, Kumar A, Maier E, Siebenhaar C, Becker S, Fernandez CO, Lashuel HA, Benz R, Lange A (2009) Structural properties of pore-forming oligomers of α-synuclein. Journal of the American Chemical Society 131: 17482–17489.

[118] Jang H, Connelly L, Arce FT, Ramachandran S, Lal R, Kagan BL, Nussinov R (2013) Alzheimer's disease: which type of amyloid-preventing drug agents to employ? Physical chemistry chemical physics : PCCP 15: 8868–77.

[119] Arce FT, Jang H, Ramachandran S, Landon PB, Nussinov R, Lal R (2011) Polymorphism of amyloid β peptide in different environments: implications for membrane insertion and pore formation. Soft Matter 7: 5267.

[120] Butterfield SM, Lashuel Ha (2010) Amyloidogenic protein-membrane interactions: Mechanistic insight from model systems. Angewandte Chemie - International Edition 49: 5628–5654.

[121] Sciacca MFM, Kotler SA, Brender JR, Chen J, Lee Dk, Ramamoorthy A (2012) Two-step mechanism of membrane disruption by Aβ through membrane fragmentation and pore formation. Biophysical journal 103: 702–10.

[122] Wirths O, Breyhan H, Cynis H, Schilling S, Demuth HU, Bayer Ta (2009) Intraneuronal pyroglutamate-Abeta 3-42 triggers neurodegeneration and lethal neurological deficits in a transgenic mouse model. Acta Neuropathologica 118: 487–496.

[123] Soderberg M, Edlund C, Alafuzoff I, Kristensson K, Dallner G (1992) Lipid composition in different regions of the brain in Alzheimer's disease/senile dementia of Alzheimer's type. Journal of neurochemistry 59: 1646–1653.

[124] Wells K, Farooqui AA, Liss L, Horrocks LA (1995) Neural membrane phospholipids in alzheimer disease. Neurochemical Research 20: 1329–1333.

[125] Nitsch RM, Blusztajn JK, Pittas AG, Slack BE, Growdon JH, Wurtman RJ (1992) Evidence for a membrane defect in Alzheimer disease brain. Proceedings of the National Academy of Sciences 89: 1671–1675.

[126] Svennerholm L, Gottfries CG (1994) Membrane lipids, selectively diminished in Alzheimer brains, suggest synapse loss as a primary event in early-onset form (type I) and demyelination in late-onset form (type II). Journal of neurochemistry 62: 1039–1047.

[127] Lührs T, Ritter C, Adrian M, Riek-Loher D, Bohrmann B, Döbeli H, Schubert D, Riek R (2005) 3D structure of Alzheimer's amyloid-beta(1-42) fibrils. Proceedings of the National Academy of Sciences of the United States of America 102: 17342–17347.

[128] Petkova AT, Yau WM, Tycko R (2006) Experimental constraints on quaternary structure in Alzheimer's beta-amyloid fibrils. Biochemistry 45: 498–512.

[129] Zirah S, Kozin Sa, Mazur AK, Blond A, Cheminant M, Ségalas-Milazzo I, Debey P, Rebuffat S (2006) Structural changes of region 1-16 of the Alzheimer disease amyloid β-peptide upon zinc binding and in vitro aging. Journal of Biological Chemistry 281: 2151–2161.

[130] Brooks BR, Bruccoleri RE, Olafson BD, States DJ, Swaminathan S, Karplus M (1983) CHARMM: A program for macromolecular energy, minimization, and dynamics calculations. Journal of Computational Chemistry 4: 187–217.

[131] Hanwell MD, Curtis DE, Lonie DC, Vandermeerschd T, Zurek E, Hutchison GR (2012) Avogadro: An advanced semantic chemical editor, visualization, and analysis platform. Journal of Cheminformatics 4: 17.

[132] Frisch MJ, Trucks GW, Schlegel HB, Scuseria GE, Robb MA, Cheeseman JR, Scalmani G, Barone V, Mennucci B, Petersson GA (2013) Gaussian 09, Revision B. 01; Wallingford, CT, 2009 .

[133] Schulz GE (2002) The structure of bacterial outer membrane proteins. Biochimica et biophysica acta 1565: 308–317.

[134] Jang H, Teran Arce F, Ramachandran S, Kagan BL, Lal R, Nussinov R (2014) Disordered amyloidogenic peptides may insert into the membrane and assemble into common cyclic structural motifs. Chemical Society reviews 43: 6750–6764.

[135] Jang H, Zheng J, Lal R, Nussinov R (2008) New structures help the modeling of toxic amyloid β ion channels. Trends in Biochemical Sciences 33: 91–100.

[136] Jang H, Zheng J, Nussinov R (2007) Models of beta-amyloid ion channels in the membrane suggest that channel formation in the bilayer is a dynamic process. Biophysical journal 93: 1938–1949.

[137] Jang H, Arce FT, Ramachandran S, Kagan BL, Lal R, Nussinov R (2013) Familial Alzheimer's Disease Osaka Mutant (Delta E22) beta-Barrels Suggest an Explanation for the Different A beta(1-40/42) Preferred Conformational States Observed by Experiment. Journal of Physical Chemistry B 117: 11518–11529.

[138] Zhao J, Luo Y, Jang H, Yu X, Wei G, Nussinov R, Zheng J (2012) Probing ion channel activity of human islet amyloid polypeptide (amylin). Biochimica et Biophysica Acta (BBA) - Biomembranes 1818: 3121–3130.

[139] Jang H, Ma B, Lal R, Nussinov R (2008) Models of toxic β-sheet channels of protegrin-1 suggest a common subunit organization motif shared with toxic alzheimer β-amyloid ion channels. Biophysical journal 95: 4631–4642.

[140] Gupta K, Jang H, Harlen K, Puri A, Nussinov R, Schneider JP, Blumenthal R (2013) Mechanism of membrane permeation induced by synthetic β-hairpin peptides. Biophysical Journal 105: 2093–2103.

[141] Woolf TB, Roux B (1994) Molecular dynamics simulation of the gramicidin channel in a phospholipid bilayer. Proceedings of the National Academy of Sciences of the United States of America 91: 11631–11635.

[142] Klauda JB, Venable RM, Freites JA, O'Connor JW, Tobias DJ, Mondragon-Ramirez C, Vorobyov I, MacKerell AD, Pastor RW (2010) Update of the CHARMM All-Atom Additive Force Field for Lipids: Validation on Six Lipid Types. Journal of Physical Chemistry B 114: 7830–7843.

[143] Durell SR, Brooks BR, Ben-Naim A (1994) Solvent-Induced Forces between Two Hydrophilic Groups. The Journal of Physical Chemistry 98: 2198–2202.

[144] Phillips JC, Braun R, Wang W, Gumbart J, Tajkhorshid E, Villa E, Chipot C, Skeel R D Kalé L, Schulten K (2005) Scalable molecular dynamics with NAMD. J Comput Chem 26: 1781–1802.

[145] Allen TW, Andersen OS, Roux B (2004) Energetics of ion conduction through the gramicidin channel. Proceedings of the National Academy of Sciences of the United States of America 101: 117–122.

[146] Nussbaum JM, Schilling S, Cynis H, Silva A, Swanson E, Wangsanut T, Tayler K, Wiltgen B, Hatami A, Rönicke R, Reymann K, Hutter-Paier B, Alexandru A, Jagla W, Graubner S, Glabe CG, Demuth HU, Bloom GS (2012) Prion-like behaviour and tau-dependent cytotoxicity of pyroglutamylated amyloid-β. Nature 485: 651–655.

[147] Bleicken S, Wagner C, García-Sáez AJ (2013) Mechanistic differences in the membrane activity of bax and Bcl-xL correlate with their opposing roles in apoptosis. Biophysical Journal 104: 421–431.

[148] Smart OS, Goodfellow JM, Wallace Ba (1993) The pore dimensions of gramicidin A. Biophysical journal 65: 2455–2460.

[149] Hubner CA (2002) Ion channel diseases. Human Molecular Genetics 11: 2435–2445.

[150] Dworakowska B, Dolowy K (2000) Ion channels-related diseases. Acta biochimica Polonica 47: 685–703.

[151] Ackerman MJ, Clapham DE (1997) Ion Channels — Basic Science and Clinical Disease. New England Journal of Medicine 336: 1575–1586.

[152] Wirths O, Bethge T, Marcello A, Harmeier A, Jawhar S, Lucassen PJ, Multhaup G, Brody DL, Esparza T, Ingelsson M, Kalimo H, Lannfelt L, Bayer Ta (2010) Pyroglutamate Aβ pathology in APP/PS1KI mice, sporadic and familial Alzheimer's disease cases. Journal of Neural Transmission 117: 85–96.

[153] Dubyak GR (2004) Ion homeostasis, channels, and transporters: an update on cellular mechanisms. Advances in physiology education 28: 143–54.

[154] Baaken G, Sondermann M, Schlemmer C, Rühe J, Behrends JC (2008) Planar microelectrode-cavity array for high-resolution and parallel electrical recording of membrane ionic currents. Lab on a chip 8: 938–44.

[155] Baaken G, Ankri N, Schuler AK, Rühe J, Behrends JC (2011) Nanopore-based single-molecule mass spectrometry on a lipid membrane microarray. ACS nano 5: 8080–8.

[156] Baaken G, Halimeh I, Bacri L, Pelta J, Oukhaled A, Behrends JC (2015) High-Resolution Size-Discrimination of Single Nonionic Synthetic Polymers with a Highly Charged Biological Nanopore. ACS nano .

[157] del Rio Martinez JM, Zaitseva E, Petersen S, Baaken G, Behrends JC (2015) Automated formation of lipid membrane microarrays for ionic single-molecule sensing with protein nanopores. Small (Weinheim an der Bergstrasse, Germany) 11: 119–25.

[158] DeKosky ST, Scheff SW (1990) Synapse loss in frontal cortex biopsies in Alzheimer's disease: correlation with cognitive severity. Annals of neurology 27: 457–64.

[159] Terry RD, Masliah E, Salmon DP, Butters N, DeTeresa R, Hill R, Hansen LA, Katzman R (1991) Physical basis of cognitive alterations in Alzheimer's disease: synapse loss is the major correlate of cognitive impairment. Annals of neurology 30: 572–80.

[160] Davies CA, Mann DM, Sumpter PQ, Yates PO (1987) A quantitative morphometric analysis of the neuronal and synaptic content of the frontal and temporal cortex in patients with Alzheimer's disease. Journal of the neurological sciences 78: 151–64.

[161] Shankar GM, Bloodgood BL, Townsend M, Walsh DM, Selkoe DJ, Sabatini BL (2007) Natural oligomers of the Alzheimer amyloid-beta protein induce reversible synapse loss by modulating an NMDA-type glutamate receptor-dependent signaling pathway. The Journal of neuroscience : the official journal of the Society for Neuroscience 27: 2866–75.

[162] Kirkitadze MD, Bitan G, Teplow DB (2002) Paradigm shifts in Alzheimer's disease and other neurodegenerative disorders: The emerging role of oligomeric assemblies. Journal of Neuroscience Research 69: 567–577.

[163] Stroud JC, Liu C, Teng PK, Eisenberg D (2012) Toxic fibrillar oligomers of amyloid-β have cross-β structure. Proceedings of the National Academy of Sciences 109: 7717–7722.

[164] Bernstein SL, Dupuis NF, Lazo ND, Wyttenbach T, Condron MM, Bitan G, Teplow DB, Shea JE, Ruotolo BT, Robinson CV, Bowers MT (2009) Amyloid-β protein oligomerization and the importance of tetramers and dodecamers in the aetiology of Alzheimer's disease. Nature chemistry 1: 326–331.

[165] Bernstein SL, Wyttenbach T, Baumketner A, Shea JE, Bitan G, Teplow DB, Bowers MT (2005) Amyloid β-protein: Monomer structure and early aggregation states of Aβ42 and its Pro19 alloform. Journal of the American Chemical Society 127: 2075–2084.

[166] Eisenberg D, Jucker M (2012) The amyloid state of proteins in human diseases. Cell 148: 1188–1203.

[167] Lashuel Ha, Hartley D, Petre BM, Walz T, Lansbury PT (2002) Neurodegenerative disease: amyloid pores from pathogenic mutations. Nature 418: 291.

[168] Lashuel Ha, Lansbury PT (2006) Are amyloid diseases caused by protein aggregates that mimic bacterial pore-forming toxins? Quarterly reviews of biophysics 39: 167–201.

[169] Laurén J, Gimbel DA, Nygaard HB, Gilbert JW, Strittmatter SM (2009) Cellular prion protein mediates impairment of synaptic plasticity by amyloid-beta oligomers. Nature 457: 1128–32.

[170] Diaz JC, Simakova O, Jacobson KA, Arispe N, Pollard HB (2009) Small molecule blockers of the Alzheimer Abeta calcium channel potently protect neurons from Abeta cytotoxicity. Proceedings of the National Academy of Sciences of the United States of America 106: 3348–53.

[171] Mandel SA, Amit T, Weinreb O, Reznichenko L, Youdim MBH (2008) Simultaneous manipulation of multiple brain targets by green tea catechins: a potential neuroprotective strategy for Alzheimer and Parkinson diseases. CNS neuroscience & therapeutics 14: 352–65.

[172] Wagner J, Ryazanov S, Leonov A, Levin J, Shi S, Schmidt F, Prix C, Pan-Montojo F, Bertsch U, Mitteregger-Kretzschmar G, Geissen M, Eiden M, Leidel F, Hirschberger T, Deeg Aa, Krauth JJ, Zinth W, Tavan P, Pilger J, Zweckstetter M, Frank T, Bähr M, Weishaupt JH, Uhr M, Urlaub H, Teichmann U, Samwer M,

Bötzel K, Groschup M, Kretzschmar H, Griesinger C, Giese A (2013) Anle138b: A novel oligomer modulator for disease-modifying therapy of neurodegenerative diseases such as prion and Parkinson's disease. Acta Neuropathologica 125: 795–813.

[173] Giese A, Bertsch U, Kretzschmar H, Habeck M, Hirschberger T, Tavan P, Griesinger C, Leonov A, Ryazanov S, Weber P (2009). New drug for inhibiting aggregation of proteins involved in diseases linked to protein aggregation and/or neurodegenerative diseases.

[174] Levin J, Schmidt F, Boehm C, Prix C, Bötzel K, Ryazanov S, Leonov A, Griesinger C, Giese A (2014) The oligomer modulator anle138b inhibits disease progression in a Parkinson mouse model even with treatment started after disease onset. Acta neuropathologica 127: 779–80.

[175] Liu F, Arce FT, Ramachandran S, Lal R (2006) Nanomechanics of hemichannel conformations: Connexin flexibility underlying channel opening and closing. Journal of Biological Chemistry 281: 23207–23217.

[176] Di Paolo G, Kim TW (2011) Linking lipids to Alzheimer's disease: cholesterol and beyond. Nature reviews Neuroscience 12: 284–296.

[177] Glabe CG (2008) Structural classification of toxic amyloid oligomers. Journal of Biological Chemistry 283: 29639–29643.

[178] Chiang K, Koo EH (2014) Emerging therapeutics for Alzheimer's disease. Annual review of pharmacology and toxicology 54: 381–405.

[179] Teich A, Arancio O (2012) Is the Amyloid Hypothesis of Alzheimer's disease therapeutically relevant? Biochemical Journal 446: 165–177.

[180] Citron M (2004) Strategies for disease modification in Alzheimer's disease. Nature Reviews Neuroscience 5: 677–685.

[181] Holmes C, Boche D, Wilkinson D, Yadegarfar G, Hopkins V, Bayer A, Jones RW, Bullock R, Love S, Neal JW, Zotova E, Nicoll JA (2008) Long-term effects of Aβ42 immunisation in Alzheimer's disease: follow-up of a randomised, placebo-controlled phase I trial. The Lancet 372: 216–223.

[182] Postina R, Schroeder A, Dewachter I, Bohl J, Schmitt U, Kojro E, Prinzen C, Endres K, Hiemke C, Blessing M, Flamez P, Dequenne A, Godaux E, Van Leuven F, Fahrenholz F (2004) A disintegrin-metalloproteinase prevents amyloid plaque formation and hippocampal defects in an Alheizmer disease mouse model. Journal of Clinical Investigation 113: 1456–1464.

[183] Bateman RJ, Siemers ER, Mawuenyega KG, Wen G, Browning KR, Sigurdson WC, Yarasheski KE, Friedrich SW, DeMattos RB, May PC, Paul SM, Holtzman DM (2009) A gamma-secretase inhibitor decreases amyloid-beta production in the central nervous system. Annals of Neurology 66: 48–54.

[184] Yi P, Hadden C, Kulanthaivel P, Calvert N, Annes W, Brown T, Barbuch RJ, Chaudhary A, Ayan-Oshodi Ma, Ring BJ (2010) Disposition and metabolism of semagacestat, a gamma-secretase inhibitor, in humans. Drug Metabolism and Disposition 38: 554–565.

[185] Masliah E, Rockenstein E, Veinbergs I, Mallory M, Hashimoto M, Takeda A, Sagara Y, Sisk A, Mucke L (2000) Dopaminergic loss and inclusion body formation in alpha-synuclein mice: implications for neurodegenerative disorders. Science (New York, NY) 287: 1265–9.

[186] Greenfield NJ (2006) Using circular dichroism spectra to estimate protein secondary structure. Nature protocols 1: 2876–90.

[187] Martin SR, Schilstra MJ (2008) Circular dichroism and its application to the study of biomolecules. Methods in cell biology 84: 263–93.

[188] Biancalana M, Koide S (2010) Molecular mechanism of Thioflavin-T binding to amyloid fibrils. Biochimica et Biophysica Acta - Proteins and Proteomics 1804: 1405–1412.

[189] Kerns EH (2001) High throughput physicochemical profiling for drug discovery. Journal of pharmaceutical sciences 90: 1838–58.